

The electronic structure of transition metal dichalcogenides investigated by angle-resolved photoemission spectroscopy

Mathias Gehlmann

Schlüsseltechnologien / Key Technologies

Band / Volume 170

ISBN 978-3-95806-324-2

Forschungszentrum Jülich GmbH
Peter Grünberg Institut (PGI)
Elektronische Eigenschaften (PGI-6)

The electronic structure of transition metal dichalcogenides investigated by angle-resolved photoemission spectroscopy

Mathias Gohlmann

Schriften des Forschungszentrums Jülich
Reihe Schlüsseltechnologien / Key Technologies

Band / Volume 170

ISSN 1866-1807

ISBN 978-3-95806-324-2

Bibliografische Information der Deutschen Nationalbibliothek.
Die Deutsche Nationalbibliothek verzeichnet diese Publikation in der
Deutschen Nationalbibliografie; detaillierte Bibliografische Daten
sind im Internet über <http://dnb.d-nb.de> abrufbar.

Herausgeber und Vertrieb: Forschungszentrum Jülich GmbH
Zentralbibliothek, Verlag
52425 Jülich
Tel.: +49 2461 61-5368
Fax: +49 2461 61-6103
zb-publikation@fz-juelich.de
www.fz-juelich.de/zb

Umschlaggestaltung: Grafische Medien, Forschungszentrum Jülich GmbH

Druck: Grafische Medien, Forschungszentrum Jülich GmbH

Copyright: Forschungszentrum Jülich 2018

Schriften des Forschungszentrums Jülich
Reihe Schlüsseltechnologien / Key Technologies, Band / Volume 170

D 464 (Diss., Duisburg, Univ., 2018)

ISSN 1866-1807
ISBN 978-3-95806-324-2

Vollständig frei verfügbar über das Publikationsportal des Forschungszentrums Jülich (JuSER)
unter www.fz-juelich.de/zb/openaccess.



This is an Open Access publication distributed under the terms of the [Creative Commons Attribution License 4.0](https://creativecommons.org/licenses/by/4.0/), which permits unrestricted use, distribution, and reproduction in any medium, provided the original work is properly cited.

Contents

Zusammenfassung	1
Abstract	3
1 Introduction	5
2 Theoretical background	9
2.1 Electronic band structure	9
2.2 Spin-orbit coupling in solids	13
2.3 Density functional theory	16
2.3.1 The Kohn-Sham equations	16
2.3.2 Numeric band structure calculations	17
2.4 Photoemission spectroscopy	20
2.4.1 The photoemission process	20
2.4.2 Angle-resolved photoemission spectroscopy	23
2.5 Van der Waals materials	31
2.5.1 The van der Waals interaction	31
2.5.2 Layered crystals	32
2.5.3 Atomically thin materials	33
2.5.4 Transition metal dichalcogenides	33
3 Experimental setup	35
3.1 ARPES setup at PGI-6	37
3.2 Beamline 5 at DELTA	46
3.3 Momentum microscope at Elettra	53
4 The hidden spin-polarization of 2H-MoS₂	59
4.1 Sample Properties	60
4.1.1 2H-MoS ₂ crystal structure	60
4.1.2 Cleavage behavior	61

4.1.3	Identification of the correct MoS ₂ polytype	63
4.2	2D electronic states in a 3D crystal	65
4.2.1	Comparison to a freestanding monolayer	65
4.2.2	The valence band splitting at the \bar{K} point	69
4.2.3	Surface electronic structure	71
4.2.4	Exclusion of the 3R phase	73
4.3	The hidden spin-polarization	75
4.3.1	Quantum mechanical considerations	75
4.3.2	Spin-ARPES experiments	78
4.3.3	The initial band polarization	81
4.3.4	Spin-layer locking	84
4.4	Conclusions	86
5	The electronic structure of ReS₂	87
5.1	3D band mapping ReS ₂ bulk single crystals	87
5.1.1	ARPES experiments and DFT calculations	88
5.1.2	Applying the FEFS model	94
5.1.3	Identification of the valence band maximum	97
5.2	Atomically thin ReS ₂	100
5.2.1	Sample properties	100
5.2.2	Micro-ARPES experiments	101
5.3	Conclusions	106
6	Summary and outlook	107
	List of Abbreviations	I
	Bibliography	III

Zusammenfassung

Van-der-Waals-Materialien (vdW) bieten die Perspektive, mit einer neuartigen Generation von zweidimensionalen Bauteilen die heutige Technologie in nahezu jeder Hinsicht zu revolutionieren. Die Übergangsmetall-Dichalkogenide (TMDCs) sind eine Gruppe von vdW-Kristallen, zu der einige Halbleiter mit Bandlücken im Bereich des optischen Spektrums gehören. Daher sind sie äußerst vielversprechend für Anwendungen wie Transistoren, optische Sensoren, Solarzellen und LEDs. Der Fokus dieser Arbeit liegt auf zwei Mitgliedern der TMDC-Familie: Molybdändisulfid (MoS_2) und Rheniumdisulfid (ReS_2). Mit einer Kombination aus winkelaufgelöster Photoemissionsspektroskopie (ARPES) und Dichtefunktionaltheorie (DFT) liefern wir eine detaillierte Analyse der elektronischen Bandstruktur dieser faszinierenden Materialien.

In atomaren MoS_2 -Monolagen resultiert aus der Kombination von gebrochener Inversionssymmetrie mit dem schweren Element Molybdän eine erhebliche Spinaufspaltung von parabolischen Zuständen, sogenannten *Valleys*, an mehreren Positionen innerhalb der Bandstruktur. Daher vereint MoS_2 die grundlegenden Voraussetzungen für die Bereiche der *Spintronik* und *Valleytronik*. Es galt als allgemein bekannt, dass diese faszinierenden Eigenschaften in MoS_2 -Volumenkristallen nicht existieren können, da sie eine zentrosymmetrische Raumgruppe besitzen. Wir zeigen jedoch, dass die Valleys nahezu vollständig innerhalb der vdW-Lagen lokalisiert sind, was zu einer vor Kurzem entdeckten Art *versteckter Spinpolarisation* führt, und dass diese die Ausbildung von quasi-zweidimensionalen und stark polarisierten Zuständen in diesem zentrosymmetrischen Kristall ermöglicht.

Des Weiteren werden die bisher ersten ARPES-Messungen an Volumenkristallen sowie an Mono- und Zweifachlagen von ReS_2 präsentiert. Aus jüngsten Veröffentlichungen gingen Hinweise hervor, die auf einen vollständigen Einschluss der elektronischen Volumenzustände innerhalb der vdW-Lagen hindeuten. Dies können wir aber mit dem Nachweis einer deutlichen dreidimensionalen Delokalisierung der Valenzelektronen widerlegen. Außerdem wird das Valenzbandmaximum experimentell für Mono- und Zweifachlagen sowie für das Volumen identifiziert. Mit der Kombination von ARPES und Bandstrukturechnungen wird gezeigt, dass ReS_2 -Zweifachlagen und das Volumen einen direkten Bandübergang besitzen, dass der Übergang in Monolagen allerdings indirekt ist.

Abstract

Van der Waals (vdW) materials offer a perspective to revolutionize basically every facet of nowadays technology with a new generation of atomically thin devices. Transition metal dichalcogenides (TMDCs) are a family of vdW crystals, that includes several semiconducting materials with band gaps within the optical range. This makes them ideal for numerous applications such as transistors, optical sensors, solar cells, and LEDs. In this study we focus on two members of the TMDC family: molybdenum disulfide (MoS_2) and rhenium disulfide (ReS_2). Using a combination of angle-resolved photoemission spectroscopy (ARPES) with density functional theory (DFT), we provide a thorough analysis of the electronic band structure of these two exceptional materials.

In monolayers of MoS_2 the combination of broken inversion symmetry with the heavy element molybdenum leads to a large spin-splitting of distinct valleys within its electronic structure. Therefore, MoS_2 combines the essential ingredients for so-called *spintronics* and *valleytronics*. It was generally believed that these fascinating features are forbidden in MoS_2 bulk crystals due to their centrosymmetric space group. This study demonstrates that the strong confinement of the valleys within the vdW layers leads to a recently discovered type of *hidden spin-polarization*, which results in quasi two-dimensional, highly spin-polarized states in this centrosymmetric bulk crystal.

Furthermore, we present the first ARPES study of ReS_2 bulk, monolayer, and bilayer crystals. Recent literature reported indications for a total confinement of the bulk electronic structure within the plains of the vdW layers. Our study comes to the opposite conclusion. Based on the observation of a considerable out-of-plane dispersion in the ARPES experiments, as well as in the band structure calculations, we show that valence electrons are significantly delocalized across the vdW gap. In addition, we identify the valence band maximum of bulk, monolayer, and bilayer ReS_2 experimentally. The combination of ARPES and band structure calculations shows that ReS_2 undergoes a transition from a direct band gap in the bulk and bilayer to an indirect gap in the monolayer.

Introduction

From our every day experience it has become entirely natural to us that the technology around us gets faster, smaller, and more affordable. Most of us carry mobile phones in our pockets that have no trouble outperforming what was an up-to-date desktop PC ten years ago. And probably none of us doubt, that ten years from now people will smile about nowadays “smartphones” performance. This technological trend can even be quantified: already in 1965 Gordon E. Moore predicted that the number of transistors in an integrated circuit will double every two years [1]. Back then he only dared to forecast the development until 1975. Not only was he right about this ten year period, but until today engineers and scientists managed to keep up with “Moore’s law”, doubling the performance of computer every two years.

The exponential growth in computing power has continued successfully for decades following the same principle: making silicon-based transistors smaller. This year the semiconductor industry formally announced in the *International Technology Roadmap for Semiconductors* that they will abandon Moore’s law as its central dogma [2]. It seems that, 45 years after the first commercially available microprocessor [3], silicon finally ran out of *room at the bottom*, and reached the lower limit in size, defined by the quantum tunneling effect [4]. The demand for an increase of computing power, however, remains and new challenges are gaining awareness. In 2012 information technology consumed $\approx 5\%$ of the global electric power, and is predicted to rise drastically within the next years [5]. On the one hand a growing portion of the world’s population gains access to electronic devices, on the other hand computers and networking technology are integrated into an increasing number of everyday items, such as refrigerators, watches, or clothes. The so-called *internet of things* demands power efficiency not only for ecological and economical reasons, but devices should also run for long time disconnected from the power grid. Since the development of silicon-based electronics seems to be heading towards a dead end, entirely new concepts for computing are required.

Promising candidates to become the basis for the next generation of electronics are van der Waals (vdW) materials. They are named after a peculiar structural prop-

erty: they are layered in sections of covalently bound atoms, while the coupling of the layers to each other is the much weaker vdW interaction. In 2010 Andre Geim and Konstantin Novoselov were rewarded the Nobel prize in physics “for groundbreaking experiments regarding the two-dimensional material graphene” [6]. Geim and Novoselov showed that by simply peeling layers from the surface of the vdW material graphite with scotch tape, it was possible to create carbon sheets with a thickness of only one single atom, the so-called graphene. Furthermore, they demonstrated that this newly discovered, purely two-dimensional material possesses a range of physical properties that had never been observed in another material before [7]. The fascinating discoveries regarding graphene triggered an outburst in research activity, which quickly spread to other layered materials that could be thinned down to two-dimensional sheets in a similar fashion. In addition to graphene, which is a semimetal, scientists characterized two-dimensional semiconductors such as MoS₂, WSe₂, and ReS₂, metals such as TiS₂ and SbS₂, and the wide band gap insulator BN, to name but a few [8–10]. Therefore, two-dimensional equivalents to all basic building blocks of classical electronics are available. Due to the ease at which the different materials can be restacked in lateral and vertical heterojunctions, vdW materials even caught the nickname “atomic-scale Legos” [11].

Prototype devices have already demonstrated that vdW materials could push the size, speed, and power consumption of transistors beyond the limits of silicon-based electronics [12–16]. But the scope of possible applications goes much further. All classical devices are based on the same principle: switching between high and low resistive states. vdW materials offer fundamentally different approaches such as *spintronics*, which relies on the electron’s spin instead of its charge [17–22], *valleytronics*, which adds the electron momentum as an additional degree of freedom [23–26], or a combination of the two [27–31]. Apart from major advances in computing power and efficiency, concepts have been proposed to use vdW materials to create a new generation of solar cells [32–35], light-emitting diodes (LEDs) and displays [36, 37], or sensors [22, 38]. And since the layers are ultra-thin and robust, it is imaginable that the devices can be engineered to be transparent and mechanically flexible.

Layered materials have the chance to revolutionize basically every facet of nowadays technology. Their extraordinary potential is based on mechanisms that are rooted deeply within the quantum mechanical properties of the material’s electrons. The interplay of the electrons with the covalently bound crystal lattice, the vdW interlayer coupling, and the two-dimensional confinement make the system quite

complicated to describe. But these are exactly the degrees of freedom that make vdW materials so promising. In solid state physics the quantum mechanical state of electrons in a crystal is defined by their band structure, which is the relation between binding energy and momentum, and it can also be extended to the electron spin. The electronic band structure defines fundamental properties such as charge transport, optical excitation and decay, and spin-polarization. Therefore, its investigation is at the heart of finding and optimizing novel concepts for electronic applications.

This thesis will present a study of the electronic band structure of the transition metal dichalcogenides (TMDCs) molybdenum disulfide (MoS_2) and rhenium disulfide (ReS_2). Shortly after the discovery of graphene, TMDCs, especially MoS_2 , drew the attention of many researchers, since they provided a semiconducting graphene-equivalent. However, it quickly became clear that TMDCs offer far more than a replacement of silicon as a transistor gate material. Monolayer MoS_2 combines broken inversion symmetry with the heavy element molybdenum, which allows for huge spin-splittings in the electronic structure. Furthermore, it possesses distinct valleys in its band structure, that are well separated in momentum space. This means MoS_2 combines the two essential ingredients for spintronic and valleytronic applications [30]. ReS_2 on the other hand has an uniaxially distorted crystal lattice, which leads to an extremely anisotropic charge transport and optical behavior. Therefore, ReS_2 shows a high potential for various sensoric applications [39].

The key technique of this thesis is angle-resolved photoemission spectroscopy (ARPES). It is capable of probing both the electron energy and momentum, and therefore provides a direct, experimental access to the electronic band structure. The experiments are combined with a theoretical description of the system based on density functional theory (DFT) band structure calculations.

The thesis is organized in the following way:

- Chapter 2 gives an overview of the basic theoretical concepts of the electronic band structure, density functional theory, photoemission spectroscopy, and van der Waals materials.
- Chapter 3 introduces the experimental setups with a focus on ARPES.
- Chapter 4 presents the study of MoS₂ bulk crystals. It focuses on the splitting of distinct valleys in the electronic band structure. The results of the ARPES experiments and the DFT calculations demonstrate that the valleys are strongly confined within the two-dimensional monolayers of the vdW crystal. By additionally performing spin-ARPES measurements we show that bulk MoS₂ hosts a recently introduced type of *hidden spin-polarization*, which is a result of quasi two-dimensional states within the three-dimensional crystal.
- Chapter 5 shows an ARPES and DFT study of ReS₂ bulk, monolayer, and bilayer crystals. The first investigated issue is the three-dimensional delocalization of the valence electrons. ARPES measurements are performed with a momentum microscope, and the three-dimensional band dispersion is analyzed using the free-electron final-state (FEFS) model. We prove that the valence electrons of ReS₂ are significantly delocalized between the vdW layers, which stands in contrast to reports in the recent literature. The second issue that is investigated is the position of the valence band maximum. Atomically thin monolayer and bilayer samples are produced by mechanical exfoliation. Their band structure is mapped with momentum microscopy, and compared to the ReS₂ bulk crystals. The combination of photoemission and band structure calculations allows the identification of a transition from a direct band gap in the bulk and bilayer to an indirect gap in the monolayer.
- Chapter 6 gives a summary of the presented results and conclusions, and presents an outlook for this thesis.

Theoretical background

This chapter will give an overview of the basic theoretical concepts underlying this thesis. In particular the electronic band theory and its central role in solid state physics is introduced, together with employed experimental and computational methods.

Electronic band structure

One of the greatest breakthroughs in solid state physics was the formulation of **Bloch's theorem**, which allowed a quantum mechanical treatment of delocalized electrons in a crystal [40]. The resulting band theory provided major advances in the understanding of some of the most basic properties of solids, such as electric conductivity, optical absorption and transparency, or ferromagnetism. Ultimately the electronic band theory has become an essential foundation for the field of modern solid-state physics.

Bloch's theorem states that energy eigenstates of electrons in a periodic crystal have the form of **Bloch waves** [41]:

$$\psi(\mathbf{r}) = e^{i\mathbf{k}\cdot\mathbf{r}} \cdot u(\mathbf{r}) \quad (2.1)$$

The crucial postulation is that the amplitude of the Bloch wave $u(\mathbf{r})$ shares the crystal symmetry and remains unaffected in case of a displacement by the crystal lattice vector \mathbf{T} :

$$u(\mathbf{r}) = u(\mathbf{r} + \mathbf{T}). \quad (2.2)$$

Based on this approach it is possible to solve the stationary Schrödinger equation for a given value of the electron wave vector \mathbf{k} to obtain a set of energy eigenvalues $E_n(\mathbf{k})$. This solution gives a range of allowed energies as a function of \mathbf{k} , or the n -th *energy band*.

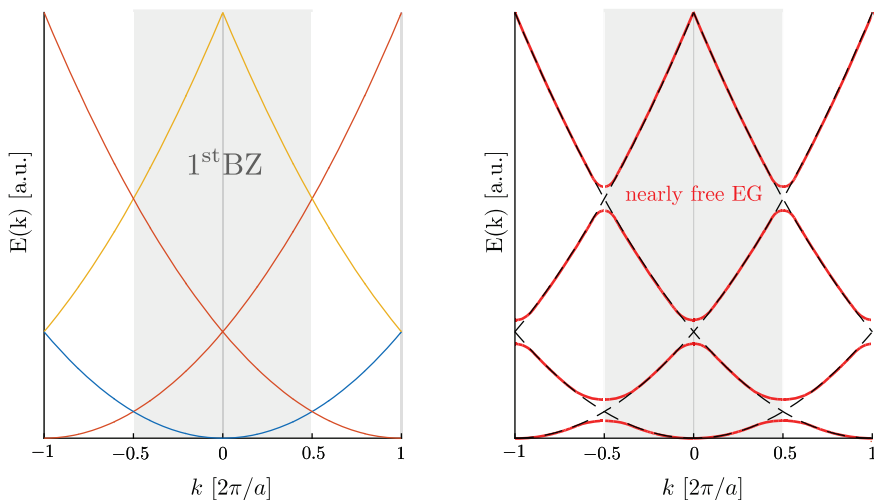


Figure 2.1: Energy eigenvalues $E_n(\mathbf{k})$ of the free electrons (left panel) and nearly free electron gas (right panel) in a 1D crystal with the lattice constant a . At the BZ edges and in the center the crystal field opens band gaps.

Since the invariance with respect to the crystal lattice \mathbf{T} carries over to the wavefunction, the same holds in reciprocal space with the reciprocal lattice vector \mathbf{G} :

$$E_n(\mathbf{k}) = E_n(\mathbf{k} + \mathbf{G}) \quad . \quad (2.3)$$

Therefore, it is sufficient to discuss the solutions within the 1st Brillouin zone (BZ), the Wigner-Seitz cell of reciprocal space. For every \mathbf{k} vector there is an equivalent solution within the 1st BZ.

The left panel of Figure 2.1 shows the band structure of free electrons in a 1-dimensional crystal. This model for the electronic bands appears to be an acceptable description for many materials, as long as \mathbf{k} is not close to high symmetry points, which means at the edge or the center of the BZ [41]. Close to high symmetry points one can find pronounced deviations from the parabolic bands, which is illustrated in the right panel of figure 2.1. Qualitatively this behavior can be understood within the *nearly free electron model*. The meaning of a \mathbf{k} vector close the BZ edge is that the corresponding wavelength matches the crystal periodicity. In this case the Bloch

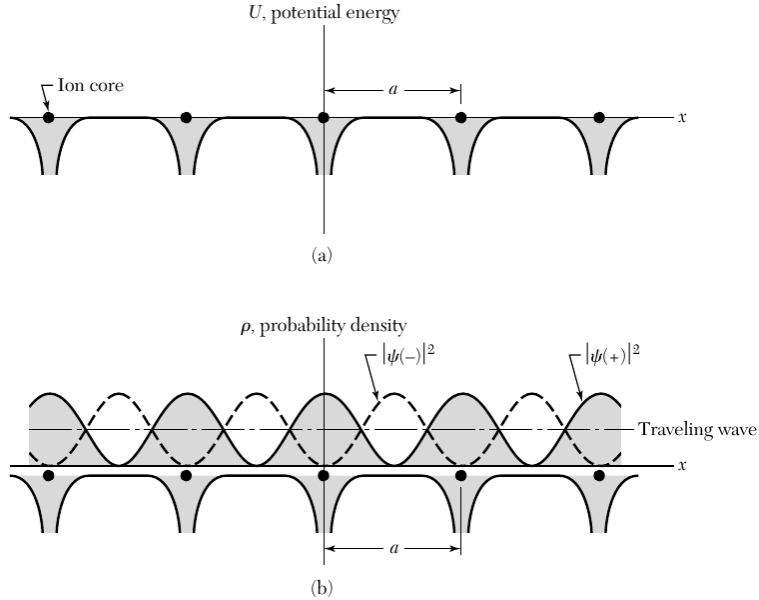


Figure 2.2: Coulomb potential of the atomic cores b) Bloch wave separated into two components that are in phase ($\psi(+)$) and out of phase ($\psi(-)$) with the atomic cores (adapted from [41])

wave can be separated into two components $\psi(+)$ and $\psi(-)$ that oscillate in phase (+) and out of phase (-) with the atomic positions. Since the charge density of $\psi(+)$ is more concentrated close to the atoms, the band gains significant electrostatic energy compared to $\psi(-)$. Therefore, the degeneracy of $\psi(+)$ and $\psi(-)$ is lifted, and so-called *band gaps* are opened at the zone edges.

The presence of band gaps, which define regions of forbidden energies, allows the classification of materials as metals, insulators, or semiconductors. From the band structure one can derive the density of states $D(E)$, which is the number of available electronic states within the energy window ∂E . Within the band gaps the density of states drops to zero. Since electrons are fermions, they are distributed according to the Fermi-Dirac distribution $f_{FD}(E)$, which gives the probability of a state being occupied as a function of the energy:

$$f_{FD}(E) = \left(e^{\frac{E-E_f}{k_B T}} + 1 \right)^{-1} . \quad (2.4)$$

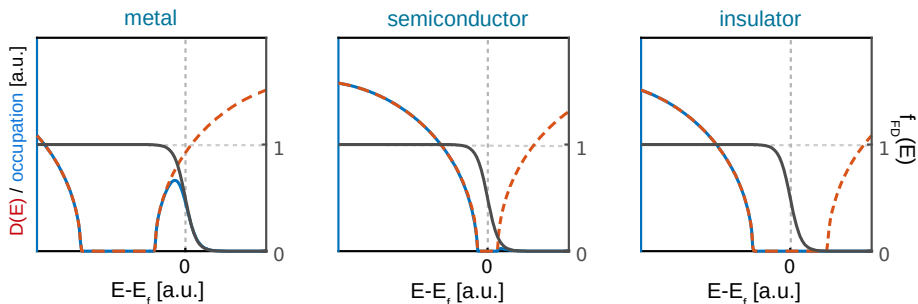


Figure 2.3: Illustration of the distinction between metal, semiconductor, and insulator. For 3 cases a simplified density of states (red, dashed) is multiplied with the Fermi-Dirac distribution (black), and results in the occupied states (blue).

Figure 2.3 illustrates the distribution of electrons according to $f_{FD}(E)$ over a simplified density of states with a band gap. In a metal the Fermi energy E_f , which separates occupied and unoccupied states, crosses at least one band, leaving it only partially filled. The immediate proximity of partially occupied states in the band structure allows the redistribution of electrons even by small electric fields, which results in a flowing charge current. In the case of an insulator the Fermi level lies within a band gap, separating bands into completely filled ones, which are called **valence bands**, and the completely unoccupied **conduction bands**¹. Therefore, the band gap provides a threshold for any redistribution of the electrons, which is otherwise forbidden by the Pauli exclusion principle. If the thermal excitation results in a considerable number of electrons overcoming the band gap the material is classified as a semiconductor. The size of the band gap alone does not determine the distribution of electrons between valence and conduction band, but also the position of the Fermi-energy within the gap, which can be modified by *doping*. Even materials with a relatively large band gap can be considered as semiconductors, if E_f is sufficiently close to the valence band (p-type) or the conduction band (n-type).

¹In some definitions only the topmost occupied and the first unoccupied bands are considered the valence/conduction band.

Spin-orbit coupling in solids

The term spin-orbit coupling (SOC) describes the interaction between the spin \mathbf{S} of a particle and its orbital momentum \mathbf{L} [42]. From a technological point of view the SOC is of key importance in the field of *spintronics*. Since it breaks the time reversal symmetry, it can lift the spin-degeneracy of electronic states without the presence of a magnetic field or magnetization [17].

When discussing SOC in a solid one should distinguish between two types of electronic states: core levels and dispersing energy bands. An electronic state at binding energies higher than 20 - 50 eV can be considered a core level. Because of their high binding energy the atomic sites for core levels are separated by high potential barriers, which prohibit the delocalization of the states, and they show no dispersion (meaning no \mathbf{k} -dependence). In addition the proximity to the core makes the contribution of the neighboring atoms to the potential almost negligible. Therefore, core states can be treated very similarly to atomic orbitals. The SOC of an isolated atom can be approximated ² from the Dirac equation:

$$\hat{H}_{SOC} = \xi(\hat{\mathbf{L}} \cdot \hat{\mathbf{S}}) \quad ; \quad \xi = \frac{e^2}{2\pi\epsilon_0 m^2 c^2} \cdot \frac{Z}{r^3} . \quad (2.5)$$

This equation reveals a linear scaling of the SOC strength with the atomic number Z . In addition the SOC rapidly drops with an increasing distance r from the core. This already provides a phenomenological explanation for the strong SOC in core levels (in the order of several eV), and the much weaker effect on loosely bound, dispersing electronic bands (maximum of few 100 meV, often negligible).

This simple approach of the SOC, however, cannot be easily transferred to the electronic band model. First of all, the formula 2.5 assumes a spherically symmetric potential $V(r)$. For delocalized electronic bands, however, the symmetry is defined by the crystal structure instead. Furthermore, as it was introduced in chapter 2.1, the wave functions in the band model consist of Bloch waves with their respective eigenvalues $E(\mathbf{k})$. Since every \mathbf{k} point in the BZ corresponds to a Bloch wave propagating along a straight line it can neither be associated with a circular motion

² The approximation holds for $v \ll c$. Then the Hamiltonian is $\hat{H} = \hat{H}_{kin} + \hat{H}_{pot} + \hat{H}_{SOC}$ with $\hat{H}_{kin} = \frac{\hat{p}^2}{2m} - \frac{\hat{p}^4}{8m^3 c^2}$, and $\hat{H}_{pot} = V(r) - \frac{i\hbar}{4m^2 c^2} (\nabla V(r) \cdot \hat{\mathbf{p}})$. Note that despite $v \ll c$, \hat{H}_{kin} and \hat{H}_{pot} need to contain relativistic corrections. The fully non-relativistic approach gives a \hat{H}_{SOC} that is too small by a factor of 2 (missing g-factor). For further reading see ref. [43].

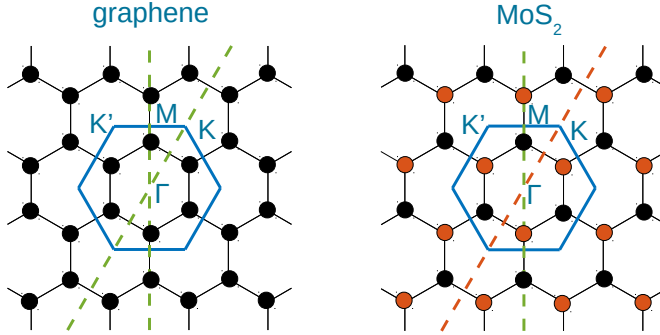


Figure 2.4: Comparison of graphene-like lattice (a) and monolayer-MoS₂-like lattice (b). In a) both lines ΓM and ΓK are mirror planes (green). As a result of the inversion symmetry all 6 K-points are equivalent. Since b) has a two atom basis the mirror symmetry along ΓK is broken and the SOC separates the BZ (blue) corners into non equivalent K/K' points allowing for spin-polarized bands.

nor is the orbital momentum quantum number l a good quantum number in the absence of spherical symmetry.

The role of the crystal symmetry in the context of SOC and the spin-polarization that may result from it, are central topics in this thesis. To allow the SOC to induce spin-polarized electronic states in the first place it is mandatory to break the inversion symmetry, since otherwise its combination with time reversal symmetry leads to *Kramers degeneracy*:

$$\left. \begin{array}{l} \text{inversion: } |\psi_{\uparrow}(\vec{k})\rangle = |\psi_{\uparrow}(-\vec{k})\rangle \\ \text{time reversal: } |\psi_{\uparrow}(\vec{k})\rangle = |\psi_{\downarrow}(-\vec{k})\rangle \end{array} \right\} \Rightarrow |\psi_{\uparrow}(\vec{k})\rangle = |\psi_{\downarrow}(\vec{k})\rangle \quad (2.6)$$

The symmetry of a Bloch state is on the one hand defined by the crystal structure, and on the other by the position of the \mathbf{k} vector within the BZ. Figure 2.4 illustrates these symmetry considerations on the example of the two-dimensional honeycomb-like crystal structure of graphene (Fig. 2.4 a) and monolayer-MoS₂ (Fig. 2.4 b). Although both crystals share the same prismatic lattice, only the graphene crystal is centrosymmetric with $\psi(\mathbf{k}) = \psi(-\mathbf{k})$. This symmetry is broken for monolayer-MoS₂ by the inequivalent atoms in its basis. In the evaluation the orbital momentum L of a Bloch state $|\psi(\mathbf{k})\rangle$

$$L = \langle \psi(\mathbf{k}) | \hat{\mathbf{r}} \times \hat{\mathbf{p}} | \psi(\mathbf{k}) \rangle \quad (2.7)$$

is not determined by a single atom, but the entity of all lattice atoms has to be taken into account. From the cross product in equation 2.7 one can see that for $L \neq 0$ an asymmetric distribution of the electron wave function around the \mathbf{k} vector is required. Without detailed knowledge of $|\psi(\mathbf{k})\rangle$ one can conclude that for every \mathbf{k} along a mirror plane the component of L within the plane must vanish.

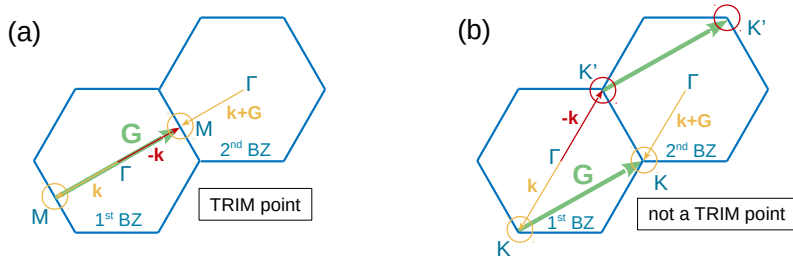


Figure 2.5: Illustration of the relation between time reversal and the lattice vector \mathbf{G} on the example of the M point (a) and the K point (b) of a hexagonal BZ, which allows the identification of TRIM points.

As it was already discussed, the SOC can break the time reversal symmetry, which means the states $|\psi(\vec{\mathbf{k}})\rangle$ and $|\psi(-\vec{\mathbf{k}})\rangle$ are not necessarily equivalent. However, in reciprocal space one can find so-called *time-reversal invariant momenta (TRIM)* points, at which the breaking of time reversal symmetry is forbidden by the periodicity of the reciprocal lattice. Figure 2.5 illustrates this concept on the example of the M point and the K point of a hexagonal BZ. For the M point time reversal is equivalent to the reciprocal lattice vector \mathbf{G} , and therefore results in an identical M point of the second BZ, which makes M a TRIM point. This is not the case for the K point, which shows that one has to distinguish between the K and K' points. Γ is a trivial TRIM point of any lattice structure, since $\mathbf{k} = 0$ cannot be reversed.

Density functional theory

The key technique of this thesis is angle-resolved photoemission spectroscopy (ARPES), which provides a rather direct, experimental access to the electronic band structure of a material. However, the insight that can be gained from the experiment can often be significantly broadened by a comparison to a thorough, theoretical description of the electronic structure. All ARPES data that are presented here is analyzed in comparison with density functional theory (DFT) calculations performed by Gustav Bihlmayer and Irene Aguilera at PGI-1. The basic concepts of DFT will be introduced within this chapter.

In the previous section the electronic band theory was discussed in the simplified context of single-particle wave functions. For a realistic description of the electronic structure, however, electron-electron correlations cannot be neglected. The central issue with this task is that the complexity of the quantum mechanical treatment of many body wave functions increases so drastically with the number of particles that systems with more than 10 particles are already virtually impossible to handle [44].

The Kohn-Sham equations

Density functional theory is based on the Hohenberg-Kohn-Sham theorem [45, 46], which states that the N particle ground state wave function $\psi(\mathbf{r}_1, \mathbf{r}_2, \dots, \mathbf{r}_N)$ and the potential $V(\mathbf{r})$ are uniquely determined by the particle density $n(\mathbf{r})$, and that the total energy can be derived as a functional of the density $E_{tot} = E[n(\mathbf{r})]$, which is stationary under first order density and energy variations [44, 47]. This leads to an eigenvalue equation in the form of:

$$\left[\underbrace{-\frac{\hbar^2}{2m}\nabla^2}_{\text{kinetic energy}} + \underbrace{V(\mathbf{r}) + e^2 \int \frac{n(\mathbf{r}')}{|\mathbf{r} - \mathbf{r}'|} d\mathbf{r}'}_{\text{coulomb interaction}} + \frac{\delta E_{xc}[n(\mathbf{r})]}{\delta n(\mathbf{r})} \right] \phi_i(\mathbf{r}) = \epsilon_i \phi_i(\mathbf{r}) \quad . \quad (2.8)$$

The term $\frac{\delta E_{xc}[n(\mathbf{r})]}{\delta n(\mathbf{r})}$ is called the exchange-correlation potential. Given that a sufficiently accurate approximation of the functional $E_{xc}[n(\mathbf{r})]$ is found, the particle density $n_0(\mathbf{r})$ of the actual many body ground state wave function $\psi(\mathbf{r}_1, \mathbf{r}_2, \dots, \mathbf{r}_N)$ can be calculated by minimizing the energy, which is determined from the eigenvalue equation 2.8, as the density is varied. This way the DFT can bypass the many

body wave function entirely, and derive central properties of the system directly from $n(\mathbf{r})$. The main challenge is to find efficient, but accurate formulations of the energy functional $E_{xc}[n(\mathbf{r})]$.

Although, the eigenvalues ϵ_i in equation 2.8 were initially introduced as Lagrange multipliers for the minimization problem, it has been established that the eigenvalues provide a good approximation for the electronic band structure, and ϕ_i for the quasiparticle wave functions. Especially for the valence bands this interpretation is confirmed by experiments [44]. One of the intrinsic limitations of DFT is that it only describes the undisturbed ground state of the system, which leads to an inaccurate description of effects such as excitation, self-interaction, and certain many body effects [48]. This results for instance in a systematic underestimation of semiconductor and insulator band gaps, and it should be kept in mind, when DFT calculations are discussed in the context of conduction band structure and photoemission, which involves photoexcitation.

Numeric band structure calculations

Electronic band structure calculations are usually performed numerically by iteratively solving the Kohn-Sham equations 2.8, and optimizing the electron density until it converges into the ground state density. The typical algorithm contains the following steps:

Step 1: determine the potential

Since the potential is a function (or functional) of the electron density, it has to be determined for a specific $n(\mathbf{r})$. At the first iteration of the algorithm an initial density has to be guessed. One typically uses a linear superposition of atomic densities. The classical Coulomb potential can be calculated by solving the Poisson equation.

Determining the exchange-correlation potential, which depends on the energy functional, is more complicated and has to rely on efficient approximations to keep the numerical effort reasonable. A rather simplistic, but successful approach is the local density approximation (LDA) [49]. It assumes that $n(\mathbf{r})$ can be approximated as homogeneous electron gas within every volume element dr . This reduces $E_{xc}[n(\mathbf{r})]$ to a function instead of a functional of $n(\mathbf{r})$ [44]:

$$E_{xc}^{LDA}(n) = \int n(\mathbf{r}) \epsilon_{xc}^{LDA}(n(\mathbf{r})) d\mathbf{r} \quad . \quad (2.9)$$

Although, the LDA is still widely used, it has been established that the accuracy of the calculation is generally improved by additionally including the local gradient of the density into the approximation of the exchange-correlation functional [50,51]. This formalism is called the generalized gradient approximation (GGA):

$$E_{xc}^{GGA}(n) = \int n(\mathbf{r}) \epsilon_{xc}^{GGA}(n(\mathbf{r}), \nabla n(\mathbf{r})) d\mathbf{r} \quad . \quad (2.10)$$

Once the exchange-correlation functional is determined, the potential can be fed into the Kohn-Sham equation.

Step 2: solve the eigenvalue problem

With the potential determined, the Kohn-Sham equation 2.8 resembles an eigenvalue problem. A numerically efficient way to solve for the eigenvalues is the expansion in a suitable basis. Since the numerical effort for a basis with N vectors scales with N^3 it is crucial to find a set of only few wave functions that efficiently represents the entire system [44]. The issue with this is that in a crystal, two quite different regimes have to be described: on the one hand the regions in the immediate proximity of the nuclei, in which single-atom orbitals provide an appropriate basis. On the other hand between the atoms the crystal potential is largely screened, and as it was already discussed, the valence electrons can be described to some degree as a free-electron gas. For these states plane waves are a more suitable basis.

The augmented plane wave (APW) method is an approach, which provides a more universal set of basis vectors. It defines a spherical region around the atoms, in which atomic orbitals are used as a basis. Outside of this sphere the orbitals are augmented with plane waves. The numerical efficiency can be further increased by using a linearized form of these wave functions in the so-called linearized augmented plane wave (LAPW) method [47].

Using this basis, the elements of the Hamiltonian of the Kohn-Sham equation 2.8 generate the Hamilton matrix \underline{H} . For the expansion the following eigenvalue problem has to be solved:

$$\underline{H}\mathbf{c}_i = \epsilon_i \mathbf{c}_i \quad . \quad (2.11)$$

The eigenvectors \mathbf{c}_i are the expansion coefficients, and in this way the solution is obtained by diagonalizing \underline{H} .

Step 3: calculate the new density

The result of the expansion can now be used to calculate a new, refined electron density. For this, the states that were obtained in the expansion are filled up to the Fermi level with the correct number of electrons. Then the density $n_{out}(\mathbf{r})$ can be calculated from the wave functions weighted with their occupation. The initial density $n_{in}(\mathbf{r})$, which was used to determine the potential of the Kohn-Sham equation in the first step, can be compared to $n_{out}(\mathbf{r})$. If the difference between the two does not exceed a certain, small amount, the density is considered *converged* and the algorithm can be stopped.

If on the other hand the density is not sufficiently converged, the algorithm has to be repeated. In order to construct the input density $n_{next}(\mathbf{r})$ for the next iteration of the algorithm, $n_{out}(\mathbf{r})$ should be mixed with $n_{in}(\mathbf{r})$ to improve the convergence behavior, which can be done for instance by a linear combination:

$$n_{next}(\mathbf{r}) = a \cdot n_{out}(\mathbf{r}) + (1 - a) \cdot n_{in}(\mathbf{r}); \quad \text{with } 0 < a < 1 \quad . \quad (2.12)$$

By repeating this procedure $n(\mathbf{r})$ can be converged against the density of the actual many body wave function within the boundaries of the basis vectors, and within the accuracy at which the exchange-correlation was approximated.

Most of the band structure calculations that are shown in this thesis were performed with the FLEUR code package [52]. FLEUR is based on the full-potential linearized augmented plane wave (FLAPW) method, which combines LAPW with a self-consistent, fully relativistic approach to determine the potential without assumptions about its shape. FLAPW in combination with the GGA exchange correlation functional is numerically rather demanding but it provides an extremely accurate description of the electronic structure, including effects such as SOC and exchange interaction.

Photoemission spectroscopy

Physical properties of a solid such as electric conductivity, optical behavior, magnetism, or its chemical properties are dominated by its electronic structure. Therefore photoemission spectroscopy (PES) has been established as one of the key techniques in solid state physics providing the most direct experimental access to electronic states.

The photoemission process

PES is based on the photoelectric effect, which was first observed in the late 19th century [53]. The observations seemed paradox at the time: only light above a certain frequency causes the emission of electrons from a material. While the light intensity determines the number of emitted electrons, it does not affect their energy. The electron energy is modified purely by the light frequency. In 1905 Albert Einstein was able to resolve the paradox by postulating the quantization of the energy transferred by light in discrete packages called photons, and was therefore awarded the Nobel prize in 1921 [54]. Einstein derived the formula for the kinetic energy of photoelectrons:

$$E_{kin} = h\nu - E_{bin} - \phi \quad . \quad (2.13)$$

In order to escape from the material the electron, that is excited by the photon energy $h\nu$, has to overcome the binding energy E_{bin} of the electronic state and the workfunction ϕ , which is a material and surface dependent constant. Therefore, a PES spectrum that is obtained with a monochromatic light source allows the analysis of the binding energy E_{bin} of occupied electronic states.

Figure 2.6 depicts a prototypical photoemission spectrum of a metal with the valence band crossing the Fermi level. As it was introduced in section 2.1, the occupation of the density of states $N(E)$ is determined by the Fermi-Dirac-distribution, and in a very simplified model the photoemission intensity can be interpreted as the signature of $N(E)$ up to the Fermi-level. In the spectrum the core levels appear as well defined lines because they are bound at discrete energy values. Since the electronic bands disperse, their intensity is distributed over a wider energy range. The kinetic energy scale of photoemission spectra can be aligned with $N(E)$ by an offset of $h\nu - \phi$ according to equation 2.13. In a standard photoemission experiment

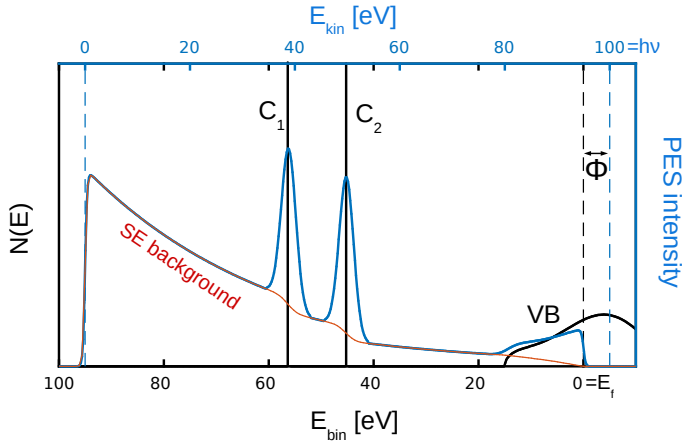


Figure 2.6: Prototypical density of states $N(E)$ (black curve) including the valence band (VB) and two core levels ($C_{1/2}$), and the corresponding PES spectrum (blue curve). $N(E)$ is plotted versus E_{bin} (bottom axis) and E_{kin} of the photoelectrons (top axis). The red, dashed line represents the typical secondary electron background within the PES spectrum.

the sample is in electrical contact with the spectrometer via a common ground potential. As a result the Fermi levels of the two align (contact voltage) and the offset of the spectrum ϕ is *not* the workfunction of the sample but of the spectrometer.

The detailed description of the photoemission process is extremely complex since it has to treat the excitation of an electron within a many body quantum system. A frequently applied approach is the **sudden approximation**, which assumes that the excitation and the escape of the photoelectron from the locally excited area are fast compared to the relaxation of the system. This reduces the process to a one-electron-problem within a stationary environment. One of the limits of the sudden approximation is a low kinetic energy due to the low electron speed, and because local potential variations due to the electron hole become more significant. Furthermore, the sudden approximation is less accurate for highly correlated electron systems such as high- T_C superconductors [55] or Mott insulators [56] since many-body effects cannot be neglected in this case, regardless of the speed of the process.

Starting from the sudden approximation the photoexcitation can be described as a single electron, which is excited by a photon with the energy $h\nu$ from the occupied *initial state* $|i\rangle$ into the unoccupied *final state* $|f\rangle$. The probability of the transition

is described by *Fermi's golden rule* [57]:

$$P_{if} = \frac{2\pi}{\hbar} |\langle f | \mathcal{H}_p | i \rangle|^2 \delta(E_f - E_i - h\nu) . \quad (2.14)$$

\mathcal{H}_p is the perturbation Hamiltonian of the photoexcitation, and the δ -distribution includes the energy conservation. If E_f lies above the vacuum energy level E_v , the photoelectron can leave the sample and reach the detector. From equation 2.14 it becomes clear that the probability of the photoemission process always depends on a **pair** of $|i\rangle$ and $|f\rangle$, with the respective *transition matrix element*:

$$M_{fi} = \langle f | \mathcal{H}_p | i \rangle . \quad (2.15)$$

M_{fi} depends mostly on the symmetries of the electronic states and the perturbation Hamiltonian \mathcal{H}_p [58]. For low photon flux densities, \mathcal{H}_p can be approximated within the *linear response theory*:

$$M_{fi} \approx -\frac{e}{mc} \langle f | \hat{\mathbf{A}} \cdot \hat{\mathbf{p}} | i \rangle \quad (2.16)$$

where $\hat{\mathbf{A}}$ is the vector potential of the electric field and $\hat{\mathbf{p}}$ the electron momentum operator. Especially for photon energies within the vacuum ultraviolet (VUV) and soft x-ray regime one can assume that the vector potential $\hat{\mathbf{A}}$ can be approximated as locally constant, which then leads to the so-called *dipole approximation*:

$$M_{fi} \approx -\frac{ie}{\hbar c} A_0 (E_f - E_i) \langle f | \hat{\mathbf{P}} \cdot \hat{\mathbf{r}} | i \rangle . \quad (2.17)$$

Here A_0 is the amplitude of the vector potential and $\hat{\mathbf{P}}$ the electric polarization. This way the transition matrix elements can be analyzed with respect to the symmetries of $|f\rangle$, $|i\rangle$, and the polarization of the light to formulate the *dipole selection rules*. They can be applied to qualitatively analyze photoemission spectra in terms of allowed transitions, e.g. in the interpretation of dichroism, which is a polarization dependent variation of the intensity [58].

Further important influences on the photoemission spectrum, aside from the probability of the photoexcitation, are the *secondary electron background* and the *energetic broadening*, which are already indicated in figure 2.6. The secondary electron background is a result of inelastic photoelectron scattering. This process creates additional, excited electrons, which can also be emitted from the sample, as long as they are excited above the vacuum level.

The energetic broadening of the PES spectrum compared to the density of states is not purely a result of the experimental resolution, which is mostly defined by the linewidth of the photons and by the energy resolution of the analyzer. Although the δ -distribution in Fermi's golden rule (eq. 2.14) suggests infinitely sharp transitions, the photoemission process itself has an intrinsic, non-zero linewidth. Within the single particle approximation the energetic broadening can be estimated from a finite duration τ of the transition. According to the uncertainty principle, this leads to the natural linewidth $\Delta E_n = \frac{\hbar}{2\tau}$. However, the single particle model fails for a non negligible coupling of the photoelectron to the electron hole, and for strong correlation effects. These mechanisms provide additional channels, over which the excitation energy has to be distributed, and strict energy conservation between initial and final state in Fermi's golden rule has to be reformulated. The δ -function in equation 2.14 is replaced by the so-called *spectral function*, which can incorporate electron-hole interaction [59] and electron correlations [58,60].

Angle-resolved photoemission spectroscopy

As discussed in section 2.1, the quantum mechanical state of an electron in a crystal consists of Bloch waves with the eigenvalue $E(\mathbf{k})$. In order to fully determine the electronic structure of a material, the binding energy of the photoelectrons has to be analyzed as a function of their momentum. The key technique in this matter is angle-resolved photoemission spectroscopy (ARPES). As the name suggests, ARPES is the measurement of the kinetic energy of photoelectrons as a function of the emission angle, from which under certain assumptions all 3 components of the momentum vector \mathbf{k} ³ can be derived.

Figure 2.7 depicts a classical ARPES setup, which uses a hemispherical analyzer in combination with a two-dimensional electron detector. The analyzer serves as an energy filter, while the dispersion along the hemisphere images an energy window onto one of the two detector dimensions (discussed in detail in section 3.1). Orthogonally to the detector dispersion, electron lenses image the angular distribution from the narrow entrance slit of the analyzer onto the second dimension of the electron detector. This setup allows one to analyze the kinetic energy of the photoelectrons

³For convenience the “wave vector” and “momentum” will be used synonymously within this thesis. The wave vector \mathbf{k} and the mechanical momentum \mathbf{p} are connected by $\mathbf{k} = \mathbf{p}/\hbar$. All values for the momentum/wave vector will be given in units of the wave number: k [\AA^{-1}].

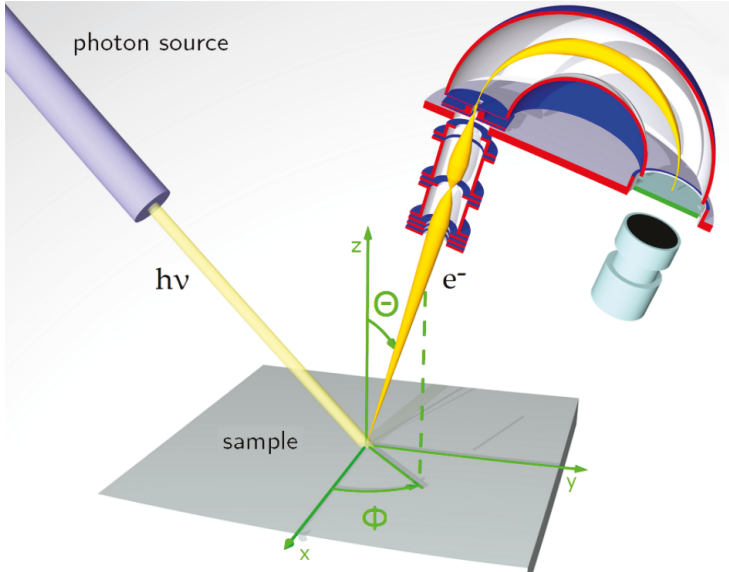


Figure 2.7: Illustration of a typical ARPES experiment (adapted from ref. [61]).

E_{kin} as a function of the angular distribution ϕ along the entrance slit direction.

The second dimension of the photoemission solid angle is defined and mapped by the position of the entrance slit. So by rotating the entrance slit orthogonally to the slit direction by the angle θ one obtains $E_{kin}(\phi, \theta)$, which fully defines the direction of the electron momentum \mathbf{k}_v of the emitted electron in vacuum. Since the norm of the momentum is defined by E_{kin} all three momentum components of the photoelectron can easily be derived:

$$\mathbf{k}_v = \frac{1}{\hbar} \sqrt{2m_e E_{kin}} \begin{pmatrix} \sin \theta \cos \phi \\ \sin \theta \sin \phi \\ \cos \theta \cos \phi \end{pmatrix}. \quad (2.18)$$

Here k_x is the momentum component parallel to the sample surface and to the entrance slit direction. k_y is the second component parallel to the surface and orthogonal to k_x , and k_z is the sample normal component. However, the directly measured momentum vector \mathbf{k}_v is *not* equivalent to the initial momentum vector \mathbf{k}_i of the initial electronic state $|i\rangle$ of the photoemission process. The next section will introduce the phenomenological **three-step model**, which divides the entire

photoemission process into separately treated steps: excitation, propagation, and escape into vacuum. By connecting the steps with basic conservation principles such as energy and momentum conservation one can derive all three components of the initial momentum \mathbf{k}_i from \mathbf{k}_v and E_{kin} . This way it is possible to interpret the ARPES data qualitatively as the a measurement of the band dispersion $E(\mathbf{k})$.

1st step: the excitation

The first step describes the excitation from the *initial state* $|i\rangle = |E_i, \mathbf{k}_i\rangle$, which is a stationary ground state of a valence electron, into the *final state* $|f\rangle = |E_f, \mathbf{k}_f\rangle$, a conduction band state in the unoccupied band structure. Energy and momentum conservation set the following relation:

$$E_f = E_i + h\nu \quad (2.19)$$

$$\mathbf{k}_f = \mathbf{k}_i + \mathbf{k}_{ph} + \mathbf{G} \quad (2.20)$$

Unless the experiment is performed with hard x-rays, $k_{ph} = \frac{h\nu}{c}$ is usually negligibly small. A photon energy of $h\nu = 120$ eV corresponds to $k_{ph} = \frac{1}{h} \cdot \frac{h\nu}{c} \approx 0.051 \text{ \AA}^{-1}$ compared to the typical BZ dimensions of $\approx 1 \text{ \AA}^{-1}$. In the context of this thesis k_{ph} can be neglected. The addition of the reciprocal lattice vector \mathbf{G} neither violates the momentum conservation, since it is transferred from the crystal lattice, nor does it change the electronic state, since the Bloch waves are periodic with \mathbf{G} . However, \mathbf{G} provides multiple possible propagation directions, and therefore multiple emission angles for the same initial state $|i\rangle$.

2nd step: the propagation

The second step is the propagation of the photoelectron in the final state $|f\rangle$ through the crystal towards the surface. Since $|f\rangle$ is an excited state it has a chance to undergo inelastic scattering on other electrons, phonons, or defects. This scattering is usually described in form of a exponential law with the inelastic mean free path (IMFP) λ :

$$I(x) = I_0 e^{-\frac{x}{\lambda}} \quad (2.21)$$

Figure 2.8 shows the experimentally determined IMFP of various materials, and

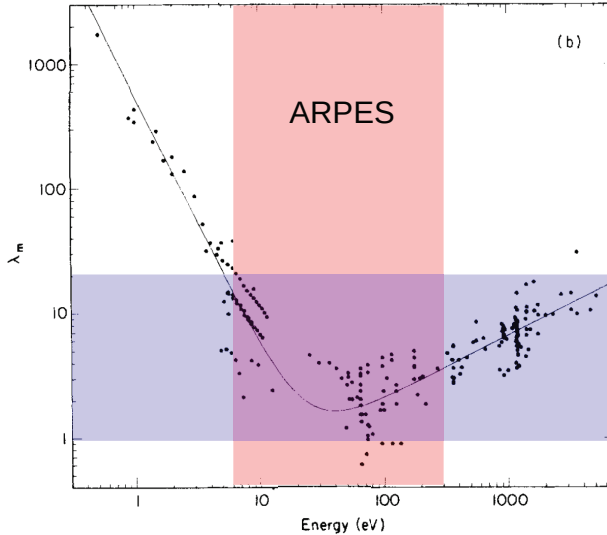


Figure 2.8: Experimental data points of the IMFP of various materials and the empirically determined universal curve as solid line. The energy scale applies for electrons inside the material, and is relative to the Fermi level. The red area shows the typical energy range for ARPES experiments, which is close to the minimum of the universal curve, and results in the low probing depth of the technique indicated in blue. (adapted from ref. [62])

the phenomenological *universal curve*. The energy scale is relative to the Fermi level, which means the very low energy range can not be observed in photoemission, since the electrons cannot overcome the workfunction and leave the sample. The universal curve shows that in the typical energy range for ARPES ($\approx 6 \text{ eV} - 200 \text{ eV}$ above E_f) the IMFP is quite low: $\approx 1 \text{ \AA} - 20 \text{ \AA}$. According to equation 2.21 about 95% of the photoemission signal stems from $3 \cdot \lambda$, which is often referred to as the probing depth or maximum escape depth of PES. This has a huge impact on PES as an experimental technique making it extremely surface sensitive. As a further consequence of the low escape depth (AR)PES usually has to be carried out under ultra-high vacuum (UHV) conditions since even the surface contaminations in the atomic monolayer regime have a drastic effect on the experiment.

However, the exact escape depth in ARPES is often unknown. The experimentally determined data points of λ scatter strongly around the universal curve. Especially at low kinetic energies the *exact* IMFP has to depend on the photoelec-

tron momentum \mathbf{k} since the final state $|f\rangle$ and the possible scattering partners such as valence electrons have dispersing band structures. Therefore the universal curve can only be seen as a rough approximation.

3rd step: escape into vacuum

The last step in this model is the transition of the photoelectron from the final state $|f\rangle$ within the crystal to the free electron plane wave state $|v\rangle$ in vacuum [63]. The main complications of describing this step are that translation symmetry is broken by the surface in the normal direction and by the potential barrier formed by the workfunction ϕ . These issues can be dealt with by assuming the conservation of the momentum component parallel to the surface \mathbf{k}_{\parallel} . This is a valid assumption since for the parallel components the crystal symmetry is not broken by the surface. In case of a structural surface relaxation might be not fulfilled (see *surface umklapp process*) [64]. Furthermore, one can assume that the surface potential barrier shares the symmetry of the surface lattice and that its gradient is mainly in the perpendicular direction. Therefore, k_x and k_y remain good quantum numbers in the surface transition. With equation 2.20 one can conclude that \mathbf{k}_{\parallel} is conserved throughout all three steps of the photoemission process:

$$\mathbf{k}_{\parallel} = \mathbf{k}_{\parallel,i} = \mathbf{k}_{\parallel,f} = \mathbf{k}_{\parallel,v} \quad . \quad (2.22)$$

Therefore the emission angles that are measured in ARPES can be directly related to the two momentum components k_x and k_y of the initial state $|i\rangle$. It is not necessary to include \mathbf{G} at this point as long as it is included later on in the treatment of \mathbf{k}_{\perp} . A momentum transfer of \mathbf{G} can happen at any point in the entire process and does not affect the position of \mathbf{k} within the BZ. However, it is mandatory to include it at least at one point (e.g. \mathbf{k}_{\perp}) to allow all possible escape directions. The photon momentum is neglected here.

Since the binding energy of the initial state can be derived from the kinetic energy, the remaining component to fully determine the initial state $|E_i, \mathbf{k}\rangle$ is the perpendicular component of the momentum $\mathbf{k}_{\perp,i}$. A widely used approach to determine the $\mathbf{k}_{\perp,i}$ is the *free-electron final-state (FEFS)* model. It assumes that the potential can be approximated as constant for the final state. This way $|f\rangle$ can be directly mapped to the state of the emitted electron $|v\rangle$ by introducing the phenomenological *inner potential* V_0 .

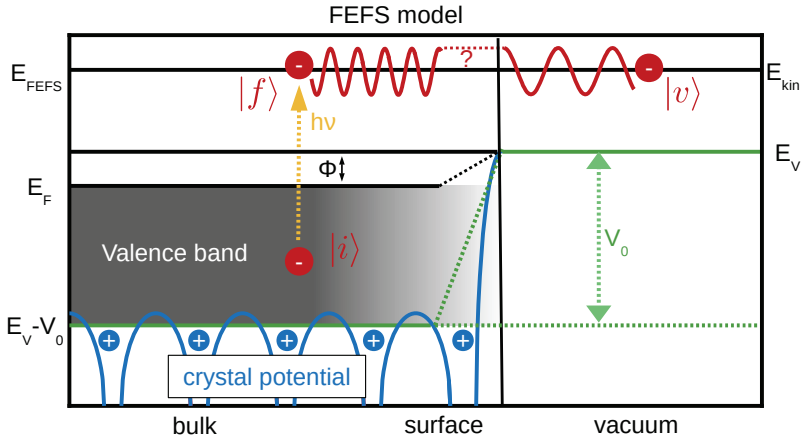


Figure 2.9: Illustration of the FEFS model of the photoemission process. The process of the surface transition is modeled by mapping the free-electron state in vacuum $|v\rangle$ directly to a quasi-free-electron state $|f\rangle$ inside the crystal with the constant inner potential V_0 .

Figure 2.9 sketches the three-step-process according to the FEFS model. The inner potential is the effective zero level of the FEFS and results in the following dispersion relation for $|f\rangle$:

$$E_{FEFS} = \frac{\hbar^2}{2m_e} (\mathbf{k}_f + \mathbf{G})^2 - V_0 \quad . \quad (2.23)$$

Assuming the conservation of \mathbf{k}_{\parallel} one can treat the reduction of the kinetic energy by overcoming ϕ purely with a reduction of k_{\perp} with the following result:

$$k_{\perp,i} = \sqrt{\frac{2m_e}{\hbar^2} (E_{kin} + V_0) - (\mathbf{k}_{\parallel} + \mathbf{G})^2} \quad . \quad (2.24)$$

Therefore, the FEFS model allows one to probe the three-dimensional electronic band structure $E_{bin}(\mathbf{k})$. However, due to the reciprocal lattice vector it contains the possibility of more than one value of k_{\perp} contributing to the photoemission signal for the same emission angle. Nevertheless, because of the dispersion the change in k_{\perp} is usually accompanied with a different binding energy, and often the bands can be uniquely identified by careful comparison to band structure calculations.

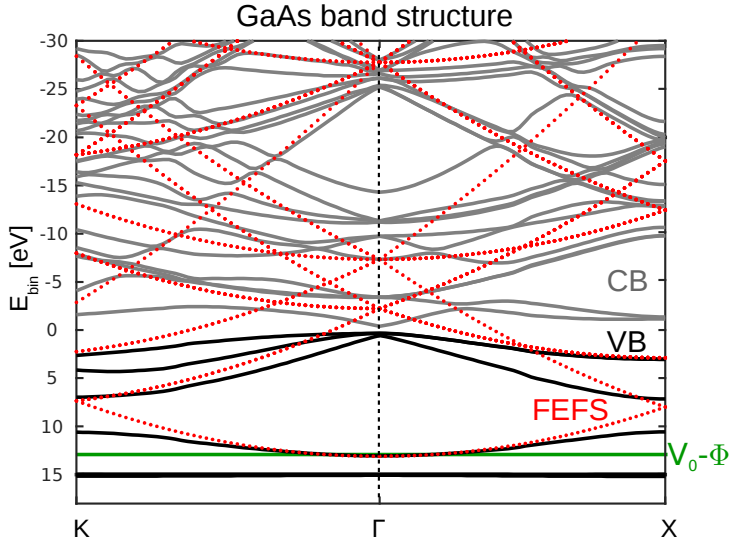


Figure 2.10: DFT calculation of the GaAs band structure overlaid with the FEFS bands, which consists of one paraboloid centered at each Γ point of the fcc-lattice. The DFT calculation was performed using Wien2k.

The inner potential V_0 is usually determined by optimizing the agreement of the experimental data with the calculated band structure, but often it can easily be estimated by comparing the band structure to the free electron dispersion. In figure 2.10 this is shown for the example of GaAs. One can immediately spot a high degree of overlap of the FEFS bands to the band structure that was calculated using DFT. One can also see that the agreement increases with higher kinetic energy since the crystal potential becomes less significant. Therefore, the FEFS model is generally a better approximation for experiments that are performed with high photon energies.

The sharpness of the k_{\perp} selection according to the FEFS model is often limited by the probing depth of photoemission. Due to the low IMFP λ the photoemission signal stems from a projection of the initial state wave function onto the surface near region, which cannot be a k_{\perp} eigenstate. The k_{\perp} resolution can be estimated with the uncertainty principle:

$$\Delta k_{\perp} \approx \frac{1}{\lambda} \quad (2.25)$$

The spatial resolution of ARPES in the lateral direction is by far too low to significantly add to the uncertainty of the parallel momentum component. The \mathbf{k}_{\parallel} -resolution is only limited by the resolution of the instrument and by the sample homogeneity. Defects, surface steps, and contaminations, lead to diffuse scattering and therefore reduce the \mathbf{k}_{\parallel} resolution, and increase the background signal in the spectrum.

Van der Waals materials

The two materials that are in the focus of this thesis are MoS_2 and ReS_2 . Their crystal structure is depicted in figure 2.11. MoS_2 and ReS_2 are so-called van der Waals (vdW) materials, which consist of layered sections of covalently bound atoms, with the coupling of the layers to each other by the much weaker vdW interaction. This section will give a brief overview of the basic properties of vdW materials.

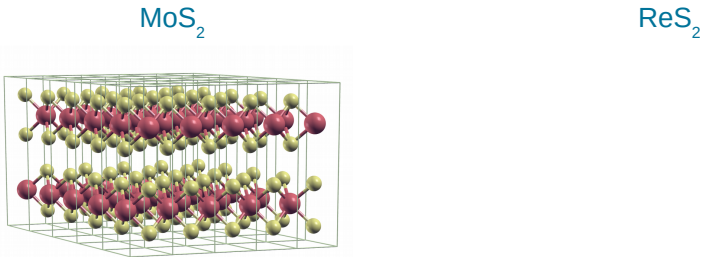


Figure 2.11: Crystal structure of MoS_2 and ReS_2 , each showing two monolayers.

The van der Waals interaction

Van der Waals interaction is an umbrella term for several types of dipole forces between atoms or molecules. They are usually categorized in three groups: interaction of two permanent dipoles (Keesom force), of one permanent and one induced dipole (Debye force), or the so-called *London dispersion force* [65, 66]. The latter describes the interaction of instantaneous dipoles, which are induced by quantum fluctuations. One can easily imagine that the deep, quantum mechanical roots of such effects make their behavior highly dependent on the system. In the case of molecular interaction, the vdW force can often be approximated within power laws such as the R^{-6} scaling with the distance R of two point particles [67], or the R^{-3} dependence for a molecule over a surface [68].

In solid state physics and in the context of the electronic band structure the proper inclusion of the London dispersion force, which has no classical interpretation, is still challenging today [10, 69]. As it was introduced in section 2.3, the most successful quantum mechanical model for crystal properties is DFT. These numerical

methods usually rely on the LDA or the GGA approximation, which assume a purely local energy functional $E[n(\mathbf{r})]$. The vdW interaction, however, stems from a non-local correlation: the coupling of spatially separated, instantaneous dipoles, and is therefore contrary to the LDA and the GGA [10, 70]. For the correct modeling of properties such as the interlayer spacing or vibrational behavior of vdW materials, the formulation of non-local energy functionals is required [69, 71, 72]. Therefore, the band structure calculations presented within this thesis, which are based on the GGA, rely on the experimental literature values for the crystal structure of the layered materials, instead of relaxing it numerically.

Layered crystals

The layered nature of vdW materials has a vast range of consequences. Mechanically the vdW gap represents an ideal predetermined mechanical breaking point. Cleaving crystals such as graphite and transition metal dichalcogenides (TMDCs) can easily be performed with ordinary adhesive tape, leaving the layer structure intact. This method is very convenient in surface science, because it can be performed in UHV, in order to produce atomically clean, well-defined surfaces [73, 74].

In non-vdW crystals the lack of bonding partners for the atoms at the surface usually causes a *surface relaxation*, which leads to deviations from the bulk lattice constant in the surface near region. In some cases surfaces even form significantly different lattices compared to the bulk in a so-call *surface reconstruction*, such as the well-known “herringbone pattern” of the Au(111) surface [75]. In vdW materials such effects are insignificant in most cases. However, absence of a structural change does not mean that the surface does not influence the electronic structure. The breaking of the bulk translational symmetry alone can have a drastic influence, and one famous example is the topological surface state of layered crystals such as Bi_2Te_3 [76].

The saturation of all covalent bonds makes the surface of vdW materials extremely inert [77]. Therefore, graphite/graphene, TMDCs, and numerous other layered materials usually do not form covalent bonds at the interface to other materials. This makes vdW materials an interesting choice for the creation of heterostructures with a minimal impact on the structural and chemical properties of the components [78].

Atomically thin materials

The high strength of the covalent bonds compared to the weak interlayer coupling suggests that the layers in bulk vdW crystals are already largely decoupled, and should share most of the properties of their atomically thin counterparts. However, especially the research regarding graphene, which has been awarded with the Nobel prize in 2010 [7], demonstrated that reaching the two-dimensional limit of the material is accompanied with the appearance of new physical phenomena. For instance the charge carriers in graphene have a linear dispersion relation, and therefore behave like relativistic, massless particles [79].

Creating atomically thin layers from vdW materials is very straightforward. By simply pulling adhesive tape off the surface of a layered crystal, and pushing the cleaved material down on a substrate, one distributes a large number of crystal flakes of varying shape, size, and thickness over the substrate surface. The chances to find atomically thin layers, also called monolayers, with a lateral size of several ten μm , is quite high [9]. The ease at which the graphene preparation could be reproduced and adapted for other vdW materials enabled a widely spread research activity in this new field. These mechanical exfoliation techniques have been refined to allow for instance the placement of few- and monolayer flakes with sub micrometer precision to create vdW heterostructures [80]. Although, these preparation techniques have proven sufficient for numerous research applications and prototype devices such as transistors [12, 13] and solar cells [16, 32], they lack the scalability and reliability for most device applications. For large scale monolayer films, chemical vapor deposition (CVD) seems to be a promising alternative to mechanical exfoliation. In recent years numerous vdW materials have been successfully grown, not only as monolayers [81–83], but also as vdW heterostructures [84–87]. Both, CVD and mechanical exfoliation, are widely used for sample preparation in research.

Transition metal dichalcogenides

Aside from graphene, the most frequently studied vdW materials are the TMDCs with the formula MX_2 , where M is a transition metal and X a chalcogenide. Unlike graphene, which is semimetallic, most TMDCs, including MoS_2 and ReS_2 , are semiconductors, and they retain this property when they are thinned down to the monolayer limit. Graphene has an exceptionally high carrier mobility [88], which

is an advantageous property in numerous situations. However, analogous to classical electronics, the semiconducting monolayer MoS_2 outperforms graphene in terms of transistor applications [12], since graphene cannot effectively be switched to an off-state. This makes TMDCs a valuable addition in choice of materials for new, two-dimensional samples and devices.

A further property that sets TMDCs aside from graphene is the multi-atom basis of their crystal structure, which is in most cases accompanied by a reduced crystal symmetry. The crystal lattice of monolayer MoS_2 , for instance, has only a threefold rotational symmetry, leaving it non-centrosymmetric. In combination with the strong SOC mediated by the heavy transition metal atom, this gives rise to pronounced spin-splittings in the electronic structure, which will be a central topic in chapter 4. In general, this makes TMDCs an interesting choice in the field of spintronics [89]. Yet another suggested application for TMDCs is optoelectronics. Several TMDCs, including MoS_2 and ReS_2 , have band gaps in the optical range. This makes them suitable candidates for applications such as photovoltaics, light-emitting diodes (LEDs), photodetectors, and optical switches [90].

Experimental setup

The focus of this study is the investigation of the electronic band structure, and therefore angle-resolved photoemission spectroscopy (ARPES) is the technique of choice. This chapter will give an overview of the different experimental configurations that were used within this thesis to perform the ARPES experiments. Supplementary methods for sample characterization, such as reflectivity measurements, will be introduced briefly within the respective results section.

The extreme surface sensitivity of the ARPES technique requires an ultra-high vacuum (UHV) environment, with pressures preferably in the order of 10^{-10} mbar or better. On one hand the scattering of the photoelectrons with residual gas has to be avoided. However, the highest demands in terms of the vacuum conditions are set by the cleanliness of the sample surface, which is especially important for high resolution ARPES with photon energies in the vacuum ultraviolet (VUV) regime. As it was already discussed in chapter 2.4, the ARPES probing depth of only few Å results in an extreme influence of surface contaminations. As a necessity for all the ARPES setups that are described here, the entire sample environment, the electron optics and analyzers, and the detectors are placed within UHV chambers.

UHV systems demand a high amount of maintenance. This includes continuously running pumps such as turbomolecular pumps, ion getter pumps, or titanium sublimation pumps. Also it requires the *baking* of the entire setup to at least 120°C each time the vacuum chamber is vented or contaminated, mainly to evaporate adsorbed water molecules. UHV also limits the accessibility and mobility of components within the chamber. To align samples for the experiment, one either has to rely on bellows and magnetic couplings that allow manipulation from the outside, or on piezo actuators, which can be placed in vacuum for fine movement.

The majority of samples for ARPES experiments require in situ preparation to obtain a sufficiently clean surface. Therefore, all ARPES setups that were used within this work include specialized preparation chambers, that are directly attached to the photoemission chambers. The preparation chambers can perform standard UHV surface preparation methods such as argon sputtering, heating for degassing

and annealing of the samples, as well as in situ growth of thin films. An alternative approach for preparing a clean sample surface is to cleave a single crystal. For van der Waals (vdW) materials this technique is particularly straightforward, since the atomic layers can be lifted off with adhesive tape. The preparation chambers also include the equipment to perform low energy electron diffraction (LEED) and Auger electron spectroscopy (AES) to characterize the sample surface.

A useful consideration to judge whether the vacuum conditions are sufficient for the experiment, is to estimate the time frame in which contaminations accumulate on the sample surface. The so-called *sticking coefficient* gives the probability that a particle from the residual gas hitting the sample surface stays attached to it. A common assumption is a sticking coefficient of 1. In this case it only takes ≈ 1 ns at atmospheric pressure to build up one monolayer of surface contamination. At $1 \cdot 10^{-10}$ mbar the time frame is already ≈ 3 hours. In reality the sticking coefficient depends on the sample material, the surface properties, and its temperature, as well as on the composition of the residual gas. For highly reactive metal films a sticking coefficient close to 1 seems to be quite realistic. However, for the transition metal dichalcogenide (TMDC) samples that are discussed in this thesis the accumulation of surface contaminations is exceptionally slow. Initial tests have revealed that even samples that were cleaved in air and immediately put into vacuum showed sharp LEED patterns and ARPES spectra without additional cleaning, which are both indications of a clean surface. Therefore, it is safe to assume that no significant contamination from the residual gas has build up under UHV conditions for the entire duration of the experiment.

ARPES setup at PGI-6

The ARPES experiment at Peter Grünberg Institut 6 (PGI-6) is designed to perform band mapping at high energy and momentum resolution [91]. It employs a variety of lab-based light sources and UHV sample preparation techniques. A very detailed characterization of the full system can be found in the dissertation of Markus Eschbach [92].

UHV system

Figure 3.1 shows the schematic of the ARPES setup. The electron analyzer is mounted at a UHV system that consists of three chambers: the main chamber, the preparation chamber, and the load lock. All chambers are directly connected but can be sealed from each other, and individually pumped or vented. Each chamber has one turbomolecular pump attached to it providing the main pumping capacity. On demand the main chamber can employ a titanium sublimation pump to provide further pumping power. The back side of these pumps is connected to the pre-vacuum system, which consists of a second stage turbomolecular pump followed by

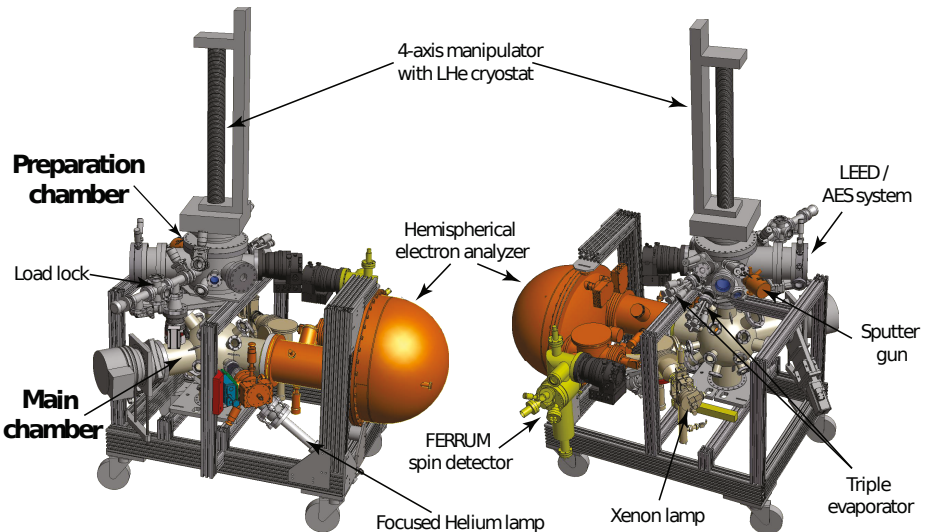


Figure 3.1: Schematic of the lab-based ARPES system at PGI-6 from two perspectives (Courtesy of B. Küpper).

an oil free scroll pump. The base pressure of the chamber is $< 1 \cdot 10^{-10}$ mbar, but can vary depending on the operating conditions. While the cryostat is in use, the cold surfaces improve the vacuum noticeably by adsorbing residual gas. However, a cooled sample also has a higher sticking coefficient, which usually leads to a faster buildup of contaminations despite the better vacuum. For the studied TMDC samples, it is safe to assume that the vacuum conditions are more than sufficient to avoid significant sample contaminations.

The load lock was designed as small as possible to minimize the volume that has to be vented when a new sample is introduced into the system. After the sample is transferred via a wobble stick from the load lock to the central 4-axis sample manipulator the load lock is sealed from the preparation chamber again. On its tip the manipulator carries a copper sample holder, which is depicted in figure 3.2. It has two slots for

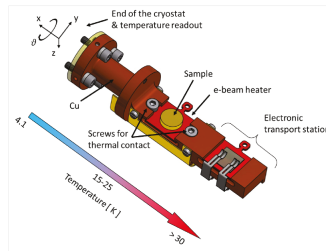


Figure 3.2: Schematic of the sample holder at the tip of the main manipulator (Courtesy of B. Küpper) capable of taking two Omicron sample mounting plates (one with e-beam heater, one with two electric contacts for electric transport measurements). It is mounted at the end of the LHe cryostat. The cooling efficiency along the holder is indicated by the arrow.

Omicron type sample mounting plates that can be easily moved with the wobble stick. The sample holder is placed directly at the end of a liquid helium cryostat, which is integrated into the manipulator. Figure 3.2 also indicates the cooling efficiency along the sample holder. The first sample slot is the main position for ARPES experiments. It is equipped with two screws that can be tightened with a vacuum screwdriver, which is mounted at the preparation chamber. The screws secure the sample during manipulator movements and for example during in situ cleaving of single crystals. They also increase the thermal contact of the Omicron plate to the copper sample holder. The only integrated temperature readout is at the end of the cryostat. However, by fitting the Fermi-Dirac-distribution to ARPES spectra, the temperature of the sample itself has been confirmed to be ≈ 25 K, which allows for ARPES measurements with high energy resolution, and low background signal [92].

In addition this sample slot has an integrated electron beam heater. An opening in the copper sample holder behind the sample slot directly exposes the Omicron

plate to a tungsten filament. Sending a current through the filament results in the emission of electrons, which are then accelerated by an additional high voltage between the filament and the Omicron plate. This allows for a direct electron bombardment of the back side of the sample plate. Temperatures up to 500 - 600°C can be reached easily by this method. To control the temperature an infrared pyrometer is used in combination with a ZnSe viewport, which is installed at the preparation chamber. The e-beam heater allows for efficient degassing and annealing, which are essential for UHV sample preparation. The second sample stage is equipped with two electrical contacts, and allows for in situ electrical transport measurements in combination with ARPES. With its large, vertical bellow the manipulator is designed to reach all relevant sample positions both within the preparation chamber and the main ARPES chamber, which are placed on top of each other.

This system is designed to achieve a high angle and energy resolution at low kinetic energies of the photoelectrons. The slow electrons are extremely susceptible even to small electric and magnetic fields, which distort their angular distribution or might change their kinetic energy. To avoid these issues, the use of magnetic materials is reduced to a minimum. Hot cathode vacuum gauges are used instead of magnetic gauges, and no ion getter pumps are used, because of their high electric and magnetic fields. The only magnet of the setup belongs to the argon sputter gun and is removed before the photoemission experiment. Also insulators are avoided in the immediate proximity of the sample. In case of illumination of materials such as ceramics by VUV light the photoeffect can build up a heavy, electrostatic charge, that can hardly discharge under vacuum conditions.

To judge the significance of a magnetic fields for the photoelectrons's trajectories one can calculate the Larmor radius [93]. For a typical kinetic energy of 16 eV even fields as weak as Earth's geomagnetic field, which has a strength of $\approx 30 \mu\text{T}$, leads to a Larmor radius of $\approx 45 \text{ cm}$, and can have a noticeable impact on the experiment. To reduce the influence of external magnetic fields, the main chamber is constructed from a so-called μ -metal. Its high magnetic permeability reduces the magnetic field within the chamber to only few nT [92], effectively shielding the photoelectron trajectories.

Light sources

The main chamber of the ARPES setup is equipped with multiple light sources for the photoemission experiments to adapt to various spectral ranges. Figure 3.3 shows the geometry of the available sources for the photoemission with respect to the sample and the electron analyzer. All presented ARPES experiments that were performed at PGI-6 used the *HIS13 helium discharge lamp*, which is the most frequently used light source of the setup. Helium lamps are a standard equipment in ARPES laboratories, because of their sharp, intense, and well separated spectral lines. In the HIS13 lamp an electric arc within a helium atmosphere ignites a plasma, and the resulting electronic recombinations produce the characteristic discharge spectrum. Helium is one of the most favorable elements for gas discharge lamps because its two strongest spectral lines, $E_{He\ I\alpha} = 21.22$ eV and $E_{He\ II\alpha} = 40.81$ eV, are extremely narrow and orders of magnitude stronger than the remaining discharge spectrum [94]. Therefore, the lamp can be used for high energy resolution photoemission experiments without further filters or monochromators. One has to be aware of the fact, that for some materials the valence band spectrum from the He I line can overlap with the signal from shallow core levels that are excited by He II. For the studied MoS₂ samples this was, however, not the case and since He I is by far stronger, He II only contributes a negligible secondary electron background to the He I spectra.

As its name indicates, VUV light is absorbed by air, and therefore the light source has to be integrated within the vacuum system. However, the plasma discharge requires a helium pressure that is significantly above UHV. Therefore, the lamp is connected to the experimental chamber via two-stage differential pumping, which reduces the helium partial pressure in the main chamber to $\approx 5 \cdot 10^{-9}$ mbar during the experiment. This way the contamination of the sample is kept to a minimum, while the main concern is not the helium itself, since it is a noble gas, but the impurities within it.

To reduce the size of the beamspot, the incoming light from the helium lamp is focused onto the sample, as it is illustrated in figure 3.3. This is done by a toroidal mirror, which produces a beamspot size of ≈ 0.4 mm \times 0.7 mm on the sample. A small beamspot has multiple advantages for the ARPES experiments. It allows to selectively probe different areas of inhomogeneous samples. Also, the angular resolution benefits from a reduced beamspot size, since it minimizes the influence of

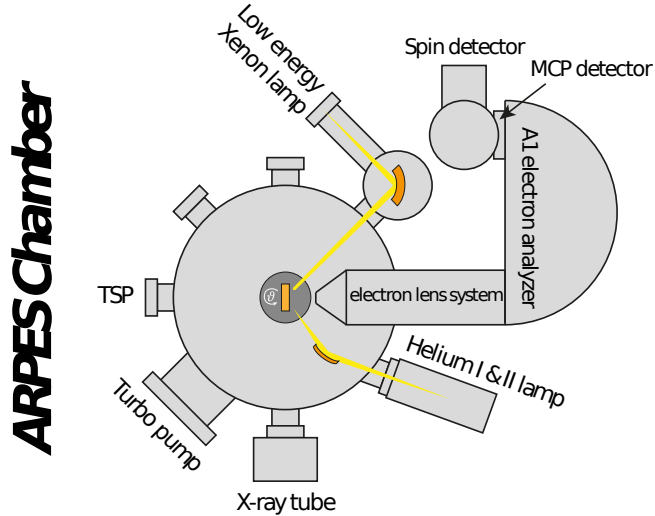


Figure 3.3: Simplified illustration of the main chamber of the ARPES setup at PGI-6 illustrating the geometry of the different light sources with respect to the sample and the electron analyzer (adapted from ref. [92]).

lens aberrations.

Further light sources, that were not employed within this thesis, are a micro wave-excited noble gas lamp, a Ti:sapphire laser system, and an x-ray tube. The noble gas lamp can be operated with different gases such as Xe, Kr, and Ar. This adds 8.44 eV, 10 eV, and 11.6 eV, respectively, as available photon energies [95]. Furthermore, this lamp is separated from the main chamber by a LiF window, allowing its operation without affecting the vacuum conditions of the main system. Its beamspot size, however, is with 1 - 2 mm larger than the spot of the He lamp. The Ti:sapphire laser system has been added recently to the system, and its thorough characterization can be found in the Masters's thesis of Pika Gospodarič [96]. It employs two stages of frequency doubling barium borate crystals to produce a photon energy of ≈ 6.02 eV. The main advantages of this light source are its high photon flux, and the possibility to use out-of-vacuum optical elements. The latter allow for focusing of the light down to ≈ 100 μm and for control of the light polarization. The x-ray tube can in principle be used for ARPES [97], but its main purpose is core level photoemission spectroscopy (PES) as means for a chemical analysis of the sample.

Analyzer and detector

The key component of the ARPES apparatus is the *MBS A1 analyzer*, which provides the simultaneous angular and energy resolution of the system. A schematic of the analyzer is shown in figure 3.4. The first element in the imaging process is a sequence of four electrostatic transfer lenses. Depending on the lens mode they project the angular or the spatial distribution of the photoelectrons across the entrance slit of the energy analyzer.

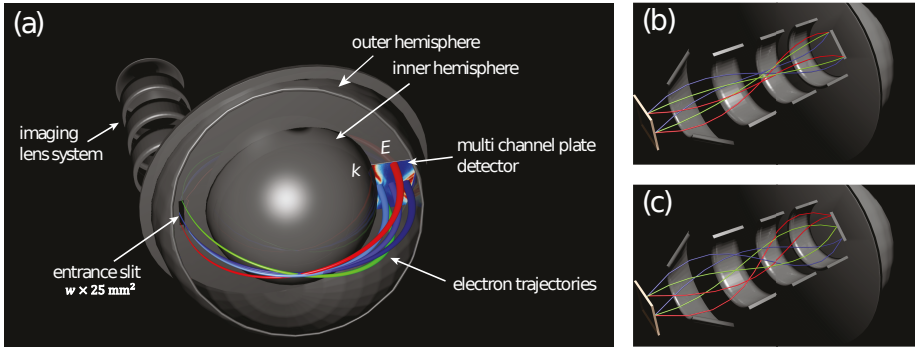


Figure 3.4: (a) Schematic of the electron lens system and the hemispherical analyzer, which image the photoelectrons onto a two-dimensional MCP detector. One detector dimension measures the kinetic energy distribution of the photoelectrons, the other direction their spatial (b) or angular (c) distribution, depending on the imaging lens mode. (adapted from ref. [92]).

The energy analyzer consists of a pair of hemispheres with a constant voltage difference applied between them, and therefore form a concentric capacitor. The electron deflection within the analyzer depends on their kinetic energy since electrons that are too fast or too slow hit the outer or inner inner hemisphere respectively. Only a certain energy window around the so-called *pass energy* E_p is transmitted from the entrance slit to the detector on the opposite side of the hemispheres. For the MBS A1 analyzer the transmitted energy range has a width of 10% of E_p . Photoelectrons with a certain initial kinetic energy can be decelerated or accelerated to the pass energy before they enter the analyzer, by varying the total potential difference between the sample, which is usually on ground, and the analyzer entrance slit. This way, the energy filter can transmit a wide range of initial kinetic energies to the detector.

A two-dimensional microchannel plate (MCP) detector is used to multiply and

detect the incoming photoelectrons. Since the transmitted energy range is distributed from low to high between the inner and outer hemisphere, this dimension of the detector image represents the kinetic energy of the photoelectrons. Orthogonally to this direction the initial distribution of the photoelectrons across the entrance slit is preserved by the imaging properties of the hemispherical design for slits much smaller than the hemisphere radius. Therefore, the two-dimensional image can be directly interpreted as the kinetic energy versus the angular or spatial distribution, depending on the lens mode.

Since the energy of the photoelectron is determined from the position where it reaches the detector, the resolution of the analyzer depends on a well-defined starting point of the electron trajectory, which is given by the width of the entrance slit w and its angular acceptance α . The energy resolution of the analyzer can be expressed as [98]:

$$\Delta E_A = E_p \cdot \left(\frac{w}{2R_m} + \frac{\alpha^2}{2} \right) \approx E_p \cdot \frac{w}{R_m} . \quad (3.1)$$

Here R_m is the mean radius of the two hemispheres, which is 20 cm for this setup. An additional aperture limits the angular acceptance, leading to the approximation $\alpha^2 \approx \frac{w}{2R_m}$. From equation 3.1 one can see that the resolution benefits from a low pass energy and a narrow entrance slit. However, the intensity scales linearly with w and roughly with E_p^2 [99]. Therefore, one usually chooses these parameters to match other factors that limit the total experimental resolution such as the line width of the photons or the sample temperature, to achieve a compromise between intensity and resolution.

Experimental conditions

Figure 3.5 (a) shows the typical geometry of the ARPES experiment. As it was discussed in section 2.4, the analysis of ARPES data relies on the photoelectron momentum components parallel to the surface, $k_{\parallel,x}$ and $k_{\parallel,y}$, which can be calculated from the angular distribution (see eq. 2.18). The angle ϕ , which is selected by the entrance slit direction and imaged onto the detector, directly relates to $k_{\parallel,x}$. The analyzer accepts a total range of $\pm 15^\circ$ for ϕ . By rotating the sample around the vertical manipulator axis, one can additionally vary the emission angle orthogonally to the entrance slit. In this way, the second photoelectron momentum component parallel to the surface $k_{\parallel,y}$ can be mapped as well. Figure 3.5 (b) shows this type of

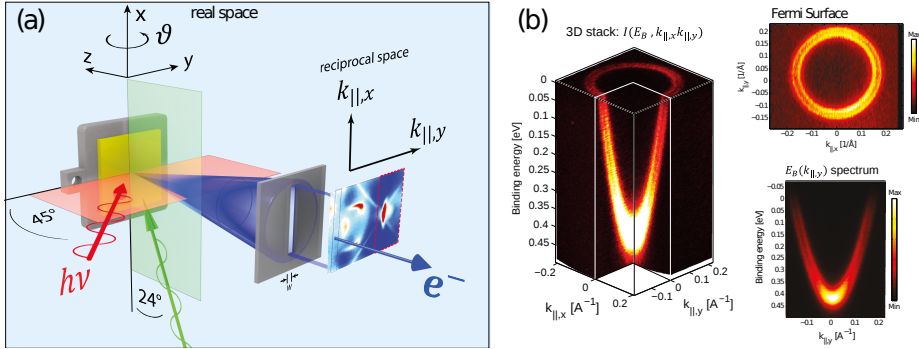


Figure 3.5: (a) Illustration of the typical experimental geometry of the ARPES setup. The angular distribution along the vertical entrance slit is imaged by the analyzer. By rotating the sample around the vertical manipulator axis, 2D k-space mapping is possible. The incidence direction of the He light is indicated in red, the light of the Xe lamp in green. (b) The 3D intensity map $I_{3D}(E_{bin}, k_{||,x}, k_{||,y})$, which was reconstructed from individual spectra $I_{2D}(E_{kin}, \phi)$ at different sample rotations θ , showing the he Au(111) surface state and its Rashba splitting (adapted from ref. [92]).

two-dimensional k-space mapping on the example of the Au(111) Shockley surface state. One can see the pronounced splitting of the parabolic state due to the Rashba effect, which is induced by the combination of spin-orbit coupling (SOC) and the symmetry breaking by the surface [100, 101]. The clear observation of the splitting is a benchmark for a high angular and energy resolution, as well as for good vacuum and sample preparation conditions.

The total experimental energy resolution is a combination of the line width of the photons $\Delta E_{h\nu}$, the analyzer resolution ΔE_A , and the thermal broadening of the spectrum due to the sample temperature ΔE_T . The three can be combined into the total resolution:

$$\Delta E_{tot} = \sqrt{\Delta E_{h\nu}^2 + \Delta E_A^2 + \Delta E_T^2} . \quad (3.2)$$

The square relation causes the largest uncertainty to dominate the total resolution. In order to estimate the thermal broadening one can use the sharpness of the Fermi-Dirac distribution, which was introduced in chapter 2.1. This leads to $\Delta E_T \approx 4 \cdot k_B T$. As room temperature corresponds to a thermal broadening of ≈ 100 meV, this often dominates the total resolution. At our setup the sample can be cooled down to ≈ 25 K, which leads to a significantly improved ΔE_T of ≈ 8 meV. Since the line width of the He discharge source is only ≈ 1 meV, and the width of the Xe line only

≈ 0.6 meV, even at these low temperatures $\Delta E_{h\nu}$ does not significantly contribute to ΔE_{tot} . Using a pass energy of 2 eV and an entrance slit width of 0.2 mm the analyzer resolution can be estimated according to equation 3.1 to be as low as 2 meV. Under these conditions a total energy resolution of 9 meV was observed in the experiment [92].

The momentum resolution Δk depends on the angular resolution of the instrument, and in addition it scales with the kinetic energy of the photoelectrons. As it was introduced in chapter 2.4, the parallel photoelectron momentum is given by $k_{\parallel} = \frac{1}{\hbar} \sqrt{2m_e E_{kin}} \cdot \sin \phi$. Therefore, at a fixed angular resolution $\Delta \phi$, Δk benefits from lower kinetic energies. $\Delta \phi$ has been experimentally determined from the sharpness of the Au(111) surface state to be $\approx 0.6^\circ$ [92]. For this example the Fermi level is observed at a kinetic energy of 17 eV, which corresponds to a momentum resolution of $\approx 0.022 \text{ \AA}^{-1}$.

Beamline 5 at DELTA

PGI-6 operates a further ARPES experiment placed at beamline 5 of the electron storage ring DELTA in Dortmund. The beamline is optimized for high photon fluxes with a high energy resolution in the VUV and soft x-ray regime. In addition to conventional ARPES experiments, a SPLEED spin-detector allows for spin-resolved ARPES experiments with simultaneous detection of the out-of-plane component and one in-plane component of the photoelectron's spin-polarization. It was used for all spin-resolved photoemission experiments that are presented in this thesis. At the time of these experiments beamline 5 had been the only setup of the institute with spin-resolution. Since then, both the lab-based ARPES setup in Jülich and the momentum microscope at ELETTRA, which will be introduced in section 3.3, have been upgraded with more efficient spin-detectors. Advantages of the setup at beamline 5 are that it is still the only ARPES experiment of the institute that offers the combination of a variable photon energy, which is not available for the lab-based light sources, and the detection of the out-of-plane spin-component, which is not possible in the momentum microscope.

The beamline

The source of the light at beamline 5 is the electromagnetic planar undulator U250. It produces “white¹” synchrotron radiation with linear polarization, which is then monochromatized and focused into the photoemission chamber by the beamline. The schematic of the beamline is depicted in figure 3.6. The beamline uses a set of curved mirrors to focus the light, while the horizontal and the vertical direction are handled individually.

For the vertical direction the first optical element is the plane grating monochromator (PGM). The unfocused undulator light is reflected from the plane premirror M2 of the monochromator onto the grating. The working principle of the PGM is based on the diffraction of the incoming light on a plane grating with a constant line spacing [104]. The grating serves as dispersive element, and refracts the white undulator spectrum at an angle that depends on the photon energy. Directly behind

¹The undulator already produces a spectrum with pronounced lines at variable photon energies [102]. However, the width of these lines is with several eV too high to consider them monochromatic in the context of ARPES experiments.

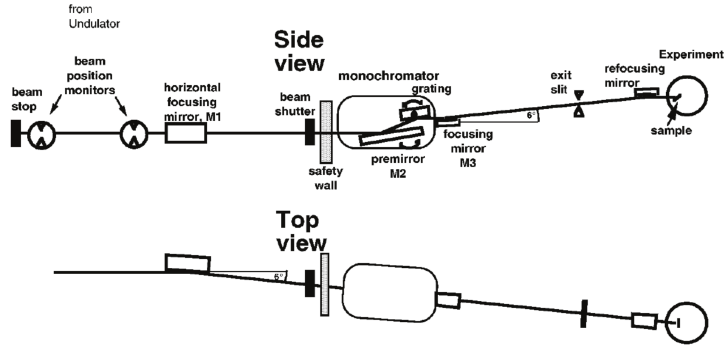


Figure 3.6: Schematic of the beamline in top and side view (adapted from ref. [103]).

the PGM the mirror M3 focuses the incoming light onto the *exit slit*, which selects the energy window that is transmitted to the experiment. The photon energy is varied by rotating the premirror M2 and the grating of the monochromator in a way that the desired energy is refracted into the forward direction. It is possible to switch between a grating with 300 lines/mm, which is optimized for the low photon energy range of $\approx 10 - 200$ eV, and a grating with 1200 lines/mm for the range of $\approx 200 - 1000$ eV. Typically the grating with 300 lines/mm is used, since the beamline provides the highest photon flux at low photon energies, and since the absolute line width of the light is proportional to the photon energy². Therefore, the 300 lines/mm grating is the preferred choice for high resolution ARPES experiments. Nevertheless, the energy range up to 1000 eV allows a chemical analysis of the sample by core level PES.

The exit slit selects the portion of the light, which was dispersed by the monochromator, and therefore its size is proportional to the spectral line width of the photons that are transmitted to the experiment. At the expense of intensity the beamline is in principle capable of producing light with a line width of only a few meV in the low photon energy regime. However, the total experimental resolution of this setup is usually limited by the thermal broadening of the spectrum of ≈ 100 meV since the measurements are performed at room temperature. Even with moderate exit slit sizes, which means at a high photon flux, this energy resolution is easily met by the beamline in the typical photon energy range for ARPES experiments.

²The relative line width $\Delta\nu/\nu$ is a constant for the PGM [104].

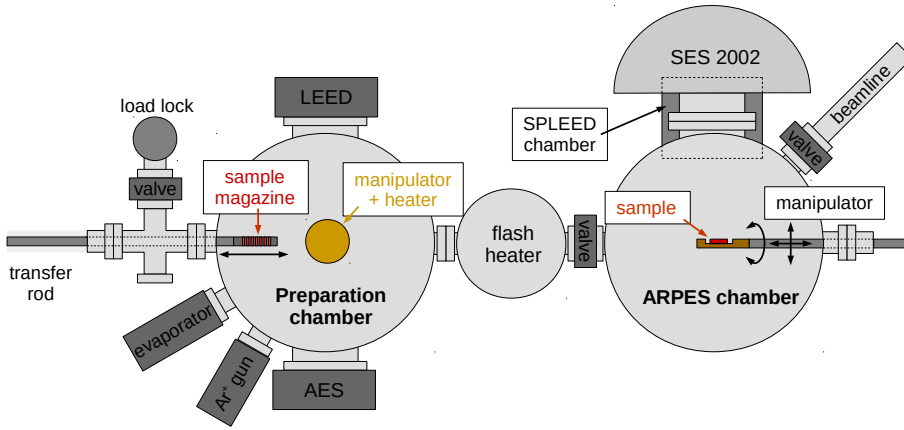


Figure 3.7: Simplified illustration of the UHV system. A transfer rod allows sample transfer between the PES chamber and the preparation chamber, which each have specialized manipulators.

In the vertical direction the last optical element is the refocusing mirror, which images the exit slit onto the sample. The refocusing produces a height of the beamspot on the sample of $\approx 300 \mu\text{m}$. For the horizontal direction there is only one optical element, which is the first mirror M1. It directly images the source point within the undulator onto the sample in the experiment chamber. The lack of horizontal refocusing results in a beamspot width of $> 3 \text{ mm}$. Apertures, which are placed at the exit slit and in front of the monochromator, can be used to reduce the width of the beamspot further, but at the expense of photon flux.

UHV system

As it was already discussed, ARPES experiments require UHV conditions. This applies to the beamline as well. It is directly connected to the experimental chamber and to the electron storage ring, which also has to be kept under UHV. During the experiments the ARPES chamber, the beamline, and the storage ring form one connected vacuum system. Therefore, the beamline is equipped with several automatic safety valves to prevent the venting of the entire system in case of a leak in one component, which would be fatal for the storage ring.

An illustration of the UHV system is depicted in figure 3.7. The experimental setup lines up along the transfer rod, which holds the sample magazine, and can

transfer samples between the load lock, the preparation chamber, the flash heating stage, and the ARPES chamber. In each chamber, a wobble stick is used to take samples from the transfer rod and to place them in the respective manipulator or sample stage.

The preparation chamber employs a 5-axis manipulator with an integrated, current heated tungsten filament, which allows annealing and degassing up to 600°C. Thermocouple sensors monitor the sample temperature. Furthermore, the chamber is equipped with an argon-ion sputter gun for sample cleaning, and e-beam evaporators for thin film growth. The LEED and the AES system provide the possibility for surface analysis. A separate flash heating stage, which can perform short time heating to temperatures $> 2300^\circ\text{C}$, is directly connected to the preparation chamber.

In the ARPES chamber the sample is transferred from the sample magazine onto the 4-axis manipulator, and the transfer rod can be retracted. This way the preparation and ARPES chamber can be separated from each other by a valve during the experiment. Both chambers are equipped with one turbomolecular pump, an ion pump, and a titanium sublimation pump. Under the electron analyzer an additional small chamber hosts the SPLEED spin-detector. This detector chamber has its own turbomolecular pump and an ion pump.

Conventional ARPES experiments

Regarding the conventional ARPES experiments this setup is similar to the lab-based system in Jülich, which was described in section 3.1. It uses a *VG Scienta SES-2002* hemispherical analyzer, which has a radius of 20 cm, and except for a lower angular acceptance of $\pm 7^\circ$ it can be considered equivalent to the MBS A1 analyzer, that was discussed in the context of the ARPES setup in Jülich. As it was already mentioned, the experiments at DELTA are performed at room temperature, which leads to a thermal broadening of the spectrum of ≈ 100 meV. Therefore, pass energies of 10 - 20 eV can be used for the measurements without a significant impact on the experimental resolution. The experimental geometry is similar, although the entrance slit is in the horizontal direction instead of vertical. However, the rotation axis of the manipulator is also horizontal, which allows the same type of two-dimensional k-space mapping that was described in section 3.1.

It is worth mentioning that the two-dimensional photoelectrons are detected by a delay line detector (DLD). Independent of this thesis the photoemission setup is

employed in a project that aims at pump-probe ARPES experiments using laser-driven higher harmonic generation of short pulses from the synchrotron [105]. The DLD is based on double-meander pattern delay lines, which couple capacitively to the back side of the MCP stack [106]. The delay lines provide an intrinsic time resolution eliminating the need of gating.

The SPLEED detector

The key feature of this setup relevant for this thesis is the possibility to perform spin-ARPES experiments using a SPLEED spin detector (*Focus GmbH*) [108]. It is based on the spin-orbit coupling (SOC) induced intensity modulation of electrons that are refracted from a tungsten single crystal. The photoelectrons are brought to a kinetic energy of 104.5 eV and focused onto a W(001) single crystal. Due to the strong SOC within this high Z element, the backscattered LEED reflexes undergo an intensity modulation, which depends on the spin-polarization of the incoming electron beam [108, 109]. Figure 3.8 (c) depicts the arrangement of four

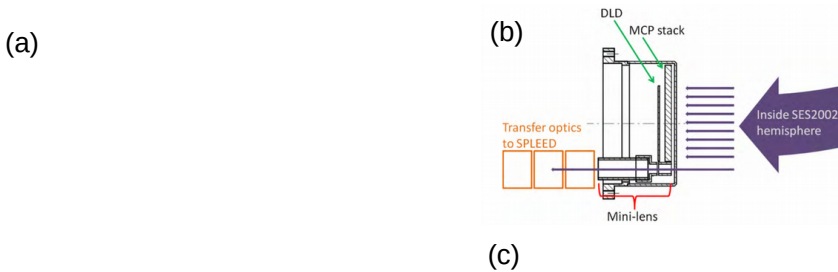


Figure 3.8: (a) Illustration of the spin-ARPES experiment at DELTA. (b) Transfer system at the conventional 2D-detector transmitting the photoelectrons to the SPLEED detector. (c) Principle of the SPLEED detector showing the arrangement of 4 channeltrons for the detection of photoelectrons, which were scattered on the W-crystal, providing the left, right, up, and down spin-channel (panels (b) and (c) adapted from ref. [107]).

channeltrons. They simultaneously measure the intensity I of the $(2,0)$, $(\bar{2},0)$, $(0,2)$, and $(0,\bar{2})$ LEED spots. The asymmetry of two opposing reflexes can then be used to deduce the spin-polarization P_x and P_y of the electron beam within the (100) and (010) directions of the W crystal:

$$P_x = \frac{1}{S} \cdot \frac{I_{(2,0)} - I_{(\bar{2},0)}}{I_{(2,0)} + I_{(\bar{2},0)}}, \quad P_y = \frac{1}{S} \cdot \frac{I_{(0,2)} - I_{(0,\bar{2})}}{I_{(0,2)} + I_{(0,\bar{2})}}. \quad (3.3)$$

The instrument specific *asymmetry function* $S = 0.25$ represents the degree of the intensity modulation that results from 100% spin-polarization. The SPLEED detector has a low figure of merit $S^2 \cdot I_{ref}/I_{in} < 10^{-3}$, which is a measure of detector efficiency. This makes the experiments very time consuming, even with the high photon flux of the undulator beamline.

The electron scattering is highly surface sensitive. Therefore, the W(001) surface must be very clean, and the SPLEED detector needs to be operated in a good UHV environment. In order to prepare a clean surface, the W surface is exposed to oxygen and flashed to 2300 K for 20 seconds. Under experimental conditions the crystal is flashed without oxygen approximately every two hours, and after about 8 hours the oxygen treatment is repeated.

Figure 3.8 shows the integration of the detector into the ARPES setup, which is described in detail in ref. [110]. Close to the DLD detector for the conventional ARPES experiments, the mini-lens transfers a portion of the photoelectrons via an electrostatic 90° deflector into the SPLEED detector. With such orientation of the W crystal, which is also presented in figure 3.8, the two analyzed spin components correspond to the sample normal direction, and to the horizontal direction within the sample plane.

Since the passing electrons are not further analyzed for their energy or their angular distribution, the resolution of the spin-polarized experiments is defined by the circular opening of the transfer lens with a 5 mm diameter. In the angular dimension the opening averages over an emission angle of $\pm 1.6^\circ$. The energy resolution of the SPLEED measurements depends on the pass energy. As it was discussed in section 3.1, lowering the pass energy narrows the energy range of the detector, but reduces the intensity in return. The low figure of merit of the SPLEED detector makes it impractical to measure at low pass energies. A compromise was chosen with $E_p = 20$ eV, which corresponds to an energy window of 150 meV within the transfer lens opening. The exit slit of the beamline and the entrance slit of the

analyzer were adjusted accordingly to optimize the intensity.

Momentum microscope at Elettra

PGI-6 operates a photoemission end-station with a modified *FOCUS NanoESCA* at the synchrotron facility Elettra in Trieste. The NanoESCA is a commercially available photoemission electron microscope (PEEM), which was designed to combine high spatial resolution imaging with simultaneous chemical analysis via photoemission spectroscopy [112]. From the point of view of this thesis the more compelling aspect of this machine is its capability to perform *k-space microscopy*. By imaging the Fourier plane of the energy filtered photoelectrons onto the detector instead of the real-space image, one can perform the analysis of E_{kin} versus \mathbf{k}_{\parallel} analogously to conventional ARPES. However, this setup can selectively measure an area of only few μm in diameter in momentum mode. This makes it a powerful tool for studying the electronic band structure of small, or inhomogeneous samples. Figure 3.9 shows the integration of the NanoESCA within the UHV system, which is permanently installed at an undulator beamline, which features a microfocused beam and variable polarization. A detailed characterization of the instrument can be found in the PhD thesis of Marten Patt [111].

The microscope column

The NanoESCA can be divided into three main sections: the microscope column, the energy filter, and the projection column. As figure 3.9 indicates, the microscope column can be used individually to perform conventional PEEM measurements. In this case the intensity is dominated by secondary electrons, which is for instance useful for x-ray absorption spectroscopy.

Figure 3.10 shows simplified photoelectron trajectories within the first optical elements of the microscope column for the three main operation modes. The first element is the objective lens. With the sample serving as a cathode, a strong electric field collects the photoelectrons from the entire solid angle above the sample surface, and accelerates them into the microscope. Already in the back focal plane of the objective a momentum image is formed. The coordinates within this image plane are directly proportional to the photoelectron momentum components parallel to the sample surface [113, 114]. Therefore, the PEEM is intrinsically capable of imaging the momentum distribution of the photoelectrons. However, for a meaningful interpretation regarding the electronic band structure, the energy filter is required.

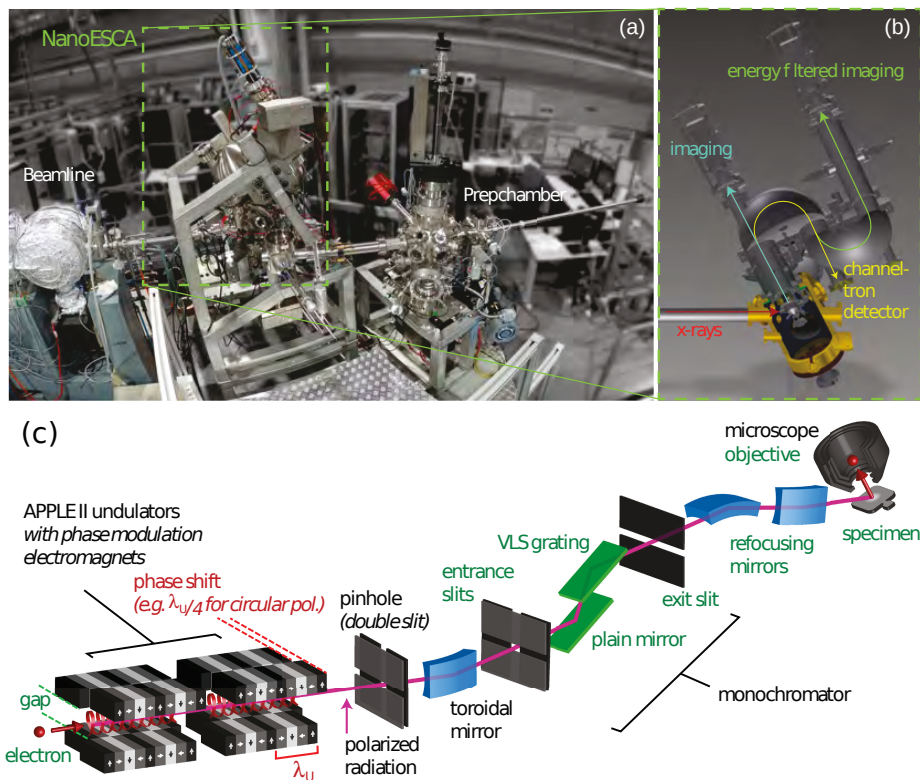


Figure 3.9: (a) Photography of the NanoESCA end-station at the synchrotron light source Elettra in Trieste, Italy. The *prep chamber* provides standard UHV surface preparation and characterization techniques. (b) Illustration of the NanoESCA showing the three stages for the photoelectron analysis: 1: conventional PEEM imaging, 2: channeltron for non-imaging PES measurements. 3: energy filtered PEEM for imaging PES and momentum microscopy. (c) Simplified schematic of the dual undulator beamline with microfocusing (adapted from ref. [111]).

The standard real space mode provides the highest magnification and spatial resolution [111]. For the momentum mode the first transfer lens should be operated in telescopic mode (see figure 3.10 (b) and (c)), which preserves the angular distribution of the trajectories. Regardless of the imaging mode, a momentum image is created in the plane of the *contrast aperture*, and a real space image at the *field aperture*. Therefore, the contrast aperture can be used to reduce the angular spread of the electrons, which reduces aberration effects, and increases the resolution in the real space mode. During the actual momentum mode measurements it is not used. However, it is convenient to adjust the NanoESCA for momentum measurements by

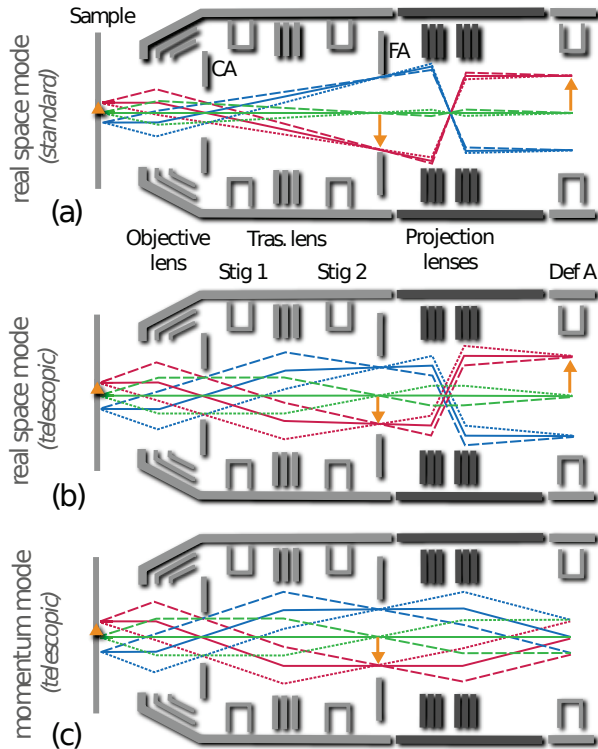


Figure 3.10: Illustration of the 3 standard imaging modes of the NanoESCA: (a) standard PEEM mode with the highest magnification and spatial resolution, (b) telescopic mode maintaining the angular distribution of the electrons, (c) momentum mode with the projective lens in Fourier mode. In all 3 modes the contrast aperture (CA) lies within Fourier plane and the field aperture (FA) within an image plane (taken from ref. [111]).

focusing on the real space image of the almost fully closed contrast aperture, which automatically means focusing within the momentum image plane of the photoelectrons. Since the beamspace is focused to $\approx 10 - 15 \mu\text{m}$, the size of the illuminated area already provides a decent spatial resolution in momentum mode. The field aperture can be used to improve this even further. It is positioned within an image plane, and can therefore reduce the field of view in real space. This way the probed area can be narrowed to a diameter $\approx 8 - 10 \mu\text{m}$.

The energy filter

Depending on the setting of the first projection lens, the microscope column can project either a real-space or a momentum image onto the entrance slit of the energy filter. A central issue of combining a PEEM with the usual, hemispherical analyzers, such as the ones of the ARPES setups at DELTA or in Jülich, is that the electrons at the exit of the hemisphere are energetically dispersed and suffer from the so-called α^2 aberration [115]. This problem can be overcome by the sequential use of two hemispheres in a point symmetric scheme. Due to the $1/r$ potential within the hemispheres the trajectories of the photoelectrons can be interpreted as Kepler ellipses. The dispersion and the α^2 aberration are at their maximum after 180° , which means after passing one hemisphere. By using a second hemisphere the full 360° cycle can be completed, and the photoelectrons are effectively brought back to their original spatial and momentum distribution [112, 114].

In a direct comparison to conventional ARPES this correction scheme pays for the image conservation to some extent with a loss in energy resolution. As it was described in section 3.1, classical ARPES setups exploit the dispersion along the hemisphere radius to gain additional resolution. However, a momentum microscope can compensate for this by adjusting the pass energy, which is proportional to the total energy window that is transmitted to the projection column. In momentum mode the NanoESCA operates at a pass energy of 50 eV, reaching an energy resolution of $\approx 100 \text{ meV}$, which is sufficient for a detailed band structure study while still maintaining a high transmission of the energy filter.

k-space imaging

The final stage of the NanoESCA operating in momentum mode is the projection column. It images the energy filtered photoelectrons onto the two-dimensional detec-

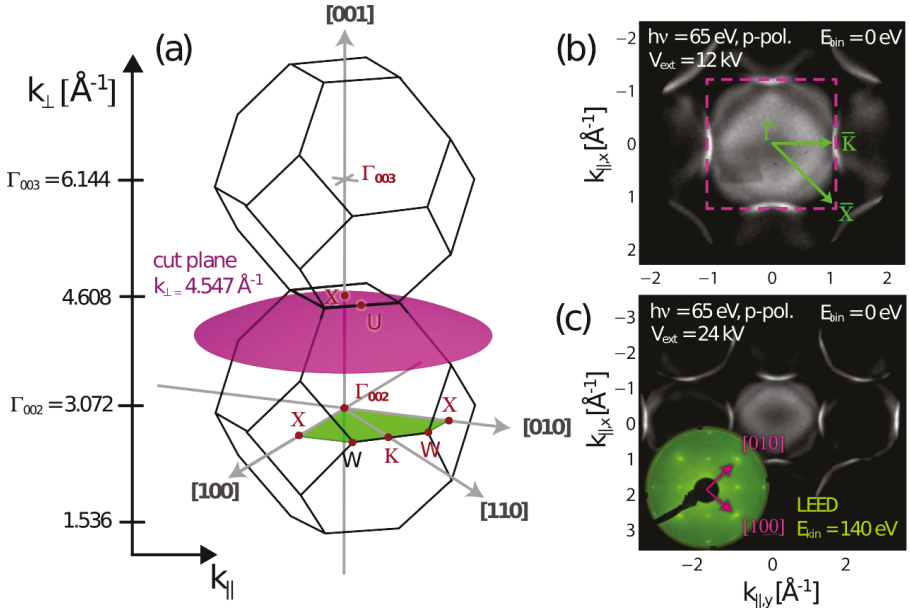


Figure 3.11: Measurement of a 2D Fermi surface of a Au(001) single crystal by the NanoESCA in momentum mode. Panel (a) indicates the position of the Fermi surface within the 3D Brillouin zone according to the FEFS model. Panels (b) and (c) show the Fermi surface as it is seen on the 2D detector at two different extractor voltages (taken from ref. [111]).

tor. Figure 3.11 depicts an exemplary measurement by the NanoESCA in momentum mode. Panels (b) and (c) show intensity maps as they are directly observed by the photoelectron detector. In this example the kinetic energy is adjusted to probe photoelectrons near the Fermi level, and the image can be interpreted as a portion of the Fermi surface, although the intensity is further modulated by the respective transition matrix elements. To measure a spectrum the filtered kinetic energy is scanned, and a three-dimensional data stack $I(k_x, k_y, E_{\text{kin}})$ is acquired. This makes the two-dimensional mapping of the full surface Brillouin zone (BZ) quite efficient in a momentum microscope, eliminating the need for sample rotation of conventional ARPES.

The hidden spin-polarization of 2H-MoS₂

Time reversal symmetry dictates that electronic states in a non-magnetic crystal cannot be spin-polarized unless the inversion symmetry is broken by the crystal structure. This general rule, called *Kramers degeneracy*, leads to the common opinion that there cannot be spin-polarization in a centrosymmetric crystal. MoS₂ is a van der Waals (vdW) material consisting of non-centrosymmetric layers. But, by an A-B stacking order the bulk crystal recovers inversion symmetry, leading to a globally centrosymmetric bulk space group. Therefore, it was usually concluded, that the symmetry breaking in freestanding monolayers allows for highly spin-polarized bands, but that this mechanism is forbidden in the bulk [30,116,117].

However, a recent publication by Zhang and Liu et al. [118] introduces a “hidden spin-polarization” that is derived from specific site asymmetries rather than from the crystal space group. This novel type of polarization has already been observed for other materials [119,120]. An argument that has been frequently brought up against the existence of spin-polarized states in bulk MoS₂ is the low circular polarization of the photoluminescence from even numbers of MoS₂ layers [89,116,121]. The fact that the circularity of the light was never fully quenched was usually disregarded as an artifact stemming from sample imperfections. However, recently Liu et al. [122] published first principle calculations, which support the interpretation that the observed circular photoluminescence response is in fact a result of the hidden spin-polarization. Therefore, its particular layered structure makes MoS₂ an ideal model material to study such effects. In this chapter it will be shown that although MoS₂ is a three-dimensional crystal, distinct parts of its electronic structure are completely confined within the plane of the monolayers, and that this confinement allows the electronic states to be dominated by the local symmetry breaking within the monolayers instead of the global space group. It will be shown that this results in **highly spin-polarized states in a centrosymmetric bulk crystal**.

All density functional theory (DFT) calculations that are presented in this chap-

ter were performed at PGI-1 by Irene Aguilera (bulk calculations) and Gustav Bihlmayer (monolayer and slab calculations) using the *FLEUR* software package [52]. A GGA exchange-correlation potential was used, and the lattice parameters were fixed at experimental literature values taken from Dickinson et al. [123].

Sample Properties

Macroscopic single crystals of MoS₂ with a diameter of several millimeters can be frequently found in ore deposits, which are usually referred to as *molybdenite*. Molybdenite is commonly mined as a source of elemental molybdenum, or used as a lubricant in its raw form. This makes MoS₂ crystals available in large quantities and at low costs, which further boosts its technological relevance. All MoS₂ crystals that were used in this thesis are natural mineral crystals that are commercially available from *SPI Supplies, USA*.

2H-MoS₂ crystal structure

MoS₂ crystallizes in covalently bound atomic S-Mo-S trilayers, which are referred to as one monolayer of the material. These monolayers are stacked to three-dimensional bulk crystals, and are only coupled by vdW interaction. Two crystal phases are common in nature: the hexagonal 2H-MoS₂ and the trigonal 3R-MoS₂, while the 2H-phase is dominant. Figure 4.1 depicts the crystal structure of 2H-MoS₂, which is the focus of this study. Although both phases share the monolayer structure and only vary in the vdW stacking order, from the point of view of this thesis the stacking order is of key importance because it changes the crystal symmetry.

The two-dimensional monolayer lattice is prismatic with a S-Mo-S basis, while the two S-atoms are equivalent since the center of the monolayer is a mirror plane. Therefore, monolayer-MoS₂ shares the 2D-crystal lattice of graphene with the characteristic honeycomb pattern. But unlike in graphene the inequivalent molybdenum and sulfur atoms of the basis reduce the rotational symmetry, which is now 3-fold instead of 6-fold.

The bulk unit cell of 3R-MoS₂ spans over three monolayers, which are translationally offset, but all have the same orientation with respect to each other. The result of this stacking is a trigonal bulk space group and therefore a 3-fold rotational symmetry, as the monolayer. On the contrary, the 2H-MoS₂ unit cell only contains

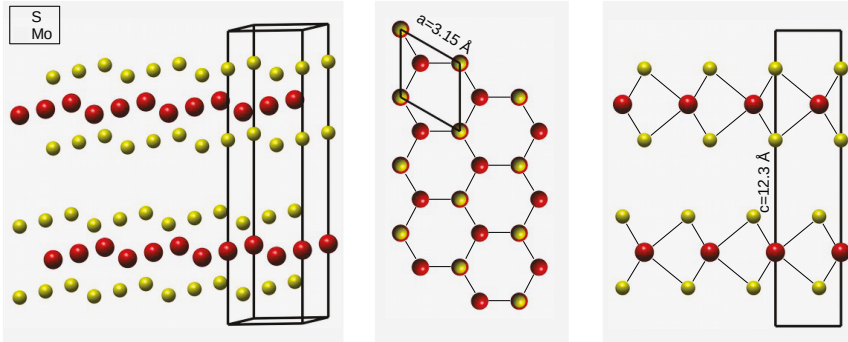


Figure 4.1: Crystal structure of 2H-MoS₂ including the primitive unit cell. In the middle and right panels the black lines indicate the covalent bonds within each monolayer.

two monolayers that are rotated by 180° with respect to each other. By this A-B stacking order 2H-MoS₂ gains a centrosymmetric space group, but also two possible terminations [30, 117], which will be discussed further below.

Cleavage behavior

The weak vdW interaction that holds the monolayers together in the bulk crystal makes MoS₂ an ideal candidate for cleaving via the so-called *scotch tape method*, which has been successfully employed on graphene. While the cleaving of non-vdW materials typically requires the application of heavy mechanical force, materials such as MoS₂ can be cleaved simply by pulling cohesive or scotch tape off the surface.

The cleavage process usually leaves a flake-like coverage of material on the scotch tape which consists of crystallites of varying lateral size and thickness, as seen in figure 4.2. The number of layers that are peeled off depends on the microscopic grain structure of the crystal and can range from thick bulk material to single monolayers. Nowadays using the cleaved-off material in a stamp-like manner is a well-established method for producing atomically thin films from layered crystals such as graphene or MoS₂. In this study, however, the remaining bulk single crystal was used for the experiment, not the cleaved-off part on the scotch tape.

Figure 4.2 (b) shows a scanning electron microscopy (SEM) image of a cleaved MoS₂ surface. One can immediately identify macroscopic, seemingly flat areas that are surrounded by sharp edges or partially cleaved-off material. To provide further

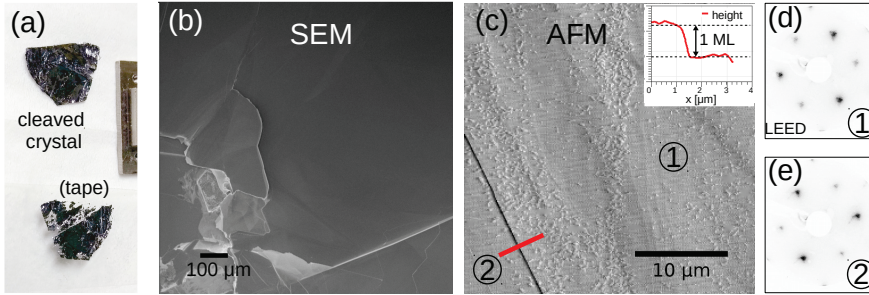


Figure 4.2: (a) Photo of cleaved MoS₂ single crystal and the cleaved-off material on the scotch tape. (b) SEM image of cleaved MoS₂ revealing extended, flat areas as well as rough edges with material sticking up. (c) AFM amplitude image that shows an extended, atomically flat terrace. The black line on the bottom left is a terrace boundary and the step height matches the thickness of 1 monolayer of MoS₂. (d)/(e) LEED images taken on two different positions on the sample. The 3-fold symmetry shows that a single type of surface termination is clearly dominant and the 180° difference between the two images corresponds to a position with the respective other type of termination.

magnification, atomic force microscopy (AFM) measurements were performed and showed that the cleaving process produced macroscopic, atomically flat terraces that are purely A- or B-terminated, reflecting the stacking order of the 2H-polytype. Figure 4.2 (c) shows the edge of such a terrace separating a large A-terminated area, that exceeds the field of view of the AFM, and a B-terminated area in the bottom left if the image. The height profile of the terrace edge matches the monolayer thickness of $\approx 6 \text{ \AA}$ while the numerous bright speckles in the image correspond to a height of less than $\approx 3 \text{ \AA}$ and are most likely adsorbates from air. It was already reported in earlier publications that MoS₂ produces exceptionally large, atomically flat terraces with a latitude of several hundred micrometers on its cleaved surface, which is a result of the exceptional mechanical strength of the monolayers [124]. Additionally the freshly cleaved surface is extremely clean. Therefore, applying the scotch tape method to MoS₂ is a suitable technique for preparing a surface that meets the demands of an angle-resolved photoemission spectroscopy (ARPES) study in terms of cleanliness and homogeneity. Furthermore, it can produce macroscopic areas of a single termination.

The AFM measurements were performed ex situ after the ARPES measurements. In the ultra-high vacuum (UHV) ARPES chamber the termination of the sample

was investigated by low energy electron diffraction (LEED). Figure 4.2 (d) shows the LEED images taken on an extended, flat area of the cleaved sample. The 3-fold symmetry of the LEED pattern shows that one type of termination is clearly dominant at this position. By moving the LEED spot on the sample it was possible to estimate that the area of the single termination extended over more than two millimeters. At the borders of the flat area the LEED spots either disappeared, were broadened or split into multiple broad spots. This behavior corresponds to areas of partially cleaved layers with random orientations of the surface normal as they can be seen in the SEM image in figure 4.2 (b). In a certain region adjacent to the flat area shown in figure 4.2 (d) a sharp transition into a 180° rotated LEED pattern was observed. This corresponds to a step edge of an odd number of monolayers, since the A- and B- type of layers have this stacking order. These observations with LEED support the interpretation of the sample surface with macroscopic, purely A- or B-terminated areas. ¹

Identification of the correct MoS₂ polytype

As it was already mentioned there exist two common polytypes of MoS₂. It is highly unlikely, but not impossible, that the commercially available crystals consist of the trigonal 3R-MoS₂ phase. The key statements in this chapter, however, are based on the assumption that the studied crystal consist of the centrosymmetric 2H-phase. An established, non destructive procedure of identifying the crystal phase of MoS₂ is to measure the optical reflectivity spectrum, the result of such measurement is shown in figure 4.3. The spectrum reveals two exciton transitions that are well known to be separated by 180 meV for 2H-MoS₂ compared to 140 meV for 3R-MoS₂ [31, 125, 126]. The reference data by Suzuki and Sakano et al. [31] shown for comparison agree well with our result. Although, the reference was taken on a synthetic crystal instead of a mineral the slight difference in the spectrum shape is most likely a result of a different spectrometer calibration, energy resolution, or background. This measurement is a solid proof that the conclusions in this chapter are based on measurements that were performed on the correct crystal phase, and

¹ On its own, this observation can also be explained by a less likely but possible scenario: due to its trigonal symmetry the 3R-MoS₂ phase should show a similar 3-fold LEED pattern regardless of the termination. The 180° reversal in LEED would then correspond to a 180° grain boundary. However, in combination with the other methods employed in this thesis, the 3R-phase can be ruled out.

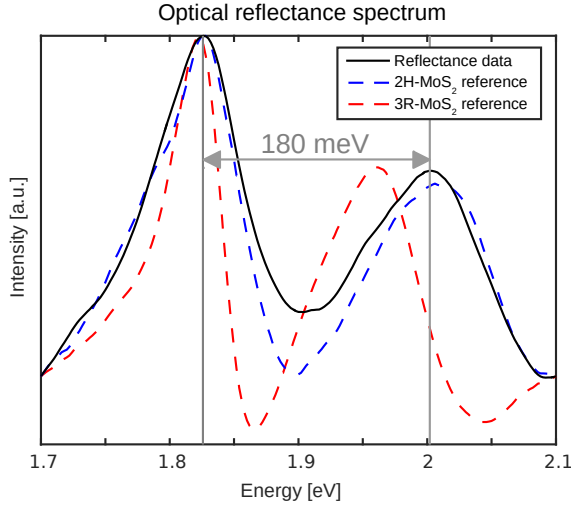


Figure 4.3: Optical reflectivity spectrum from the MoS₂ crystal (black curve). The separation of the two exciton transition peaks allows one to identify the crystal phase by comparison to reference data from ref [31] (red and blue curves).

additional evidence can be found in the photoemission data. The reflectance spectra were performed with an optical microscope with a tungsten krypton lamp coupled to an optic fiber as the illumination source. The reflected light was coupled with an optic fiber to the spectrometer with a spectral resolution of 0.5 nm.

2D electronic states in a 3D crystal

Since MoS₂ is a vdW material, it is to be expected that the strong hybridization due to the covalent bonds should lead to a high degree of electron delocalization within the monolayers. The interlayer interaction is by far weaker. This might lead to the assumption that the electronic structure of MoS₂ is largely the same in the bulk, at its surface, or in an isolated monolayer. However, it is known that when thinned down to the monolayer limit, the band structure of MoS₂ undergoes a transition from an indirect band gap to a larger, direct band gap [116, 127]. This transition has drastic consequences for the electric transport and optical behavior of the material. In this section it will be shown that while a portion of the electronic structure of MoS₂ participates in the interlayer coupling, other parts are rather isolated within the monolayers and can therefore be found unchanged in a freestanding monolayer as well as in the bulk.

Comparison to a freestanding monolayer

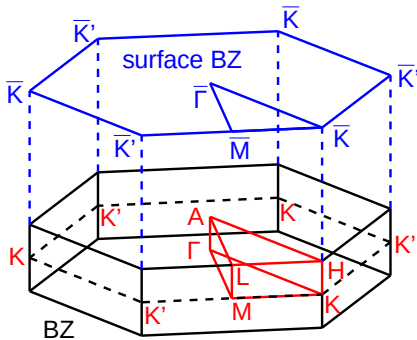


Figure 4.4: MoS₂ BZ (black) and with high symmetry points labeled (red), and surface BZ (blue).

A good starting point for the identification of two-dimensional states within the three-dimensional bulk band structure is to calculate the bulk projected band structure. Figure 4.4 shows both the bulk and the surface BZ of MoS₂. The surface BZ is the projection of the full bulk BZ onto the surface, and is equivalent to the plane of the monolayers. Figure 4.5 (a) shows the bulk band structure calculated by DFT for different values of k_{\perp} projected onto the surface BZ. The lack of dispersion is equivalent to a localized state. A two-dimensional state, which has no out-of-

plane dispersion, is projected onto a discrete energy, and forms a sharp band in the bulk projection. Since most bands are spread over a broad energy range, one can conclude that the majority of states in MoS₂ are delocalized in three dimensions.

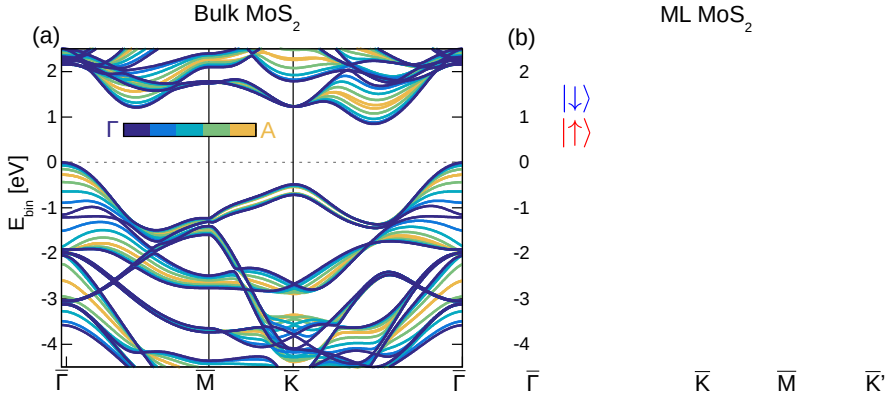


Figure 4.5: Band structure of bulk (a) and monolayer (b) MoS₂ calculated by DFT. The bulk band structure is projected onto the surface BZ and color coded for the out-of-plane dispersion. The colors of the monolayer bands represent their spin-polarization.

The out-of-plane dispersion is particularly strong for the valence band maximum at $\bar{\Gamma}$, and also for the conduction band minima within the lines $\bar{\Gamma}\bar{K}$ and $\bar{\Gamma}\bar{M}$. When the material is thinned down to the monolayer limit the entire out-of-plane dispersion is quenched by the confinement of the electrons within two dimensions. Figure 4.5 (b) shows the DFT calculations for a freestanding MoS₂ monolayer, which agrees well with previous studies [127, 128]. The comparison of the monolayer band structure to the bulk reveals that the highly dispersive states such as the valence band maximum and the conduction band minima are significantly altered by the forced confinement of the electronic states. As a result the binding energy of the topmost valence band at $\bar{\Gamma}$ shifts below the new valence band maximum at \bar{K} . This process is the origin of a well-known phenomenon in MoS₂: a drastic increase of the photoluminescence intensity in monolayer MoS₂, and an enlarged band gap of ≈ 1.8 eV compared to ≈ 1.6 eV in the bulk [116, 127].

Figure 4.6 shows ARPES data of a cleaved MoS₂ crystal, which is in good agreement with earlier band structure studies on this material [31, 129–131]. The measurements were performed with the ARPES setup at beamline 5 of DELTA, Dortmund, at a photon energy of 47 eV. Figure 4.6 (a) gives an overview of the entire three-dimensional dataset, where k_x represents the angle scale of the detector, and the second dimension k_y was obtained by rotating the sample. This way it is possible to

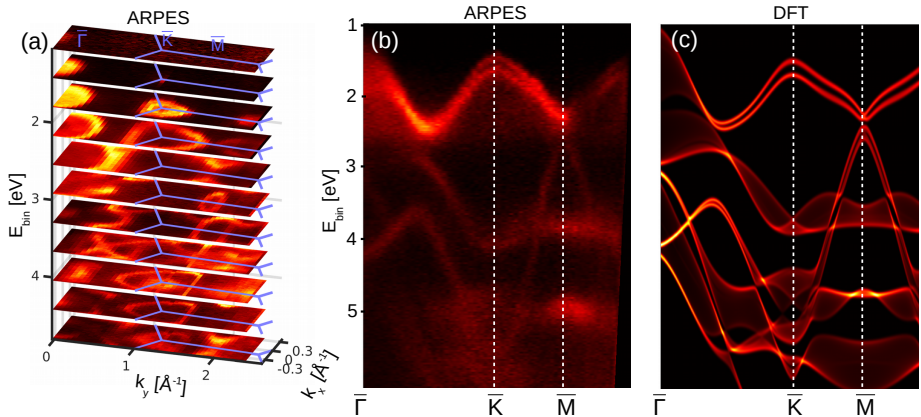


Figure 4.6: (a)/(b) ARPES data from a cleaved MoS₂ single crystal measured at DELTA with $h\nu = 47$ eV (c) bulk projected band structure calculated by DFT. In the calculation sharp bands indicate low out-of-plane dispersion. The Fermi level in (c) was adjusted for the best agreement with a).

reconstruct the $\bar{\Gamma}\text{KM}$ direction of the surface BZ, which is shown in figure 4.6 (b). The noise level in this figure is rather high and the resolution quite low. The main reasons for this are that the measurements were performed at room temperature, and that for the full range shown the sample had to be rotated from normal emission to $\approx 50^\circ$. The rotation is usually accompanied by a displacement of the beamspot on the sample, potentially losing the initially identified, flat surface region.

For a direct comparison to the bulk projected band structure, the DFT calculation was plotted for the same path in reciprocal space in figure 4.6 (c). Despite the limited data quality of this dataset one can find a good agreement of theory and experiment. It is peculiar that ARPES seems to probe the full bulk projection instead of a sharp point in k_\perp according to the free-electron final-state (FEFS) model, since only bands with a narrow projection appear sharp in the spectrum. This behavior can be explained with the low probing depth. As it was introduced in section 2.4, the uncertainty principle limits the sharpness of the k_\perp selection. According to the universal curve [62], at this kinetic energy range the inelastic mean free path (IMFP) is in the order of 2 \AA . Using equation 2.25 one can estimate the uncertainty of k_\perp to be $\approx 0.5 \text{ \AA}^{-1}$. Since the size of the MoS₂ BZ in the out-of-plane direction is only 0.5108 \AA^{-1} , a large part of the bulk projected band structure is probed by the experiment. In the ARPES spectrum in figure 4.6 (b) the valence band maximum at

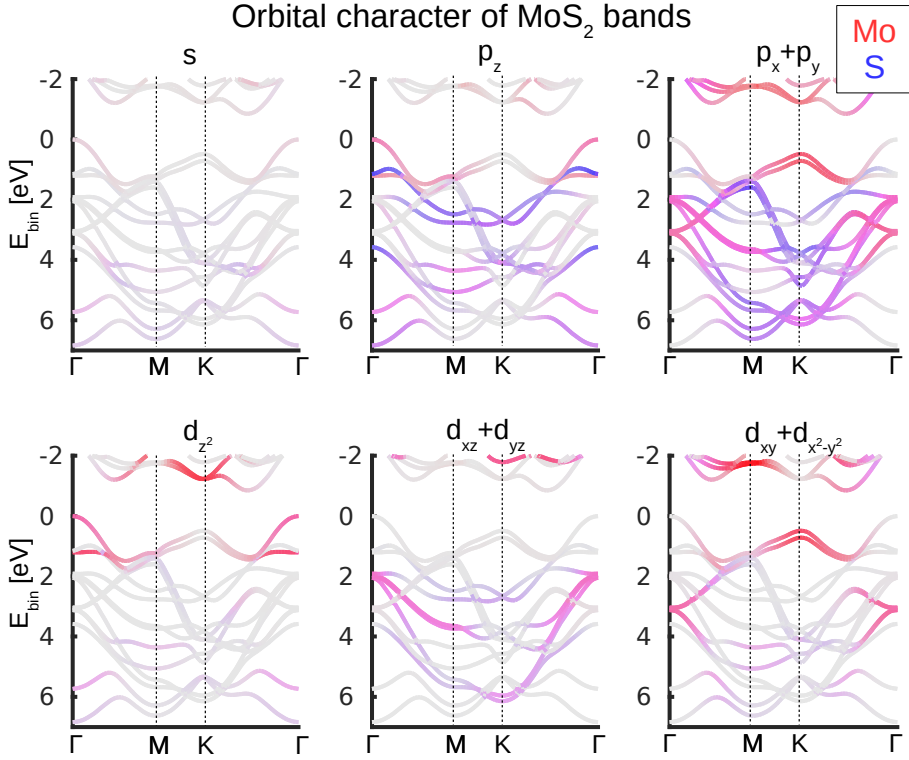


Figure 4.7: Projection of the calculated MoS₂ full band structure (gray) onto atomic orbitals with out-of-plane (left and middle column) and in-plane character (right column). In addition the bands are color coded for the projection onto atomic sites of Mo (red) and S (blue).

$\bar{\Gamma}$ appears to be lower compared to the bulk projection. With the enhanced contrast in figure 4.6 (a), however, it is obvious that the maximum is at the $\bar{\Gamma}$ point. Why the maximum appears lower is not entirely clear, but other studies have reported a similar behavior [130, 131]. While the k_{\perp} selection or the final state band structure can easily cause such intensity variations, it is also likely to be related to a drop of the local density of states at the immediate surface region, which will be discussed in section 4.2.3.

The valence band splitting at the \bar{K} point

The sharpness of the bands that are observed in ARPES is already an indication for the two-dimensional confinement of the states, since it is likely that a large part of the bulk projection is probed, and the width of the projection corresponds to the out-of-plane dispersion. In contrast to the broad bands at the $\bar{\Gamma}$ point the topmost valence band at the \bar{K} point is rather sharp and clearly split into two subbands. Due to their shape these bands are usually referred to as *valleys*, and are well-known to be highly spin-polarized in MoS₂ monolayers but are considered to be unpolarized in the bulk [30, 116, 117]. However, the sharp appearance of the bands in the ARPES data is the first clue that the valleys share the properties of those in the MoS₂ monolayers.

To investigate the character of the bands further it is possible to project the calculated eigenstates from DFT onto atomic orbitals. The result is shown in figure 4.7. One can see that valence and conduction bands mostly consist of p and d electrons. As expected, the bands that are delocalized in the k_{\perp} direction consist of orbitals with out-of-plane character. Especially the p_z and d_{z^2} , that form the valence band maximum, strongly delocalize over the vdW gap, which explains the renormalization of these states in freestanding monolayers. The valleys at the \bar{K} point, however, are formed purely by the p and d electrons of in-plane character. In addition to the orbital character, the bands in figure 4.7 are color coded for the projection into atomic sites. This projection was calculated by summing up the charge within spheres around each atomic position. From this, one can conclude that the valleys are almost completely localized at the molybdenum sites. This further shields them from adjacent layers, compared to sulfur orbitals, which can to some extent overlap with each other. Since the valleys do not contribute to the interlayer coupling they are hardly affected by the neighboring layers, and remain mostly unchanged when the material is thinned down.

The ARPES experiments were repeated in a similar fashion with the photoemission setup at PGI-6, and the results are shown in figure 4.8. This experiment was focused on the \bar{K} point, and the sample was oriented and aligned so that the \bar{KM} edge of the 1st BZ can be mapped with a minimum of sample rotation (k_y). The helium cryostat of this setup allowed the cooling of the sample to ≈ 25 K. The light source is a helium discharge lamp with a photon energy of 21.22 eV, which has a small, circular beamspot. It therefore allows better control of the illuminated, flat

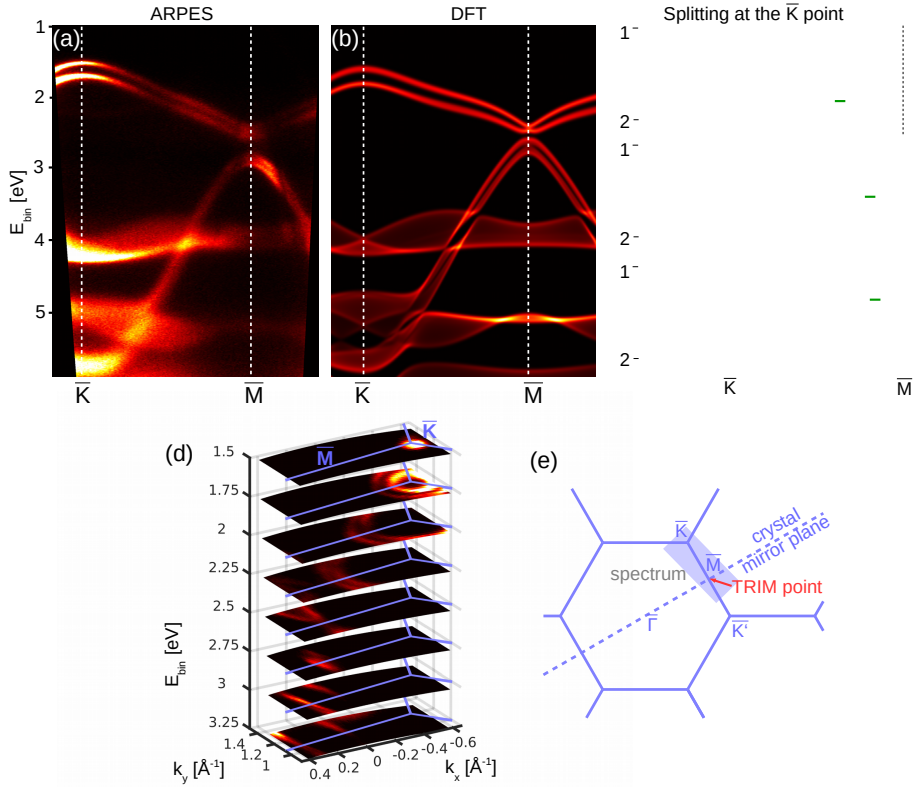


Figure 4.8: (a) ARPES data from the cleaved MoS₂ single crystal measured at PGI-6 with $h\nu = 21.2$ eV (b) bulk projected band structure calculated by DFT (c) valence band splitting at the \bar{K} point observed at different photon energies to map the out-of-plane direction KH (d) 3D representation of the obtained data set with the BZ edge marked in purple (e) position of the dataset in the surface BZ indicating the TRIM point \bar{M} , where the valence band splitting disappears in the spectra In the calculation sharp bands indicate low out-of-plane dispersion.

area. By these efforts it was possible to optimize the experiment for this particular region of the BZ, enabling a more detailed comparison of the valleys at the \bar{K} point to the DFT calculations than the results shown in figure 4.6.

In this data set the splitting of the valleys is more pronounced and one can observe that the subbands remain separated almost along the entire line $\bar{K}\bar{M}$. The size of the splitting is ≈ 180 meV. At the \bar{M} point the splitting disappears, and reopens on the other side in the $\bar{M}\bar{K}'$ direction. This behavior is an indication that the splitting is caused by the spin-orbit coupling (SOC), since \bar{M} is a time-reversal invariant momenta (TRIM) point of the BZ, where the spin-orbit-splitting is forbidden by the time-reversal symmetry.

The low background signal in the spectrum and the high energy resolution make it even clearer that the ARPES data is in remarkably good agreement with the bulk projected band structure. Therefore, it is very likely that the extremely sharp valence band splitting is a direct result of the two-dimensional character of the states. Nevertheless, the FEFS model, which was introduced in section 2.4, can be used to calculate the out-of-plane momentum component. In figure 4.8 (c) the valence band splitting is plotted for 3 different photon energies, sampling the out-of-plane direction KH, which corresponds to the \bar{K} point of the surface BZ. The fact that the size of the splitting remains unchanged proves that the valence band at the \bar{K} point is largely confined within two dimensions.

Surface electronic structure

When it comes to drawing conclusions about bulk properties, one of the central issues of ARPES is its extreme surface sensitivity. While it is possible to increase the probing depth by going towards the hard X-ray excitation regime, it will be shown later on that it is essential that the majority of the photoemission signal originates from the topmost monolayer, since the second layer has a different orientation. Therefore, this study benefits from the extreme surface sensitivity that results from the available photon energy range, but the impact of the surface on the interpretation of the data has to be taken into account.

As it was explained in section 2.5 the electronic bonds of each layer in vdW materials are fully saturated, and therefore no considerable structural surface relaxation is to be expected. However, the breaking of the out-of-plane translational symmetry alone is often enough to significantly alter the band structure. To investigate the

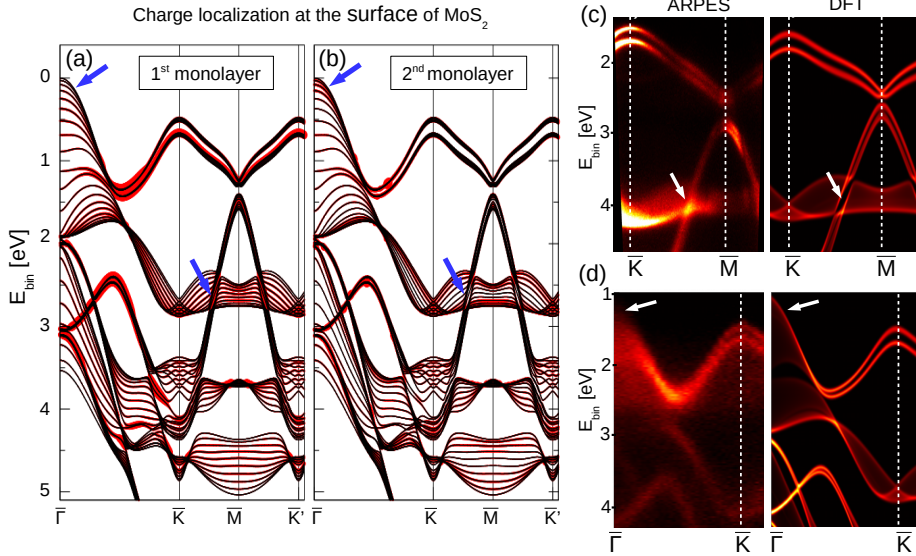


Figure 4.9: (a)/(b) Charge localization in the first and second MoS₂ surface layer from a 10-layer slab DFT calculation. The amount of charge in a state is illustrated by the size of the red envelope. (c)/(d) Magnification of the ARPES data and bulk projected DFT calculations from figures 4.8 and 4.6. The arrows point out areas with discrepancies between ARPES data and the bulk projection, that could be explained with the modification of the electronic structure by the surface.

influence of the surface, a 10-layer slab DFT calculation was performed, which is shown in figures 4.9 (a)/(b). It is not surprising that the slab band structure is almost identical to the bulk projection, which was shown before (figure 4.5). In addition to the energy eigenvalues it is possible to calculate layer-resolved charge densities within the slab. The size of the red envelope in figure 4.9 represent the charge density within in the surface layer and (4.9 (a)) and second layer (4.9 (b)). One can see that the charge density at the valence band maximum at $\bar{\Gamma}$ significantly drops in the surface layer, and similar findings have already been reported by others [130]. One can conclude that this is a result of the missing out-of-plane delocalization at the immediate surface, which is equivalent to the mechanism that causes the transition to a direct band gap in a freestanding monolayer. It is also likely that this mechanism contributes to the low photoemission intensity that can

be observed at the valence band maximum in figure 4.9 (d), which is a magnification of the spectrum from figure 4.6. Since the IMFP in the relevant kinetic energy range is only a few Å, the experiment is sensitive to such variations of the local density of states. However, it is not entirely evident that this a direct observation of the drop in the charge density. As it was explained before, the density of states is only one of many factors that determine the photoemission intensity, with other factors being k_{\perp} dispersion or dipole selection rules.

Apart from the intensity modulation at $\bar{\Gamma}$ the only apparent discrepancy between the ARPES spectrum and the bulk projected DFT calculation is highlighted in figure 4.9 (c). The bright spot in the ARPES spectrum lies within an area, for which the bulk projection predicts a gap in the band structure. However, in the slab calculation, which includes the surface, the area of the gap is filled with a band. Comparing the charge density of the first and second layer one can see that this state is entirely located at the surface. Taking this surface state into account the agreement of the ARPES data to the band structure calculations is extremely good. Since for the valleys at the \bar{K} point, ARPES, bulk projection, and slab calculation show the same band structure, one can assume that the observed properties are not exclusive to the surface, but also shared by the bulk.

Exclusion of the 3R phase

The reflectance measurements that were shown in figure 4.3 prove that the sample consists of the right crystal phase 2H-MoS₂. It is a commercially available single crystal and therefore it not to be expected that the sample is contaminated by the trigonal 3R-MoS₂ phase. Nevertheless, the probing depth of the optical reflectance is by far higher than that of ARPES and in an unlikely scenario there might be a 3R-contamination present at the surface. The best indication for the correct crystal phase is the size of the valence band splitting at the \bar{K} point, which is ≈ 180 meV in the ARPES spectrum. This splitting is also the origin of the two separate exciton transitions in the reflectance spectrum and therefore the two methods consistently point to 2H-MoS₂.

For further analysis the band structure of 3R-MoS₂ was calculated and compared to the ARPES data. Figures 4.10 (a)-(c) show a comparison of the spectrum to the bulk projected band structure of 2H-MoS₂ and 3R-MoS₂, calculated by DFT. The two band structures seem similar, which is not surprising, since they share the same

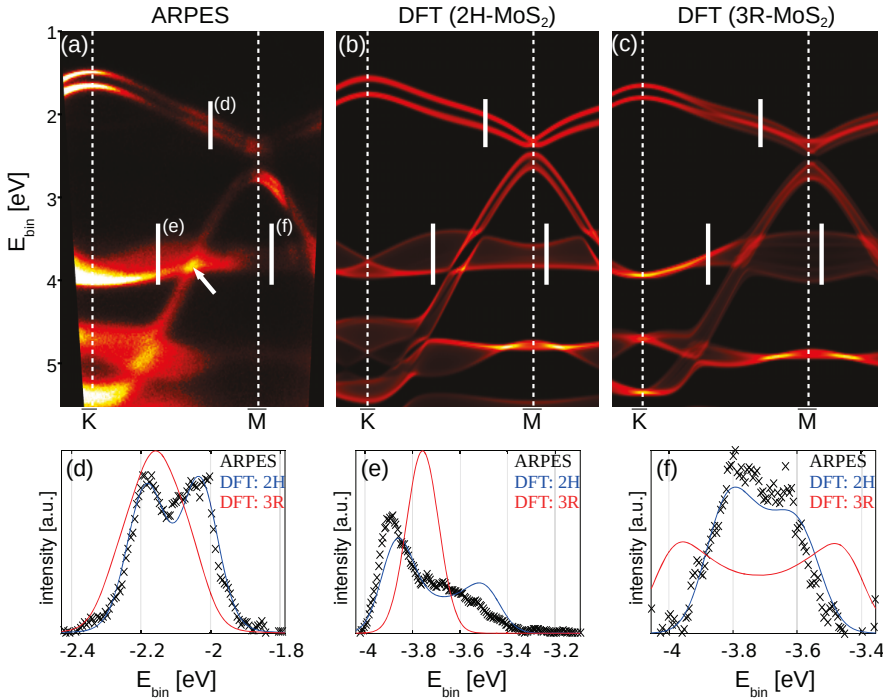


Figure 4.10: (a)-(c) Comparison of ARPES data to bulk projected DFT calculations for 2H-MoS₂ and 3R-MoS₂ (d)-(f) energy distribution curves from the regions that are marked with white bars in the spectrum and in the calculations. The white arrow in (a) points to the only region, where the 3R-MoS₂ band structure seems to agree to the ARPES data. This can be explained by a surface localized state in 2H-MoS₂.

monolayer crystal structure, where only the stacking order differs. At first sight the region that is marked with an arrow agrees better with the 3R-phase. However, this feature was identified as a surface state of 2H-MoS₂ earlier. Figures 4.10 (d)-(f) compare the energy distribution curves that were obtained from the areas that are marked with the white bars. The areas were selected because they on one hand show clear differences between the two phases in the calculated band structure and on the other hand do not show any surface specific reconstruction. Although, the bulk projection is not a photoemission simulation and ignores intensity variations due to the photoemission process, the striking deviation of the calculated band structure of the 3R phase from the experiment leaves no room for doubt that the sample was composed of the 2H-MoS₂ phase.

The hidden spin-polarization

The combination of time reversal symmetry and a centrosymmetric space group leads to the common conclusion that there cannot be spin-polarized bands in 2H-MoS₂. However, in this section it will be shown that the symmetry operations that are dictated by time reversal and the crystal space group, if applied correctly to MoS₂, leave room for the compensated type of spin-polarization that was introduced by Zhang and Liu et al. [118]. Using spin-ARPES experiments and DFT calculations it will be shown that the two-dimensional states, which were discussed in the previous section, are highly spin-polarized, but that the polarization is compensated within the crystal unit cell.

Quantum mechanical considerations

The SOC is capable of lifting the degeneracy between $|\uparrow\rangle$ and $|\downarrow\rangle$ states and is therefore a promising source of spin-polarized electronic states. It is textbook knowledge that SOC renormalizes the energy eigenvalues of atomic orbitals depending on its angular momentum L , leading to the *fine structure splitting*. However, since an atom is a fully rotational symmetric system, one can conclude that if $|L, \uparrow\rangle$ solves the wave equation, $|-L, \downarrow\rangle$ must be a degenerate solution. *The reality* from a quantum mechanical point of view is a linear combination of all solutions, and therefore an atom has no spontaneous spin-polarization despite the spin-dependent energy eigenvalue of each electronic state.

When it comes to analyzing the spin-polarization in a solid, similar considerations can be made, but they must be based on the crystal symmetry. *Kramers degeneracy* dictates that, in the absence of a magnetic field, in a centrosymmetric crystal for any Bloch state $|\mathbf{k}, \uparrow\rangle$ there is a degenerate state $|\mathbf{k}, \downarrow\rangle$. These basic considerations lead to the common assumption that crystals such as MoS₂ cannot be spin-polarized, and this is correct for the *net spin-polarization* of the complete unit cell. However, this conclusion neglects that the inversion operation $\mathbf{r} \rightarrow -\mathbf{r}$, which results in a centrosymmetric space group, maps any position outside the inversion center $\mathbf{r} = 0$ to a **different point in the unit cell**.

The consequence of this is illustrated in figure 4.11. MoS₂ is non-magnetic, and therefore time reversal symmetry applies. There must be degenerate solutions $|\mathbf{k}, \uparrow\rangle$ and $|\mathbf{k}, \downarrow\rangle$. However, unlike the time reversal, the inversion operation reverts the

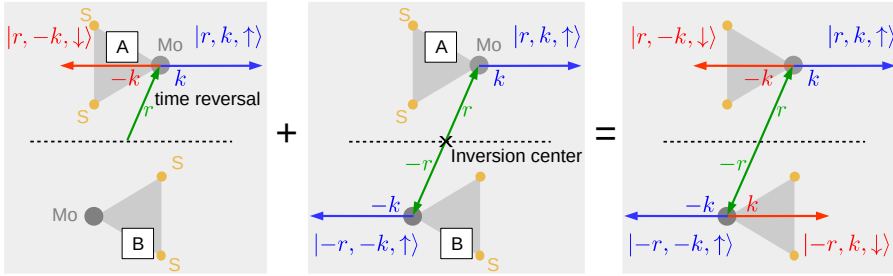


Figure 4.11: Illustration of Kramer's degeneracy applied to the MoS_2 case. Upon inversion the vector \mathbf{r} is reversed, mapping each atom from layer A onto its inversion partner in layer B and vice versa. Therefore the degenerate states of opposite spin can be located in different parts of the unit cell. Note that the localization in real space must be in a dimension perpendicular to \mathbf{k} . Otherwise there is no common set of space and momentum eigenfunctions $|\mathbf{r}, \mathbf{k}\rangle$, since the parallel components of $\hat{\mathbf{r}}$ and $\hat{\mathbf{k}}$ do not commute.

position vector \mathbf{r} along with \mathbf{k} . So if one imagines a wave function $|\mathbf{k}, \uparrow\rangle$ close to a molybdenum atom at the position \mathbf{r} in layer A of the MoS_2 unit cell, then the spatial part of the degenerate state according to time reversal symmetry $|\mathbf{-k}, \downarrow\rangle$ remains at the same atom. Inversion symmetry, however, does not demand a degenerate state $|\mathbf{-k}, \uparrow\rangle$ at the same atom, but at its *inversion partner* at $\mathbf{-r}$ in layer B. So the degenerate states $|\mathbf{k}, \uparrow\rangle$ and $|\mathbf{-k}, \downarrow\rangle$ can remain distinguishable by the spatial part of the wave function, without violating time or inversion symmetry. Based on this concept Zhang and Liu et al. [118] have recently derived a “hidden spin-polarization” by considering the specific site asymmetry of each inversion partner individually in the treatment of SOC.

In order to find this type of spin-polarization one notices that it is linked to a set of demands that have to be fulfilled. The crystal must have a multi-atomic basis in order to possess the needed site asymmetries. Also the SOC strength benefits from heavy elements in these sites. Furthermore, to access the spin-polarization, whether it is from a quantum mechanical or an experimental point of view, the electronic structure has to be measured at specific points in real and in reciprocal space. In terms of quantum mechanics the wave function must be localized mostly at one of the inversion partners, or the angular momentum of the state vanishes. Finding a distinct momentum eigenstate in reciprocal space, that is simultaneously localized in real space seems to oppose the uncertainty principle. However, only the

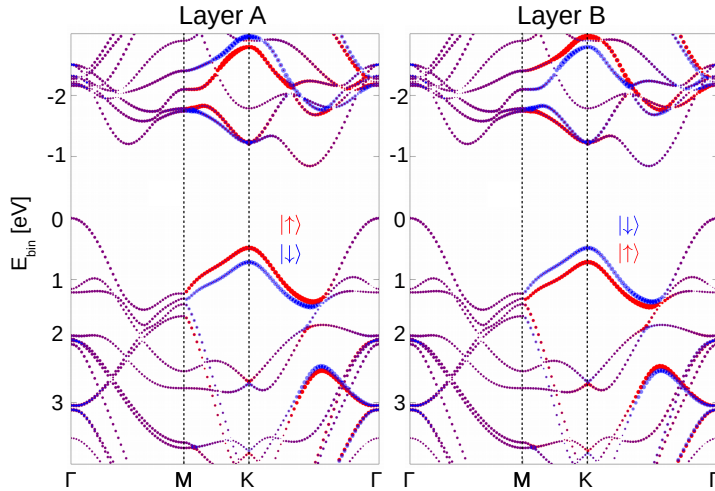


Figure 4.12: DFT calculation of the out-of-plane spin-polarization in the layers A and B in bulk MoS₂. The valleys at the \bar{K} show a high spin-polarization that reverses from one layer to the next, which leads to a vanishing average polarization for each state in the entire unit cell. The local polarization was obtained by projecting the bands into a sphere around the respective Mo atom in layer A and B, which is valid since the valleys at \bar{K} mostly localized at this atom.

parallel components of $\hat{\mathbf{r}}$ and $\hat{\mathbf{k}}$ do not commute. Therefore, one should search the electronic structure for momentum eigenstates $\hat{\mathbf{k}}$, which are localized, which means not dispersing, in a directions perpendicular to $\hat{\mathbf{k}}$.

The valleys at the \bar{K} point of the MoS₂ BZ fulfill these conditions: There are two inversion partners of the heavy element molybdenum in the unit cell. Each one is located in either the A type or B type of the monolayer orientation. In the previous section 4.2 it was shown that the valleys at the \bar{K} point disperse in the \mathbf{k}_{\parallel} direction, but not in \mathbf{k}_{\perp} . The missing \mathbf{k}_{\perp} dispersion allows for states to be localized in either the A or B type of layers. On the other hand the \mathbf{k}_{\parallel} dispersion points towards momentum eigenstates that are delocalized throughout the monolayers, and might therefore be dominated by the local site asymmetry of the molybdenum atom.

To investigate the hidden spin-polarization with DFT it is necessary to project the solution onto the A or B type layers. Figure 4.12 shows the out-of-plane component of the spin-polarization of the MoS₂ bulk bands in the two layers. And indeed the layer-resolved spin analysis reveals a non-vanishing spin-polarization

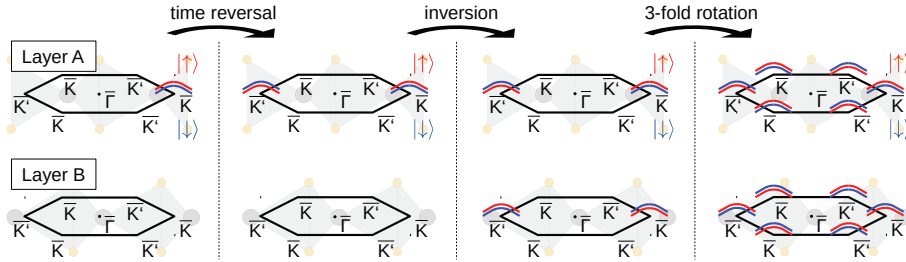


Figure 4.13: Qualitative illustration of the type of spin-texture that is consistent with the symmetry 2H-MoS₂. Assuming a spin-split valley pair at the \bar{K} point one can sequentially add degenerate valley pairs that have to exist due to basic symmetry considerations. This results in 12 degenerate pairs that remain distinguishable by either the spatial part of the wave function, which means their localization within layer A or B, or by the position within the BZ in reciprocal space.

that reverses from one layer to the next as expected. Therefore, the average spin-polarization of each state is zero when it is summed up over the entire unit cell.

To determine a complete representation of the valence band spin characteristics, the symmetry considerations described above have to be combined with the 3-fold rotational symmetry of the crystal, and it has to be applied to both of the valleys at the \bar{K} point. The result is a rather complicated spin texture which is illustrated in figure 4.13. At the \bar{K} point in layer A the states $|\uparrow\rangle$ and $|\downarrow\rangle$ are ≈ 180 meV split by the SOC, producing the valley pair that has been observed in ARPES and in DFT calculations. Time reversal duplicates the pair with reversed spin at the opposite side of the BZ at \bar{K}' . Following the inversion symmetry the entire band structure from layer A is duplicated with reversed spin in layer B, which is equivalent to a rotation of 180° equivalent to the layer orientation. Finally, the 3-fold rotational symmetry results in alternating spin orientation between neighboring \bar{K}/\bar{K}' points.

Spin-ARPES experiments

The spin-polarization in MoS₂ is hidden by its compensated nature in both real and reciprocal space, which is the reason why it has been overlooked for so long. Its experimental proof is therefore challenging. ARPES obviously provides the momentum resolution, and in section 4.2 the valleys at a selected \bar{K} point were already investigated without spin-resolution. The required real space resolution to selectively probe an A or B type layer can be achieved by the extreme surface sensitivity

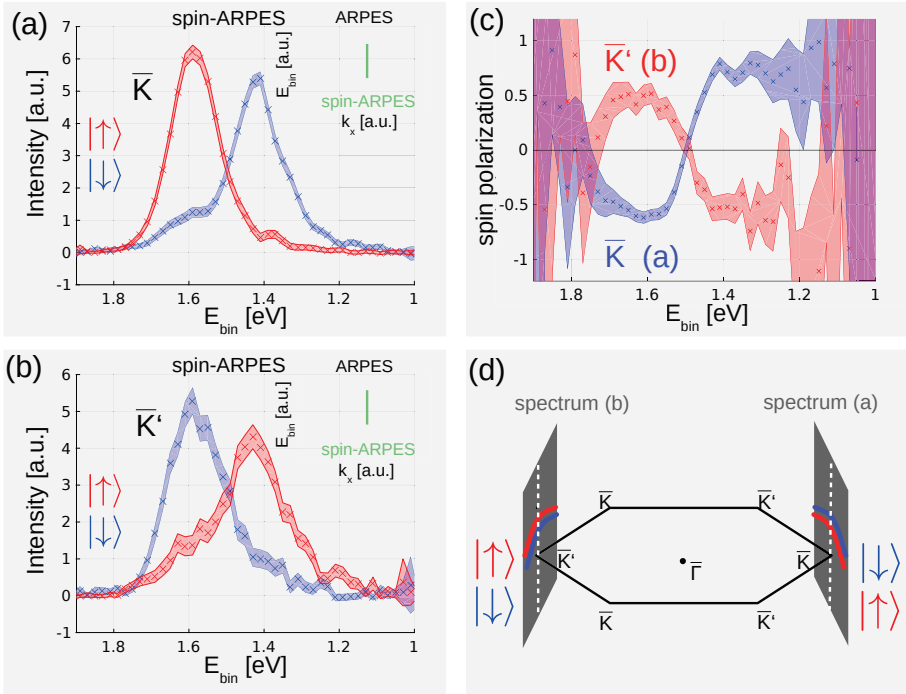


Figure 4.14: (a)/(b) Spin-ARPES spectra of the valence band splitting at the \bar{K}/\bar{K}' point. The red and blue curves show the partial intensities of $|\uparrow\rangle$ and $|\downarrow\rangle$ photoelectrons calculated from the raw spectra using the asymmetry function. (c) Spin-polarization at \bar{K} (spectrum a, blue) and at \bar{K}' (spectrum b, red). (d) Illustration of the position of the (spin-)ARPES spectra within the BZ. The envelope of the data points in (a)-(c) represents their statistical error.

of the technique. Assuming an IMFP of 4 \AA compared to a thickness of one monolayer of $\approx 6 \text{ \AA}$ it is obvious that the majority of the photoemission signal will stem from the topmost monolayer.

In order to utilize the surface sensitivity, however, a purely A or B terminated sample surface is required. In section 4.1 it was already shown by the AFM images that macroscopic terraces with a single termination can be produced by cleaving. Although the LEED measurements suggest a diameter of the terraces in the order of several millimeters it is desirable to minimize the size of the beamspot on the sample. The spin-ARPES experiments were performed at the ARPES beamline of

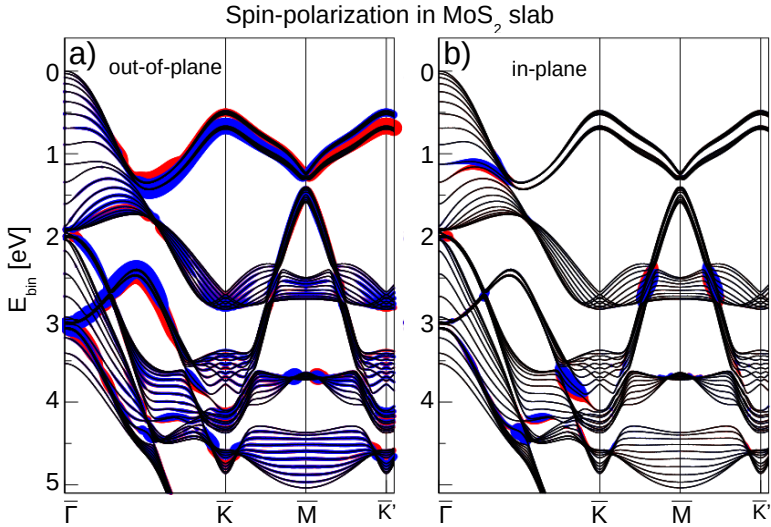


Figure 4.15: 10-layer slab calculation of the MoS₂ band structure including the spin component in out-of-plane (a) and the in-plane (b) direction in the first monolayer. The surface localized states (see section 4.2.3) show an in-plane and an out-of-plane component of the spin-polarization, which is tied to the first monolayer. The valleys at the \bar{K}/\bar{K}' have a polarization $> 99\%$ in the out-of-plane direction.

DELTA. The refocusing of the exit slit in the vertical direction produces a rather low height of the beamspot of $\approx 300 \mu\text{m}$. In the horizontal direction the lack of refocusing optics results in a native beamspot width $> 3 \text{ mm}$. The width can only be reduced by apertures. This not ideal for experiments with the SPLEED detector, which has a figure of merit of $\approx 10^{-3}$. As a compromise the intensity was reduced by $\approx 80\%$ leading to a horizontal beam spot size of $\approx 800 \mu\text{m}$ on the sample, which was determined by the spatial lens mode of the spectrometer. A photon energy of 27 eV was chosen to achieve a high photon flux in combination with high surface sensitivity. The spin-ARPES measurements were performed at $+36^\circ$ and -36° off normal emission, which corresponds to the \bar{K} and \bar{K}' point respectively. The flat surface area that was earlier observed with LEED was identified in the spatial lens mode.

Figures 4.14 (a)/(b) show the spin-ARPES spectra of the valence band splitting at \bar{K} and \bar{K}' and reveal that it is indeed highly spin-polarized. Also, the sign of the polarization reverses from \bar{K} to \bar{K}' , as it was expected considering the time reversal

symmetry. Figure 4.14 (c) shows the degree of polarization spin-ARPES spectra, which is $\approx 65\%$ at \bar{K} and $\approx 50\%$ at \bar{K}' . The reduced polarization at \bar{K}' is most likely a result of the slightly different position of the beamspot on the sample, since it had to be rotated in order to reach the opposite side of the BZ. Prior to each spin-ARPES measurement conventional ARPES spectra were taken, which are shown in the top right corners of figures 4.14 (a)/(b). Both spectra show a low overall noise ratio and the splitting is clearly visible, which is a good indication for a clean and flat surface. However, in the spectrum at the \bar{K} point the splitting is slightly more pronounced especially in the side regions of the conventional ARPES data. This also supports the interpretation that the reduced polarization at \bar{K}' is an artifact caused by the different beamspot position. If the illuminated area contains a lower portion of the single terrace region one can expect the spectrum to smear out and an overall increase of the noise due to the presence of steps and partially cleaved off material. Furthermore, it increases a chance of illuminating surface areas of the opposite termination. Both effects reduce the observed spin-polarization.

Also for the spin-ARPES experiments it has to be shown that the conclusions are not drawn based on the wrong crystal phase 3R-MoS₂. As it was already discussed 3R-MoS₂ is not centrosymmetric and the observation of spin-polarized bands would not be surprising. Apart from the convincing arguments that support the assumption of the used samples being purely composed of the centrosymmetric 2H-MoS₂ crystal phase, the spin-ARPES itself contains proof of it. The splitting that was observed in the spin-ARPES data and the conventional ARPES spectra that were taken beforehand again show the 180 eV splitting of the valleys, which corresponds to 2H-MoS₂ instead of 140 eV in the case of 3R-MoS₂ [120]. Therefore, the non-centrosymmetric 3R-MoS₂ can be ruled out as the origin of the observed spin-polarization.

The initial band polarization

The spin-polarization that is observed in the photoemission experiment is not necessarily the same as in the initial band. In general the photoelectron polarization is modulated by the polarization of the final state as well as by the transition itself. For the MoS₂ sample especially the probing depth and the surface topography have a major impact on the measured polarization.

Regarding the probing depth of the spin-ARPES experiment there are two es-

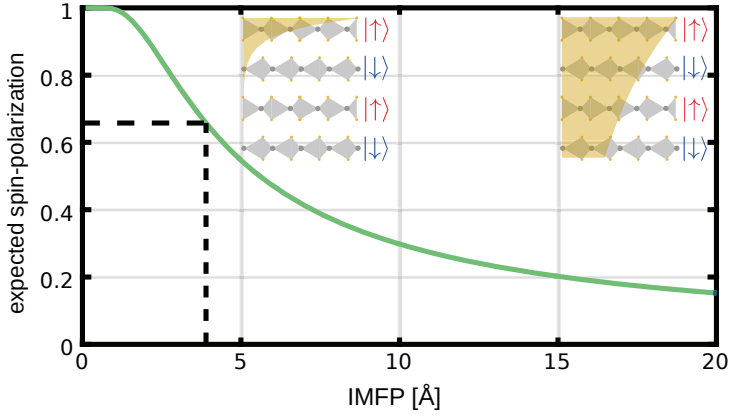


Figure 4.16: Expected polarization in spin-ARPES as a function of the IMFP assuming fully spin-polarized bands in each monolayer. The higher the probing depth the more alternating spin orientations contribute to the photoemission signal. The polarization of $\approx 65\%$, which was observed in the experiment, is marked with a dashed line and corresponds to an IMFP of $\approx 4 \text{ \AA}$.

sential aspects. The first aspect is that this study tries to draw conclusions about bulk properties of MoS₂. Therefore, it should be discussed to what extent the spin-polarization could be influenced by surface specific properties. In section 4.2 it was shown that the valleys the \bar{K}/\bar{K}' point are localized within the monolayers. ARPES and DFT both showed no indication that these states are significantly influenced by the surface. Figure 4.15 shows a 10-layer slab calculation indicating the spin-selective charge localized within the first monolayer. The out-of-plane component of the spin is in good overall agreement with the bulk calculation that was shown in figure 4.12, except for the surface states, which were discussed in section 4.2 and are not present in the bulk. Since the surface localized states are a result of the symmetry breaking in the out-of-plane direction they show a high degree of in-plane polarization, which is not the case for any of the bulk states. Riley et al. [120] observed an in-plane spin-polarization in WSe₂, which is very similar to MoS₂, and attributed it to the same mechanism. The spin-polarization of the valleys was calculated for individual layers in the slab and showed a value of more than 99% regardless of the position within the slab. Therefore, one can safely assume that the high degree of polarization that was observed in spin-ARPES is a result of the hidden spin-polarization of the bulk crystal.

The second important aspect regarding the probing depth is that the spin-polarization alternates from layer A to layer B, which means that the experimentally observed polarization is partially canceled out by a probing depth higher than one monolayer. Figure 4.16 shows a model calculation of the expected polarization in spin-ARPES as a function of the IMFP. The model assumes fully spin-polarized initial bands, as the DFT calculations suggest. The typical absorption law (see equation 2.21) of the IMFP is used to estimate the contribution of each layer to the photoemission signal and therefore to the $|\uparrow\rangle$ and the $|\downarrow\rangle$ channel in the experiment. One can see that the polarization of $\approx 65\%$, that was observed in the spin-ARPES experiment, is the expected value at an IMFP of $\approx 4 \text{ \AA}$, which is a realistic value according to the universal curve (see figure 2.8). The observation of 65% polarization agrees with the calculated value. Considering all uncertainties, especially the unknown probing depth, the SPLEED data cannot give an exact value for the initial spin-polarization.

We are only aware of one publication on the spin-polarization in MoS₂ bulk samples. Suzuki and Sakano et al. [31] investigated synthetic 2H-MoS₂ and 3R-MoS₂ crystals with spin-ARPES experiments. At first sight their results seem to contradict the results of this study. While Suzuki and Sakano et al. observed fully spin-polarized valleys in the 3R-phase they did not observe any polarization in the 2H-crystal. However, they provide optical micrograph images of their samples, which reveal a high density of steps and dislocations in their samples. Therefore, the experiment of Suzuki and Sakano et al. was only sensitive to the net-polarization averaged over all possible terminations, which means nearly 100% for 3R-MoS₂² and 0% 2H-MoS₂. The results shown here are in better agreement with a similar study on WSe₂ by Riley et al. [120], which also finds a high degree of polarization. Riley et al. also show the observed spin-polarization as a function of the photon energy and find a quite strong dependence. They provide a model calculation that derives the change of the polarization in spin-ARPES purely as a result of photoelectron diffraction from the first two monolayers. However, also the changing probing depth and the spin-character of the final state of the photoemission process certainly have a strong influence on the actually observed polarization depending on the photon energy. Therefore a thorough, quantitative analysis of the spin-polarized photoemission process is quite challenging.

Especially the uncertainty regarding the probing depth does not allow us to

²This assumes a single domain orientation of the crystal.

conclude an exact number for the polarization of the initial bands from the spin-ARPES data. However, observing 65% polarization and the reversal between the \bar{K} and \bar{K}' point makes it unlikely that the observation is dominated by pure photoemission effects. Furthermore, one should also keep in mind that the non-zero probing depth and a possible contribution of adjacent terraces of the opposite layer orientation can only reduce the observed polarization compared to the initial state, not artificially increase it. Therefore, the experimental results give a strong support for our interpretation that there are highly spin-polarized states in 2H-MoS₂.

Spin-layer locking

So far we have shown that the out-of-plane dispersion is of key importance in the context of the hidden spin-polarization in 2H-MoS₂. To our knowledge there are no publications that show experimental observations of the out-of-plane dispersion of the valleys at the \bar{K} point for MoS₂, however, other groups found a similar two-dimensional confinement in WSe₂ [120] and WS₂ [131]. The band structure calculations that are shown here are in a good overall agreement with earlier publications [130, 132–134]. Some groups, however, reported a much larger out-of-plane dispersion of the valleys at \bar{K} [116, 135] and even degenerate bands at the H point, which would indicate full three-dimensional delocalization of the states. This de-

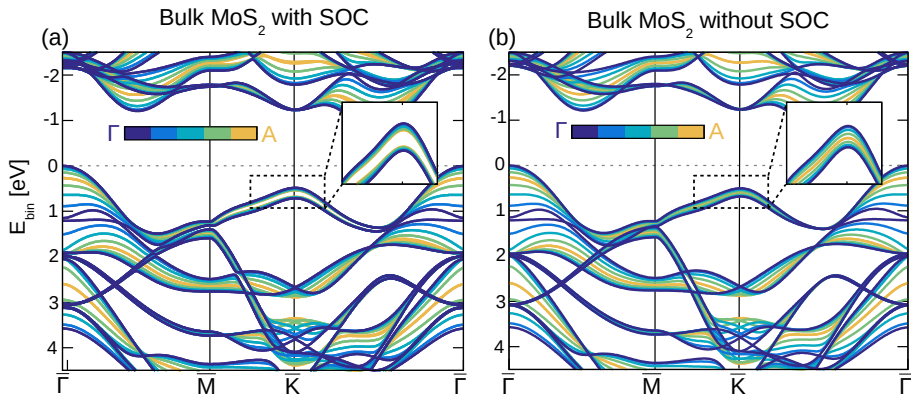


Figure 4.17: Bulk band structure of 2H-MoS₂ with (a) and without (b) SOC included projected into the surface BZ. The bands are color coded for the out-of-plane dispersion. The only apparent difference between the band structures in (a) and (b) is the out-of-plane dispersion of the valleys at the \bar{K} point.

viation from the findings that are presented in this chapter can be reproduced by omitting the SOC from the calculations. Figure 4.17 shows a comparison of the bulk projected band structure of 2H-MoS₂ with and without SOC. The two band structures are almost completely the same with the exception of the valleys at the \bar{K} point.

This observation together with the previous discussion of the hidden spin-polarization allows for an interesting interpretation: the SOC is responsible for the two-dimensional confinement of the states. Riley et al. [120] discussed the same mechanism in WSe₂ and referred to it as *spin-layer locking*. The SOC lifts the spin-degeneracy of the valleys, and the spin orientation alternates with the layer orientation. Therefore the state $|E_n, \mathbf{k}, \uparrow\rangle$ of an electron in layer A is not a solution in layer B, but $|E_n, \mathbf{k}, \downarrow\rangle$ is. This *locks* the electron to one of the two possible layer orientations depending on its spin. The spin part of the wave function makes the two states orthogonal and they cannot give rise to an out-of-plane delocalization. The next possible location for the same state to exist is a distance of two monolayers, which again results in too little spatial overlap for a significant delocalization.

Conclusions

This chapter showed that the basic symmetry considerations allow for a compensated spin-polarization in bulk crystals such as MoS₂ despite their centrosymmetric space group. By observing a vanishing out-of-plane dispersion of distinct valleys in the MoS₂ band structure in ARPES, it was demonstrated that these states are almost completely confined within two dimensions. These results were confirmed theoretically by DFT calculations, which are in exceptional agreement with the experimental observations. For the valleys a spin-polarization of $\approx 65\%$ has been observed directly in spin-ARPES. However, since several parameters of the photoemission process, in particular the exact escape depth of the photoelectrons, can only be estimated, it is not possible to derive an exact number for the polarization of the initial bands from the experiment alone. It only allows to conclude that it is at least the observed 65%, but possibly higher, since several effects such as the non-zero probing depth reduce the directly observed polarization compared to the one of the initial bands. The DFT calculations show a spin-polarization of the valleys of $> 99\%$, a simple model calculation it was shown that full spin-polarization in initial bands agrees well with the observation of 65% in spin-ARPES assuming the realistic value of 4 \AA for the IMFP of the photoelectrons.

Using a combination of (spin-)ARPES and DFT we have demonstrated that, against common belief, 2H-MoS₂ possesses a high degree spin-polarization. These results are not only of importance for this fascinating, and technologically relevant material, they also proof the existence of this recently introduced type of *hidden spin-polarization*.

The electronic structure of ReS₂

Compared to the most famous members of the transition metal dichalcogenide (TMDC) family, MoS₂ and the very similar MoSe₂, WS₂, WSe₂, rhenium disulphide (ReS₂) is a rather unknown material. Due several properties that set ReS₂ aside from classical TMDCs, a growing number of researchers move their attention towards it. Like MoS₂, ReS₂ is a semiconductor both in bulk and in its atomically thin form. However, the additional valence electron of rhenium compared to molybdenum leads to a drastic, uniaxial deformation of the ReS₂ lattice structure compared to the honeycomb lattice of classical TMDCs. This results in a highly anisotropic behavior of ReS₂ and the very similar ReSe₂, which make them a promising addition to the more established building blocks of novel van der Waals structures. The anisotropic character of the material has already been demonstrated by transport [39,136], optical absorption [137], photoluminescence [138], and Raman spectroscopy [139,140] measurements. A direct investigation of the electronic band structure, which underlies these effects, has been missing until now. This chapter will show a detailed study of the electronic structure of bulk, monolayer, and bilayer the ReS₂ by angle-resolved photoemission spectroscopy (ARPES) in combination with density functional theory (DFT) calculations. The focus will lay on two main issues: the three-dimensional delocalization of the bulk valence electrons, and the position of the valence band maximum in bulk, monolayer and bilayer ReS₂.

All DFT calculations that are presented in this chapter were performed at PGI-1 by Gustav Bihlmayer using the *FLEUR* software package [52]. A GGA exchange-correlation potential was used, and the lattice parameters were fixed at experimental literature values from Lamfers et al. [141].

3D band mapping ReS₂ bulk single crystals

ReS₂ is a van der Waals (vdW) material consisting of atomic S-Re-S trilayers forming the covalently bound monolayers of the material. Therefore, ReS₂ largely shares the properties of more well-known TMDCs such as MoS₂ and WS₂ in terms of cleavage

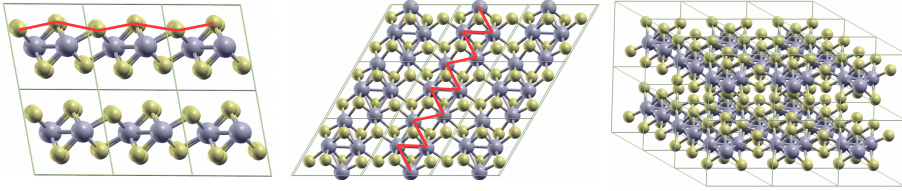


Figure 5.1: Crystal structure of ReS_2 from different perspectives. The red lines illustrate the reconfiguration of the crystal structure compared to classical TMDCs by the additional electron of Re. The apparent uniaxial symmetry is the origin of the highly anisotropic properties of the material.

and exfoliation behavior. However, the one additional electron of Re compared to W provides an additional covalent bond. This additional bond results in buckling of the crystal structure, forming uniaxial chains within the monolayers. Figure 5.1 depicts the crystal structure of ReS_2 . The buckling of the crystal not only roughly doubles the unit cell dimensions within the plane, but also reduces the crystal symmetry. This reconfiguration of the crystal structure is the origin of the highly anisotropic properties of ReS_2 .

ARPES experiments and DFT calculations

Unlike MoS_2 , which was discussed in the previous chapter, ReS_2 crystals are extremely rare in mineral form. However, large synthetic single crystals of ReS_2 have been commercially available for several years now. All bulk samples that are discussed in this chapter were bought from *hq graphene, Netherlands*. For the photoemission experiments the sample was cleaved using adhesive tape immediately before introducing it into ultra-high vacuum (UHV), and then degassed at 250°C in vacuum. The cleavage process produced shiny, flat surface areas, that were in most cases less than 0.5 mm in diameter, and separated visibly by sharp edges.

All photoemission experiments on the ReS_2 bulk samples were performed at the NanoESCA end-station of Peter Grünberg Institut 6 (PGI-6) at ELETTRA, Trieste. Although the lab-based photoemission setup in Jülich provides higher resolution, due to its macroscopic beamspot it is not feasible for the ReS_2 samples. The real space imaging capabilities of the NanoESCA and the microscopic control of the beam position makes it possible to identify and measure flat, homogeneous areas on the sample. Also, a *k-space microscope* maps the reciprocal space without rotating the

sample as in conventional ARPES setups, and therefore the same area is probed throughout the entire experiment. Furthermore, unlike the lab based light sources the beamline provides photons of a tunable energy, which is mandatory for detailed three-dimensional k-space mapping.

Disadvantages of the NanoESCA setup regarding the ReS₂ samples, apart from the lower energy resolution, are the high extractor voltage and charging effects due to the microscopic beamspot. The high voltage of several keV between the sample and the microscope lead to field emission from the sample. Since the cleavage process is likely to produce areas with partially cleaved-off layers, these layers can form sharp edges sticking out from the sample surface. The real space imaging capabilities of the NanoESCA make it quite easy to identify these areas, so they can be avoided for the measurements. However, the high electric fields at sharp edges lead to a considerable, unstable field emission current, which for some surfaces made it impossible to set up the NanoESCA for the experiment. The cleavage process had to be repeated numerous times until a suitable sample surface was obtained. Furthermore, the well focused beamspot with a diameter of $\approx 15 \mu\text{m}$ results in an extremely high photon flux density in the illuminated area. As a result charging effects of the semiconducting ReS₂ samples were observed in the form of slight kinetic energy shifts of the spectra.

Figure 5.2 shows selected binding energies from the ARPES data taken at a photon energy of 88 eV. The experimentally observed momentum range is $\approx \pm 2 \text{ \AA}^{-1}$, and therefore covers the length of more than three surface BZs of ReS₂. In figure 5.2 the surface BZs are marked in red. Comparing the data for one binding energy between different surface BZs one can definitely find similarities. However, it is obvious that the data is not genuinely periodic with the BZs. The data from different BZs not only corresponds to different escape directions of the photoelectrons with respect to the surface, but also to different initial state and final state orientation with respect to the light direction and polarization. Therefore, the photoemission process itself intrinsically breaks the symmetry, which leads to intensity modulations throughout the image. The deviation from the surface BZ's periodicity, however, is so drastic that it can be hardly explained by intensity modulations alone. Instead one can observe numerous examples of sharp bands that clearly change their position from one surface BZ to the next, which is an indication for a non-vanishing out-of-plane dispersion. This observation stands in contrast to a report by Tongay et al. [142], who claimed that they found a complete electronic decoupling of the monolayers in

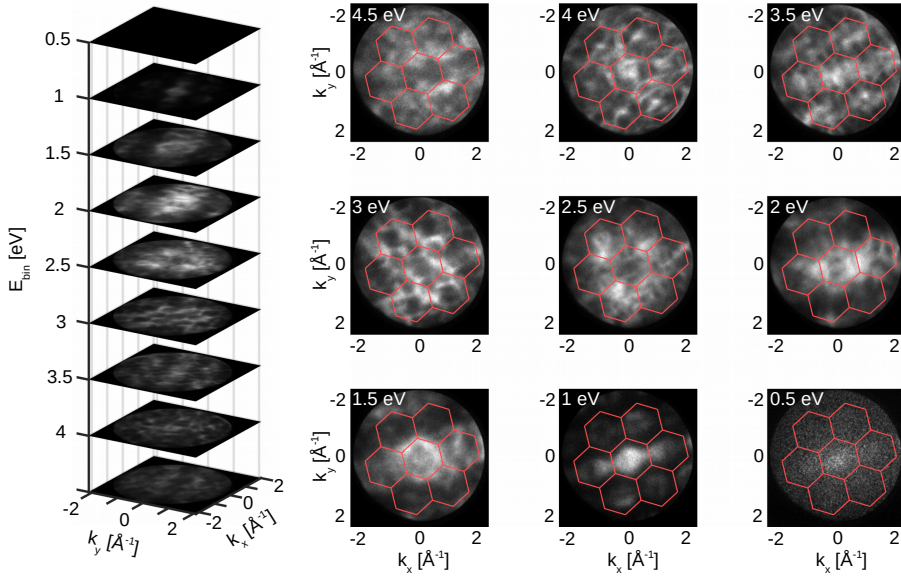


Figure 5.2: ARPES data of the ReS_2 bulk crystal at selected kinetic energies taken with $h\nu = 88$ eV. The field of view in momentum mode spans $\approx \pm 2$, which covers more than three ReS_2 surface BZs. The surface BZs edges are marked in red. Although the different BZs share similarities, no strict periodicity is observed, which is an indication of the out-plane-dispersion of the material.

ReS_2 . Their conclusions are based on band structure calculations and on Raman spectroscopy experiments, where they find no indication of out-of-plane vibrational modes. A strong out-of-plane dispersion would prove otherwise, since it corresponds to a delocalization of the valence electrons across the vdW gap.

According to the free-electron final-state (FEFS) model the perpendicular momentum component \mathbf{k}_\perp of the probed initial state is maximum at normal emission, and it decreases with a larger parallel momentum component $\mathbf{k}_\parallel = \mathbf{k}_x + \mathbf{k}_y$. The varying \mathbf{k}_\perp within the spectrum contributes to the irregular dispersion in figure 5.2. However, this effect is rotationally-symmetric around normal emission, which is also not apparent in the ARPES data. The irregular dispersion that is observed in the ARPES data can be explained by the complicated shape and arrangement of the bulk BZs that results from the triclinic crystal lattice. Figure 5.3 illustrates the three-dimensional arrangement of the bulk BZs.

Since two real space lattice vectors lie within the monolayers, one of the reciprocal

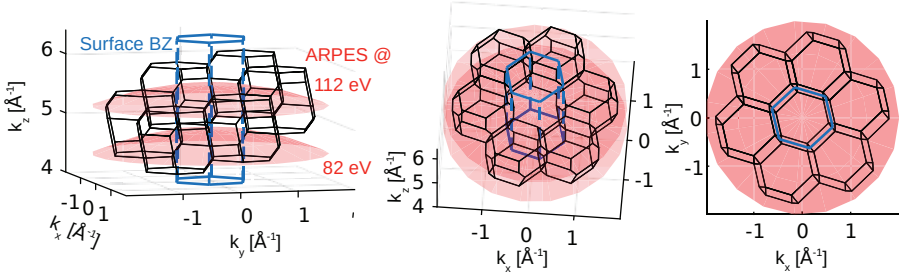


Figure 5.3: Illustration of the bulk BZ arrangement from different perspectives. Since the two reciprocal lattice vectors are not parallel to the surface, a plane with constant k_z crosses a different part of every adjacent BZ. In addition red, curved planes show the \mathbf{k}_\perp selection in ARPES according to the FEFS model for two selected values of E_{kin} .

lattice vectors is perpendicular to the monolayer plane, and therefore also to the surface. The other two reciprocal lattice vectors, however, have mixed in-plane and out-of-plane components. This means that adjacent BZs are displaced in the out-of-plane direction and a plane with constant k_z cuts through a different part of every BZ, as it is shown in figure 5.3.

Due to the reciprocal lattice vector perpendicular to the sample surface, at least in the out-of-plane direction the BZs align, so there is a meaningful bulk projection along this lattice vector onto the surface BZ. Figure 5.4 shows the bulk projection for a selected path in reciprocal space. The path along the high symmetry points Γ -M-K-M'- Γ has been sequentially displaced in the out-of-plane direction by a full reciprocal lattice vector, and is projected onto the surface BZ for every displacement. Since there is no horizontal displacement of the second BZ, the plotted k_z range represents a full period of the bulk band structure, and any further displacement will lead to equivalent states.

In this calculation one can find a considerable out of plane dispersion and a direct band gap at the A point. This stands in contrast to the report by Tongay et al. [142], which does not show the out-of-plane dispersion but claims that the bulk band structure is equivalent to that of freestanding monolayers. Tongay et al. report a direct band gap at the $\Gamma/\bar{\Gamma}$ point. However, their also presented photoluminescence data suggest an increase of the band gap when the material is thinned down to

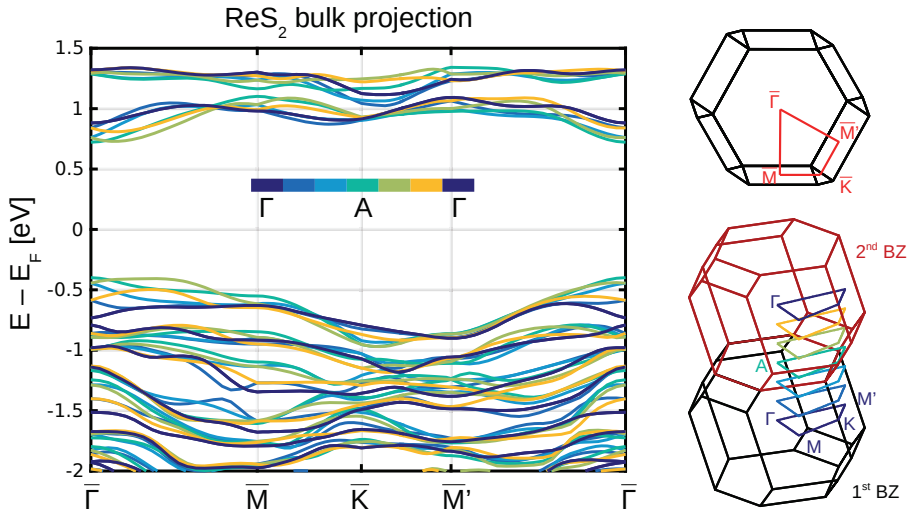


Figure 5.4: DFT calculation of the ReS_2 bulk band structure projected onto the surface BZ. The color code represents the out-of-plane displacement of the path. The position of the differently displaced paths within the 3D BZ is illustrated on the right. A direct band gap is found at the A point.

a single monolayer. A recent report by Qiao et al. [143] shows a similar behavior in photoluminescence, and finds contrary to Tongay et al. a significant interlayer interaction in bulk ReS_2 .

When ReS_2 is thinned down to a few layers, the out-of-plane dispersion is quenched by the forced quantum confinement of the electronic states. In the monolayer limit, the electronic structure becomes fully two dimensional. This means that the Γ and the A point become equivalent in the $\bar{\Gamma}$ point of the surface BZ. The dispersion along Γ -A has to disappear, and therefore it is hard to imagine that the bulk band gap at the A point remains unaffected by the quantum confinement. This interpretation compares well to the thickness dependent optical behavior that was reported by Tongay et al. [142] and Qiao et al. [143]. To investigate the dispersion of the full ReS_2 bulk band structure, it is necessary to measure ARPES spectra at different photon energies. As it is shown in 5.3, this shifts the probed k_{\perp} in k-space so that the entire bulk BZ can be mapped. Since ARPES only probes the occupied valence band states, the valence band maximum can be identified experimentally, but the conduction band minimum cannot. To demonstrate the existence of a direct

band gap at the A point, this study has to rely on the comparison of ARPES data to the DFT calculations. A good agreement of the valence band structure is a strong support for the validity of the calculated band structure.

The main issue of a direct comparison of the ARPES data to DFT is to reliably determine the \mathbf{k}_\perp component of the initial state. Although the FEFS model provides the means to calculate \mathbf{k}_\perp it always depends on the inner potential V_0 , which has to be determined empirically. V_0 influences the offset and the exact curvature of the slice of the three-dimensional k-space that is probed by a certain kinetic energy. Additionally, the sample was charging under the synchrotron light. The resulting binding energy offset changed for spectra measured at different photon energies. Therefore, the compensation of this offset enters the analysis as an additional, empirical parameter. This in combination with the complicated stacking of the BZs makes it difficult to directly to identify high symmetry directions from the DFT calculations within the ARPES data without prior knowledge of the empirical parameters.

Applying the FEFS model

Calculating the energy eigenvalues for a large number of points in reciprocal space is rather time consuming, and the exact coordinates in k -space were not clear before the inner potential and the kinetic energy offsets were determined. Therefore, the energy eigenvalues for a $61 \times 61 \times 61$ point mesh of k -coordinates were calculated by Gustav Bihlmayer (PGI-1) to cover the full primitive unit cell in reciprocal space. The eigenvalues of an arbitrary path in k -space could then be quickly calculated by folding it back into the first unit cell and interpolating within the precalculated mesh for each band. The interpolation method in combination with the FEFS model, made it possible to determine the inner potential and the kinetic energy offsets by optimizing the agreement of the calculated bands with the ARPES data.

Figure 5.5 shows a comparison of the ARPES data, taken with a photon energy of $h\nu = 88$ eV, with the FEFS calculations. Since the DFT calculations give discrete energy eigenvalues, the theoretical band structure is infinitely sharp. To simulate the

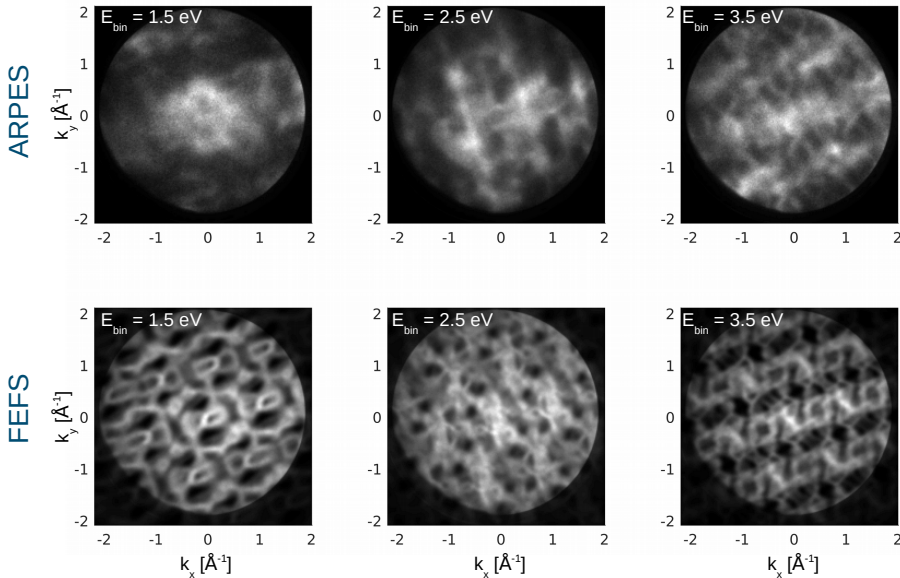


Figure 5.5: Comparison of ARPES data taken at $h\nu = 88$ eV to FEFS calculation. Gaussian broadening was applied to the FEFS calculation to simulate the experimental energy and momentum resolution.

experimental resolution, which is dominated by the energy resolution of the analyzer, the calculated bands are convoluted with a Gaussian distribution with $\Delta E = 0.1$ eV. The FEFS calculation shows a good agreement with the experimental data except for additional intensity modulations due to photoemission effects, which are not included in the FEFS model.

The scripts for the FEFS calculations were written for the software package *Matlab* [144]. To accurately determine the k_{\perp} selection for a certain point within the spectrum resembles a classical chicken-and-egg problem. As it was introduced in chapter 2.4.2 the k_{\perp} selection according to the FEFS model is a function of the kinetic energy E_{kin} . However, E_{kin} of the photoelectrons is a function of the binding energy, which is a function of the band dispersion in return. The band dispersion is only available in form of the discrete, precalculated mesh of eigenvalues, and the identification of the crossing point of the free-electron parabola with the bands has to be performed for each \mathbf{k}_{\parallel} individually.

To obtain an accurate FEFS result within a reasonable run-time of the Matlab scripts, first the intersection of the free electron parabola with the average binding energy of each band is solved analytically. This way an approximated value for k_{\perp} is obtained. Then the value is refined by sampling the band dispersion in the region of the approximated k_{\perp} via interpolation within the precalculated mesh of eigenvalues. In figure 5.6 three directions of k_{\parallel} , which resemble vertical cuts through the previously shown k_x vs. k_y data, are compared to the FEFS calculations. The results of the FEFS calculations that are shown in figure 5.6 reproduce the experimental data quite well.

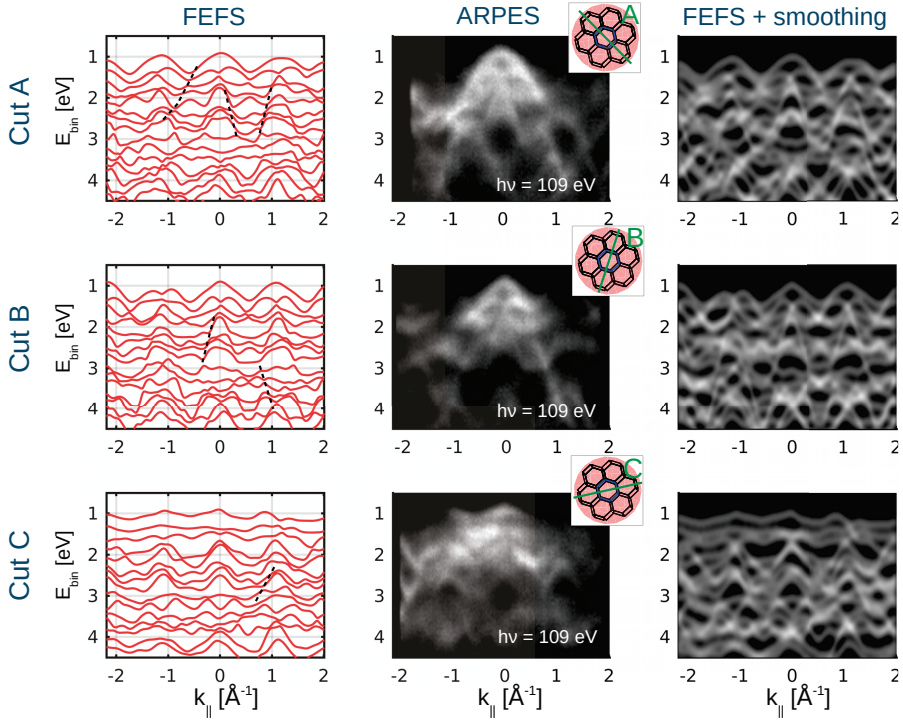


Figure 5.6: Comparison of ARPES data to FEFS calculations. The center column represent three different vertical cuts through the previously shown data. The direction is indicated in the top right corner of each spectrum. The left column shows the bands calculated according to the FEFS model. Several bands in the ARPES data appear steep compared to rather flat bands in the FEFS calculation. This is an artifact of the finite energy resolution and can be reproduced by smoothing the FEFS bands accordingly, which is shown in the right column in good agreement to the ARPES data.

Identification of the valence band maximum

In order to track the valence band dispersion in the out-of-plane direction from the Γ point to the A point, where the DFT calculations predicted the valence band maximum, the ARPES measurements were performed at photon energies from 82 eV to 112 eV in 3 eV steps. In figure 5.7 this is shown for one selected k_{\parallel} direction plotted against the binding energy. The bands in the ARPES spectra appear rather broad. This can be partially explained by the energy resolution of ≈ 100 meV, but a further mechanism that has to be taken into account is the limited sharpness of the k_{\perp} selection due to the low probing depth of the technique. According to the *universal curve*, the inelastic mean free path (IMFP) for the used photon energy range should be in the region of 2 - 3 Å. Using Heisenberg's uncertainty principle one can estimate

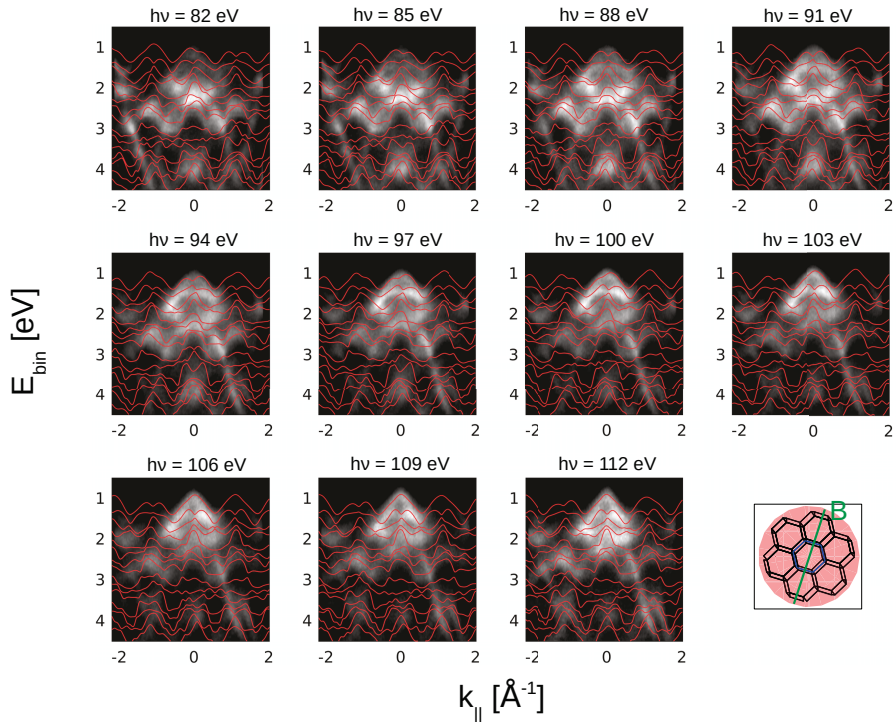


Figure 5.7: ARPES data obtained with different photon energies overlaid with the according FEFS calculations.

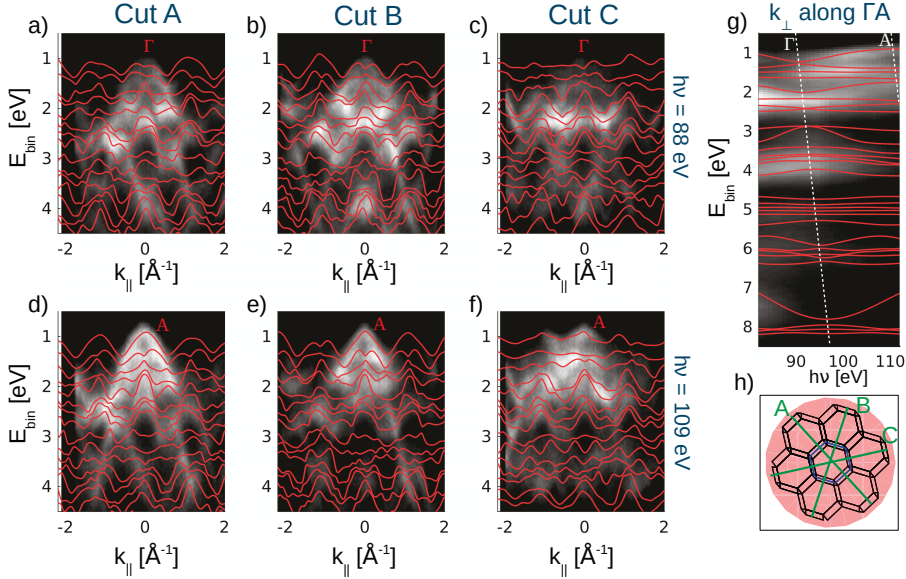


Figure 5.8: a-c) ARPES data in three k_{\parallel} directions taken at $h\nu = 88$ eV, where the topmost valence band cuts the 3D BZ through the Γ point for $k_{\parallel} = 0$. d-f) The same three k_{\parallel} directions taken at $h\nu = 109$ eV, where the topmost valence band cuts through the A point. g) ARPES data in the ΓA direction recalculated from all spectra with $h\nu = 88$ -112 eV. The dashed lines indicate the A and the Γ -point. h) Indication of the direction of cuts A, B, and C within the complete dataset (red circle) and the BZs.

that the sharpness of the k_{\perp} selection is in the order of $0.3 - 0.5 \text{ \AA}^{-1}$, compared to the height of the BZ in the surface normal direction of 1.03 \AA^{-1} . As it was already discussed the universal curve is only an approximation, but it is very likely that the low probing depth contributes to the energetic broadening of the ARPES data. Nevertheless, a clear change in the shape of the valence band can be observed in the ARPES data as the photon energy increases. Although the effect is superimposed with a shift of the spectral weight due to photoemission effects, the changes of the band shapes and the remarkable agreement with the FEFS calculations make it quite clear that the data represents an observation of the out-of-plane dispersion.

Figures 5.8 a-f) show k_{\parallel} vs. E_{bin} maps for three different directions within the BZ (see fig. 5.8 (h)) taken at the photon energies of 88 eV and 109 eV. The experimental data is again superimposed by the FEFS calculations. At 88 eV the topmost valence band at $k_{\parallel} = 0$ cuts through the Γ point of the three-dimensional

BZ. The dispersion of this band appears rather flat. Opposite to this, in the spectrum taken at a photon energy of 109 eV one can observe a pronounced maximum in the valence band dispersion. In this spectrum the topmost band is probed at the A point, where the global valence band maximum was found in the DFT calculations. In figure 5.8 g) the ARPES data from the entire used photon energy range is combined to show the out-of-plane dispersion in the ΓA direction. One can see that both in the experiment and in the theory the topmost valence band has its local minimum at the Γ point, while the valence band maximum is found at the A point. The dispersion in the ΓA direction appears slightly stronger in the FEFS calculation than in the ARPES data, but it is not entirely clear if this represents a discrepancy between the DFT calculations and the experimentally observed band structure, since it could as well be explained by the broad k_{\perp} selection, which is not exactly known. In conclusion, our three-dimensional band mapping in combination with band structure calculations provide strong evidence of a sizable out-of-plane band dispersion, which results from a considerable overlap of the electronic states across the vdW gap.

Atomically thin ReS_2

This section will show the results of photoemission experiments carried out on exfoliated, atomically thin ReS_2 samples. It will focus on the valence band maximum, which is largely responsible for the optical and electric transport properties of the material.

Sample properties

The atomically thin ReS_2 sample was produced by Philipp Nagler at AG Schüller, University Regensburg. In this group, mechanical exfoliation techniques are employed to produce few and single layer samples from layered crystals. The first step in the sample preparation process is the exfoliation of ReS_2 flakes from bulk crystal, such as the ones that were studied in the previous section, with adhesive tape. This step produces flakes of varying shape, size, and thickness. Under an optical microscope flakes with the desired properties can then be identified and transferred onto a viscoelastic, transparent polydimethylsiloxan (PDMS) stamp. A detailed description of the exfoliation and transfer procedures can be found in ref. [80]. The number of layers can be determined from the color of the flake alone. Figure 5.9 a) shows the ReS_2 sample on the PDMS stamp. Different shades allow to identify monolayer and bilayer areas that are more than $5\ \mu\text{m}$ wide, which makes them large enough for k-space-microscopy experiments.

In earlier attempts within this study the atomically thin samples were placed directly on doped Si substrates with native SiO_2 . The large band gap of SiO_2 makes it suitable to study quasi-freestanding vdW materials. However, these measurements suffered from an extremely poor quality of the spectra and it was not possible to observe clear, dispersive features in the photoemission data. The two main reasons for this are most likely the roughness of the substrate, and that it was covered by several atomic layers of adsorbates.

Unlike the previously discussed bulk samples, which could be cleaved immediately before the experiment to produce clean, flat surfaces, the exfoliation is performed ex situ. In order to clean the monolayer samples in UHV multiple approaches were tried: annealing, exposure to oxygen and hydrogen, and sputtering with low energy argon ions. However, these preparation steps could not produce surfaces clean and uniformly enough to show a clear band dispersion. As an alternative

approach, the samples were placed on highly oriented pyrolytic graphite (HOPG) flakes that were exfoliated and placed on the Si/SiO₂ substrates beforehand. Since HOPG is a vdW material itself it is a more promising candidate, as compared to SiO₂ to produce a clean surface purely through degassing at moderate temperatures in UHV. Furthermore, SiO₂ has a rough surface topography, which is likely to result in a buckling of ReS₂ monolayers when placed directly on it. Since ARPES relies on a uniform surface normal direction, this further reduces the quality of the spectra. A thick HOPG buffer layer can be expected to provide a much smoother support for the monolayer sample.

As a downside, HOPG is a semimetal unlike the insulating SiO₂. This seemingly makes it a poor choice of substrate for studying the electronic structure of quasi-freestanding monolayer of ReS₂. The stacking of the two materials would be described as a heterostructure, rather than isolated monolayers. However, HOPG and ReS₂ have significantly different lattice constants. The width of the HOPG surface BZ is $\approx 2.5 \text{ \AA}^{-1}$ and the only bands close to the Fermi level are the π bands at the K points in the BZ corners. ReS₂ on the other hand has a much larger lattice constant, which results in a surface BZ that only spans $\approx 1.1 \text{ \AA}^{-1}$. This means that the first surface BZ of ReS₂ is well separated from the HOPG bands, and one can assume that there is little impact, e.g. by hybridization, on the observed band structure. Figures 5.9 b-c) show the ReS₂ sample after the transfer onto the HOPG flake, which had been exfoliated onto the Si/SiO₂ substrate beforehand.

The photoemission experiments on the atomically thin ReS₂ were performed at the *SPEEM/UE49-PGMa* end-station at BESSY-II, Berlin. The sample was introduced into UHV and degassed for one hour at 150°C. Figures 5.9 d-f) show energy filtered photoemission electron microscope (PEEM) images integrated over kinetic energy ranges related to different core level peaks. The monolayer and bilayer areas can easily be identified by the increased intensity depending on the number of ReS₂ layers.

Micro-ARPES experiments

A great advantage of this end-station is its high spatial resolution in ARPES mode. However, the energy resolution of the SPEEM/UE49-PGMa end-station is $\approx 300 \text{ meV}$, which is, rather low compared to conventional ARPES setups. The size of the beamspot on the sample is $20 \mu\text{m} \times 30 \mu\text{m}$, and its position remains stable

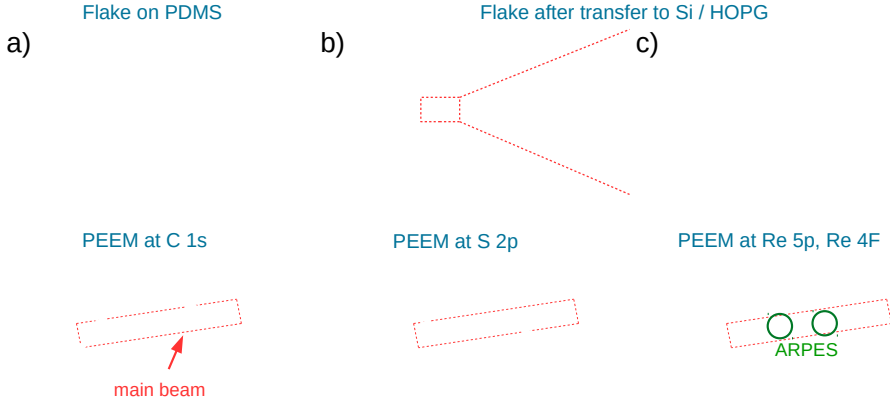


Figure 5.9: a-c) Optical microscope images of the atomically thin ReS_2 sample before (a) and after (b-c) the transfer to the substrate. d-f) PEEM images of the sample showing the intensity over different core level photoemission peaks taken at $h\nu = 300$ eV. The S and Re core level intensity images easily allow the identification of the monolayer, bilayer, and bulk like sample areas. In f) the green circles show the areas that were measured in the micro ARPES experiments.

even over several hours of measurement. The beamspot size can be reduced further by the exit slit of the beamline, at the expense of a reduced photon flux, down to $\approx 5 \mu\text{m} \times 30 \mu\text{m}$. In addition the field of view in real space can be limited to $\approx 5 \mu\text{m}$ by the field aperture of the PEEM. Therefore, the monolayer and bilayer parts of the sample can be selectively measured in ARPES mode. The chosen areas are indicated in figure 5.9.

Figure 5.10 shows the ReS_2 monolayer and bilayer ARPES data at selected binding energies. The spectra were taken at a photon energy of 100 eV to achieve the combination of high surface sensitivity with a high photon flux from the beamline. The only contribution of HOPG to the ARPES spectrum is the π band, which can easily be identified. At a binding energy of 4 eV the π -band appears as a sharp circle in the outer part of the image, and it retracts further towards the K points of the HOPG BZ with lower binding energy. Therefore, the dispersing features within the first BZ of ReS_2 can be interpreted as pure monolayer or bilayer ReS_2 bands.

The ReS_2 bands in the center of the images appear rather broad. To some extent this can be attributed to the low energy resolution of the experimental setup. However, the high degree of diffuse intensity suggest that the sharpness of the spectrum

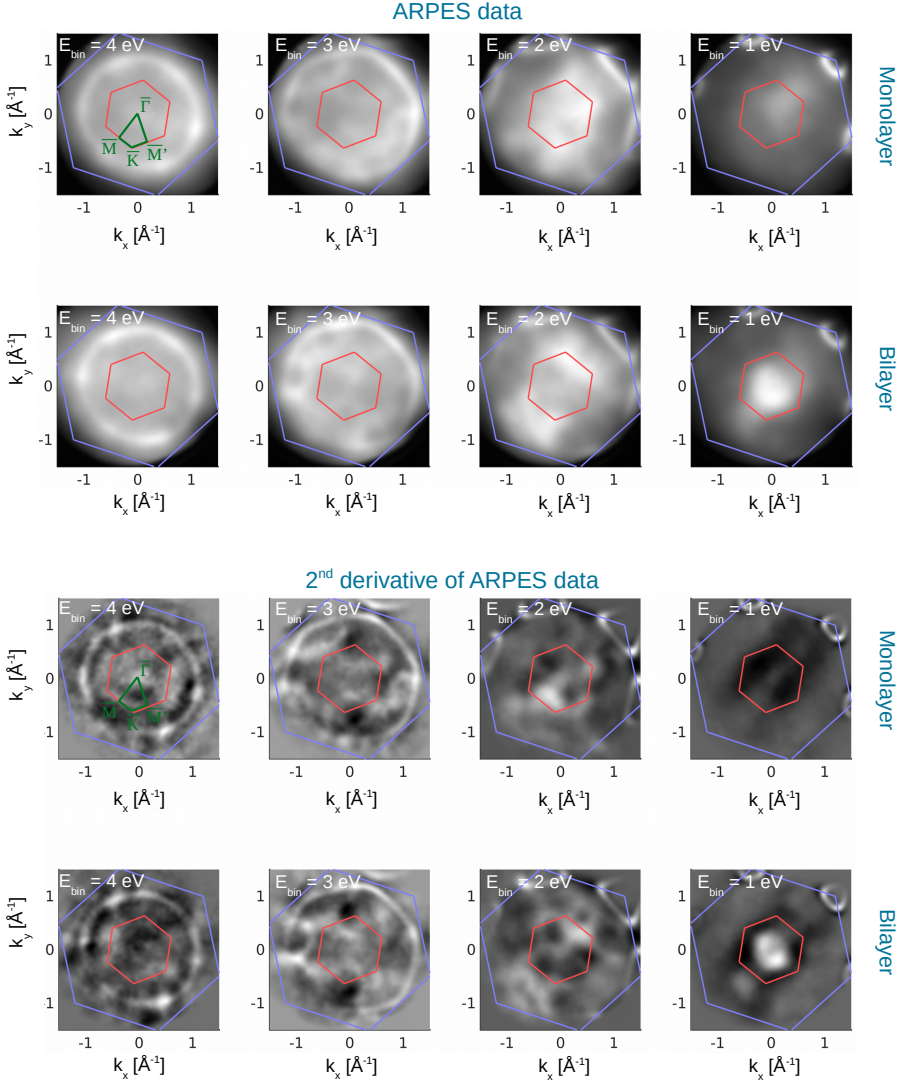


Figure 5.10: ARPES data and 2^{nd} derivative ARPES data of monolayer and bilayer ReS_2 taken at $h\nu = 100$ eV. The surface BZ of ReS_2 is marked in red and the much larger surface BZ of HOPG is marked in blue.

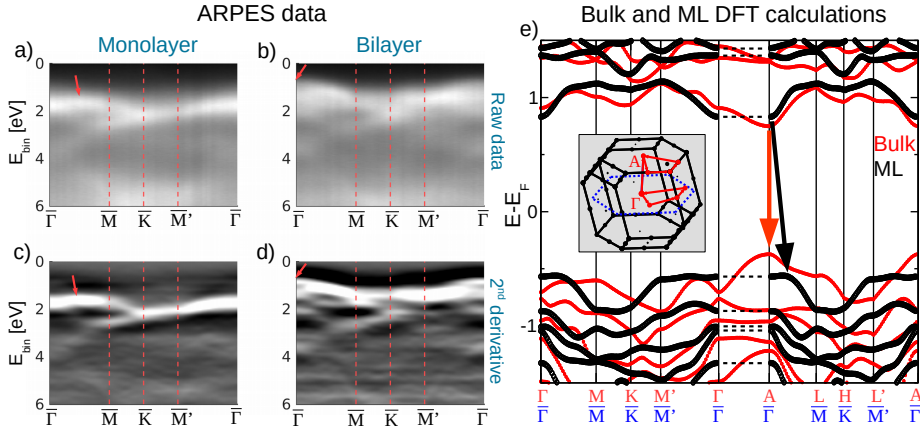


Figure 5.11: a-b) Monolayer and bilayer ARPES data along high symmetry lines of the ReS_2 surface BZ. c-d) 2nd derivative of the ARPES data. e) DFT calculation of the ReS_2 bulk and monolayer band structure. The valence band that is observed in the ARPES data is highlighted with a red arrow.

is mostly limited by the properties of the ReS_2 sample itself. Most likely degassing the sample at 150°C is not sufficient to fully remove contaminations. In the earlier attempts it was tried to clean samples at higher temperatures. However, the quality of the ARPES spectra even decreased, and real space PEEM images revealed that numerous holes had appeared in the samples during the annealing process. These are most likely caused by contaminations that are trapped underneath the exfoliated samples and burst through the monolayer. Wilson et al. [145] reported a similar behavior for exfoliated materials, referring to this phenomenon as “blisters”. A further argument for this interpretation is that the surface of bulk-like ReS_2 showed a much higher quality of the ARPES data after degassing, which suggests that the surface is effectively cleaned by this procedure. Therefore, it is most likely that contaminations trapped underneath the atomically thin samples have the main impact on the quality of the spectra. To enhance the contrast, the second derivative of the intensity in the energy direction $\frac{d^2I}{dE^2}$ is shown in addition to the raw data.

Figures 5.11 a-d) depict vertical cuts through the previously shown ARPES data and second derivative data along the high symmetry direction $\bar{\Gamma}$ -M-K-M'- $\bar{\Gamma}$ of the ReS_2 surface BZ. It is evident from the spectra, especially from the second derivative, that the valence band maximum of the monolayer lies between $\bar{\Gamma}$ and M, and not at the $\bar{\Gamma}$ point, as it was reported by Tongay et al. [142]. Furthermore, the dispersion

of the monolayer valence band that is observed in ARPES agrees well with the DFT calculation that is shown in figure 5.11 e). In this figure the DFT calculation for monolayer and bulk ReS₂ are overlaid with each other. The calculation shows the direct band gap of the bulk band structure at the A point. In the process of thinning down the material to an atomically thin monolayer, the increasing two dimensional quantum confinement does not allow for out-of-plane dispersion. According to the DFT calculation this results in a transition from a direct band gap at the A point to a larger, indirect gap with its conduction band minimum at $\bar{\Gamma}$ and the valence band maximum between $\bar{\Gamma}$ and \bar{M} . Although the conduction band minimum cannot be observed in ARPES the combination of DFT and ARPES is a convincing argument for the existence of an indirect-direct band gap transition. This observation agrees well with multiple reports of decreasing photoluminescence intensity accompanied by a blue-shifted peak from monolayer ReS₂ compared to bulk crystals [138,142,143].

Interestingly, the bilayer ARPES data reveals a pronounced maximum of the valence band at the $\bar{\Gamma}$ point, which is in contrast to the monolayer data. This increased dispersion resembles the onset of the out-of-plane delocalization of the electronic states, which leads to the indirect-direct band gap transition. However, the pronounced maximum suggests that the band gap transition already takes place between one and two layers, and that therefore only monolayer ReS₂ has an indirect gap.

Conclusions

This chapter presented the first detailed band structure study of ReS₂. With the observation of a strong out-of-plane dispersion in ARPES experiments and in DFT calculations it was shown that the valence electrons of ReS₂ are highly delocalized across the vdW gap. This observation stands in stark contrast to a recent publication by Tongay et al. [142], which reported that the bulk electronic structure is completely confined within the monolayers.

Furthermore, the valence band maximum was identified in the ARPES data for bulk, monolayer and bilayer crystals. The valence band maximum was found at the A point of the bulk crystal, and at the $\bar{\Gamma}$ point in the bilayer. Therefore, in both cases it was located in the center of the surface BZ. For the monolayer sample, however, the valence band maximum was found off center between $\bar{\Gamma}$ and \bar{A} . Although the conduction band minimum could not be observed experimentally, one can conclude the band gap position from the band structure calculations, which are in good agreement with the ARPES data. The results show a transition from a direct band gap in bulk and bilayer ReS₂ to an indirect gap in the monolayer.

Summary and outlook

We can only begin to imagine the possibilities that might arise from van der Waals (vdW) materials for scientists and engineers alike in the near future. Materials such as graphene and MoS_2 have already proven to be fascinating on their own. On one hand they have enabled the observation of new phenomena such as relativistic charge carriers in a solid. On the other hand they have a good chance not only to improve existing technological concepts like field effect transistors, but they also might open up entirely new possibilities for spintronics, valleytronics, and numerous other disciplines. The potential of the “atomic-scale Legos” can still be extended by the countless combinations for novel composite materials. A profound understanding of the electronic structure and of the interplay between vdW coupled layers will be an essential step towards discovering and characterizing new physical phenomena, and towards new applications. By combining angle-resolved photoemission spectroscopy (ARPES) with density functional theory (DFT), we have provided a thorough analysis of the electronic structure of two fascinating members of the transition metal dichalcogenide (TMDC) family: MoS_2 and ReS_2 .

The ARPES and DFT study of MoS_2 has shown that the large spin-splitting of the valleys at the edges of the Brillouin zone (BZ) is not, as it was commonly believed, exclusive to the materials with broken inversion symmetry. Due to the strong, two-dimensional confinement of the valleys, their properties are dominated by the local symmetry breaking within the monolayers instead of the global bulk space group. As a result, the spin-polarization of the valleys in the electronic structure is equally present in the bulk as it is in the monolayers, although in the bulk its sign alternates between adjacent layers. Therefore, it is compensated within the unit cell.

This observation is not only of importance for MoS_2 itself, but it demonstrates the existence of this recently introduced, hidden type of spin-polarization. The same concept can be applied to numerous other materials, which have been ruled out as candidates for spintronic applications for a long time because of their centrosymmetric space group.

For ReS₂ this thesis presented the first detailed ARPES study of its monolayer, bilayer, and bulk band structure. In an earlier publication the ReS₂ layers of the bulk crystal had been reported as electronically completely decoupled. Within this thesis it was shown, by a direct observation of a considerable out-of-plane dispersion in the photoemission experiments, that this is not the case. The experimental data and the presented DFT calculations prove that the ReS₂ valence electrons are strongly delocalized across the vdW gap, and therefore they are truly three-dimensional.

Furthermore, the valence band maxima of monolayer, bilayer, and bulk ReS₂ were identified. The combination of band structure calculations and photoemission data demonstrated that the material undergoes a transition from a direct band gap in the bulk and in the bilayer to an indirect gap in the monolayer. These results represent crucial information, since ReS₂ is proposed as a material for transistor devices and optical sensors, and the band gap as well as the valence band maximum have a major impact on the transport properties and the optical behavior.

In the near future investigations of vdW materials will be pursued further with a greater focus on the atomically thin layers. The next steps will involve band structure studies of mechanically restacked heterostructures such as MoS₂/WSe₂, which is known to form a two-dimensional p-n-junction. First experiments on MoS₂/WSe₂ have already been performed, but suffered from a strong sample contamination. However, we gained new experiences regarding the sample preparation during the more recent ReS₂ experiments that were presented here, and we are confident that the heterostructures can be prepared successfully for photoemission experiments.

The nanoESCA end-station in Trieste can play a key role in these experiments. Apart from its capabilities regarding momentum microscopy that were shown in this work, a recently installed, two-dimensional spin-detector will allow for new insights into the spin-textures of monolayers and heterostructures alike.

List of Abbreviations

- AES** Auger electron spectroscopy
- APW** augmented plane wave
- AFM** atomic force microscopy
- ARPES** angle-resolved photoemission spectroscopy
- BZ** Brillouin zone
- CVD** chemical vapor deposition
- DFT** density functional theory
- DLD** delay line detector
- FEFS** free-electron final-state
- FLAPW** full-potential linearized augmented plane wave
- GGA** generalized gradient approximation
- HOPG** highly oriented pyrolytic graphite
- IMFP** inelastic mean free path
- LEED** low energy electron diffraction
- LAPW** linearized augmented plane wave
- LED** light-emitting diode
- LDA** local density approximation
- MCP** microchannel plate
- PDMS** polydimethylsiloxan

PEEM photoemission electron microscope

PES photoemission spectroscopy

PGI-6 Peter Grünberg Institut 6

PGM plane grating monochromator

SEM scanning electron microscopy

SOC spin-orbit coupling

TMDC transition metal dichalcogenide

TRIM time-reversal invariant momenta

UHV ultra-high vacuum

vdW van der Waals

VUV vacuum ultraviolet

Bibliography

- [1] Gordon E. Moore. Cramming more components onto integrated circuits. *Electronics*, 38, 1965. 5
- [2] International Technology Roadmap for Semiconductors. <http://www.itrs2.net/>. Accessed: 2016-10-08. 5
- [3] The Story of the Intel® 4004. <http://www.intel.co.uk/content/www/uk/en/history/museum-story-of-intel-4004.html>. Accessed: 2016-10-08. 5
- [4] M. Mitchell Waldrop. The chips are down for Moore's law. *Nature*, 530:144:147, 2016. 5
- [5] Erol Gelenbe and Yves Caseau. The impact of information technology on energy consumption and carbon emissions. *Ubiquity*, June 2015. 5
- [6] The Nobel Prize in Physics 2010. https://www.nobelprize.org/nobel_prizes/physics/laureates/2010/. Accessed: 2016-10-08. 6
- [7] A. K. Geim and K. S. Novoselov. The rise of graphene. *Nat Mater*, 6:183 – 191. 6, 33
- [8] Pulickel Ajayan, Philip Kim, and Kaustav Banerjee. Two-dimensional van der Waals materials. *Phys Today*, 69:38, 2016. 6
- [9] A. K. Geim and I. V. Grigorieva. Van der Waals heterostructures. *Nature*, 499(7459):419–425, 2013. 6, 33
- [10] T Björkman, A Gulans, A V Krasheninnikov, and R M Nieminen. Are we van der Waals ready? *Journal of Physics: Condensed Matter*, 24(42):424218, 2012. 6, 31, 32
- [11] Andre K. Geim. Atomic-scale Legos. *SciAm*, 311:50–51, 2014. 6
- [12] B. Radisavljevic, A. Radenovic, J. Brivio, V. Giacometti, and A. Kis. Single-layer MoS₂ transistors. *Nat. Nano*, 6(3):147, 2011. 6, 33, 34

- [13] Yu-Ming Lin, Keith A. Jenkins, Alberto Valdes-Garcia, Joshua P. Small, Damon B. Farmer, and Phaedon Avouris. Operation of graphene transistors at gigahertz frequencies. *Nano Letters*, 9(1):422–426, 2009. PMID: 19099364. 6, 33
- [14] Tania Roy, Mahmut Tosun, Xi Cao, Hui Fang, Der-Hsien Lien, Peida Zhao, Yu-Ze Chen, Yu-Lun Chueh, Jing Guo, and Ali Javey. Dual-gated MoS₂/WSe₂ van der Waals tunnel diodes and transistors. *ACS Nano*, 9(2):2071–2079, 2015. PMID: 25598307. 6
- [15] Pyo Jin Jeon, Sung-Wook Min, Jin Sung Kim, Syed Raza Ali Raza, Kyunghee Choi, Hee Sung Lee, Young Tack Lee, Do Kyung Hwang, Hyoung Joon Choi, and Seongil Im. Enhanced device performances of WSe₂/MoS₂ van der Waals junction p-n diode by fluoropolymer encapsulation. *J. Mater. Chem. C*, 2015. 6
- [16] Yexin Deng, Zhe Luo, Nathan J. Conrad, Han Liu, Yongji Gong, Sina Najmaei, Pulickel M. Ajayan, Jun Lou, Xianfan Xu, and Peide D. Ye. Black phosphorus-monolayer MoS₂ van der Waals heterojunction p-n Diode. *ACS Nano*, 8(8):8292–8299, 2014. PMID: 25019534. 6, 33
- [17] S. A. Wolf, D. D. Awschalom, R. A. Buhrman, J. M. Daughton, S. von Molnár, M. L. Roukes, A. Y. Chtchelkanova, and D. M. Treger. Spintronics: A spin-based electronics vision for the future. *Science*, 294(5546):1488–1495, 2001. 6, 13
- [18] K. Sato and H. Katayama-Yoshida. First principles materials design for semiconductor spintronics. *Semiconductor Science and Technology*, 17(4):367, 2002. 6
- [19] Igor Žutić, Jaroslav Fabian, and S. Das Sarma. Spintronics: Fundamentals and applications. *Rev. Mod. Phys.*, 76:323–410, Apr 2004. 6
- [20] David D. Awschalom and Michael E. Flatte. Challenges for semiconductor spintronics. *Nat Phys*, 3(3):153–159, 2007. 6
- [21] M. Venkata Kamalakar, André Dankert, Johan Bergsten, Tommy Ive, and Saroj P. Dash. Spintronics with graphene-hexagonal boron nitride van der Waals heterostructures. *Applied Physics Letters*, 105(21), 2014. 6

- [22] Saptarshi Das, Joshua A. Robinson, Madan Dubey, Humberto Terrones, and Mauricio Terrones. Beyond graphene: progress in novel two-dimensional materials and van der Waals solids. *Annual Review of Materials Research*, 45(1):1–27, 2015. 6
- [23] J. L. Garcia-Pomar, A. Cortijo, and M. Nieto-Vesperinas. Fully valley-polarized electron beams in graphene. *Phys. Rev. Lett.*, 100:236801, Jun 2008. 6
- [24] D. Gunlycke and C. T. White. Graphene valley filter using a line defect. *Phys. Rev. Lett.*, 106:136806, Mar 2011. 6
- [25] Zhenhua Wu, F. Zhai, F. M. Peeters, H. Q. Xu, and Kai Chang. Valley-dependent Brewster angles and Goos-Hänchen effect in strained graphene. *Phys. Rev. Lett.*, 106:176802, Apr 2011. 6
- [26] Henning Schomerus. Helical scattering and valleytronics in bilayer graphene. *Phys. Rev. B*, 82:165409, Oct 2010. 6
- [27] Cong Mai, Andrew Barrette, Yifei Yu, Yuriy G. Semenov, Ki Wook Kim, Linyou Cao, and Kenan Gundogdu. Many-body effects in valleytronics: Direct measurement of valley lifetimes in single-layer MoS₂. *Nano Letters*, 14(1):202–206, 2014. PMID: 24325650. 6
- [28] Motohiko Ezawa. Spin valleytronics in silicene: Quantum spin hall–quantum anomalous hall insulators and single-valley semimetals. *Phys. Rev. B*, 87:155415, Apr 2013. 6
- [29] Nourdine Zibouche, Pier Philipsen, Agnieszka Kuc, and Thomas Heine. Transition-metal dichalcogenide bilayers: Switching materials for spintronic and valleytronic applications. *Phys. Rev. B*, 90:125440, Sep 2014. 6
- [30] Hualing Zeng, Junfeng Dai, Wang Yao, Di Xiao, and Xiaodong Cui. Valley polarization in MoS₂ monolayers by optical pumping. *Nat. Nano*, 7(8):490, 2012. 6, 7, 59, 61, 69
- [31] R. Suzuki, M. Sakano, Y. J. Zhang, R. Akashi, D. Morikawa, A. Harasawa, K. Yaji, K. Kuroda, K. Miyamoto, T. Okuda, K. Ishizaka, R. Arita, and

- Y. Iwasa. Valley-dependent spin polarization in bulk MoS₂ with broken inversion symmetry. *Nat. Nano*, 9(8):611, 2014. 6, 63, 64, 66, 83
- [32] Andreas Pospischil, Marco M. Furchi, and Thomas Mueller. Solar-energy conversion and light emission in an atomic monolayer p-n diode. *Nat Nano*, 9:257–261, 2014. 6, 33
- [33] Marco M. Furchi, Andreas Pospischil, Florian Libisch, Joachim Burgdörfer, and Thomas Mueller. Photovoltaic effect in an electrically tunable van der Waals heterojunction. *Nano Letters*, 14(8):4785–4791, 2014. PMID: 25057817. 6
- [34] Julien Vidal, Stephan Lany, Mayeul d’Avezac, Alex Zunger, Andriy Zakutayev, Jason Francis, and Janet Tate. Band-structure, optical properties, and defect physics of the photovoltaic semiconductor SnS. *Applied Physics Letters*, 100(3), 2012. 6
- [35] J. F. Sánchez-Royo, A. Segura, O. Lang, E. Schaar, C. Pettenkofer, W. Jaegermann, L. Roa, and A. Chevy. Optical and photovoltaic properties of indium selenide thin films prepared by van der Waals epitaxy. *Journal of Applied Physics*, 90(6), 2001. 6
- [36] Rui Cheng, Dehui Li, Hailong Zhou, Chen Wang, Anxiang Yin, Shan Jiang, Yuan Liu, Yu Chen, Yu Huang, and Xiangfeng Duan. Electroluminescence and photocurrent generation from atomically sharp WSe₂/MoS₂ heterojunction p-n diodes. *Nano Letters*, 14(10):5590–5597, 2014. PMID: 25157588. 6
- [37] F. Withers, Del Pozo, A. Mishchenko, A.P. Rooney, A. Gholinia, K. Watanabe, T. Taniguchi, S.J. Haigh, A.K. Geim, A.I. Tartakovskii, and K.S. Novoselov. Light-emitting diodes by band-structure engineering in van der Waals heterostructures. *Nat Mater*, 14(3):301–306, 2015. 6
- [38] J. Kong, M. G. Chapline, and H. Dai. Functionalized carbon nanotubes for molecular hydrogen sensors. *Advanced Materials*, 13(18):1384–1386, 2001. 6
- [39] Yung-Chang Lin, Hannu-Pekka Komsa, Chao-Hui Yeh, Torbjörn Björkman, Zheng-Yong Liang, Ching-Hwa Ho, Ying-Sheng Huang, Po-Wen Chiu,

-
- Arkady V. Krashennnikov, and Kazu Suenaga. Single-Layer ReS₂: two-dimensional semiconductor with tunable in-plane anisotropy. *ACS Nano*, 9(11):11249–11257, 2015. PMID: 26390381. 7, 87
- [40] Felix Bloch. Über die quantenmechanik der elektronen in kristallgittern. *Zeitschrift für Physik*, 52(7):555–600, 1929. 9
- [41] Charles Kittel. *Introduction to Solid State Physics*. John Wiley & Sons, Inc., New York, 6th edition, 1986. 9, 10, 11
- [42] F. Schwabl. *Quantenmechanik (QM I)*:. Springer-Lehrbuch. Springer, 2002. 13
- [43] Wolfgang Nolting and Anupuru. Ramakanth. *Quantum Theory of Magnetism*. Springer-Verlag Berlin Heidelberg, Berlin, Heidelberg, 2009. 13
- [44] G. Bihlmayer. Electronic structure of matter: Basics and DFT. *in: Probing the Nanoworld, 38th IFF Spring School Jülich, chapter A3*, 2007. 16, 17, 18
- [45] W. Kohn and L. J. Sham. Self-consistent equations including exchange and correlation effects. *Phys. Rev.*, 140:A1133–A1138, Nov 1965. 16
- [46] P. Hohenberg and W. Kohn. Inhomogeneous electron gas. *Phys. Rev.*, 136:B864–B871, Nov 1964. 16
- [47] Wolfgang Schattke and Michel A Van Hove. *Solid-State Photoemission and Related Methods: Theory and Experiment*. Wiley-VCH, Weinheim, 2003. 16, 18
- [48] I. Aguilera. Many-Body Effects in the Electronic Structure of Topological Insulators. *in: Topological Insulators, Fundamentals and Perspectives*, 2015. 17
- [49] O. Gunnarsson and B. I. Lundqvist. Exchange and correlation in atoms, molecules, and solids by the spin-density-functional formalism. *Phys. Rev. B*, 13:4274–4298, May 1976. 17
- [50] Alberto García, Christian Elsässer, Jing Zhu, Steven G. Louie, and Marvin L. Cohen. Use of gradient-corrected functionals in total-energy calculations for solids. *Phys. Rev. B*, 46:9829–9832, Oct 1992. 18

- [51] Andrea Dal Corso, Alfredo Pasquarello, Alfonso Baldereschi, and Roberto Car. Generalized-gradient approximations to density-functional theory: A comparative study for atoms and solids. *Phys. Rev. B*, 53:1180–1185, Jan 1996. 18
- [52] FLEUR project homepage. <http://www.flapw.de/>. Accessed: 2016-10-03. 19, 60, 87
- [53] H. Hertz. Über einen Einfluss des ultravioletten Lichtes auf die elektrische Entladung. *Annalen der Physik*, 267:983, 1887. 20
- [54] The Nobel Prize in Physics 1921. http://www.nobelprize.org/nobel_prizes/physics/laureates/1921/index.html. Accessed: 2016-08-05. 20
- [55] Elbio Dagotto. Correlated electrons in high-temperature superconductors. *Rev. Mod. Phys.*, 66:763–840, Jul 1994. 21
- [56] Patrick A. Lee, Naoto Nagaosa, and Xiao-Gang Wen. Doping a mott insulator: Physics of high-temperature superconductivity. *Rev. Mod. Phys.*, 78:17–85, Jan 2006. 21
- [57] Peter J. Feibelman and D. E. Eastman. Photoemission spectroscopy—correspondence between quantum theory and experimental phenomenology. *Phys. Rev. B*, 10:4932–4947, Dec 1974. 22
- [58] C. M. Schneider. Photoelectron emission spectroscopy. *chapter F3. Forschungszentrum Jülich GmbH, 43rd IFF Spring School*, 2012. 22, 23
- [59] N. V. Smith, P. Thiry, and Y. Petroff. Photoemission linewidths and quasi-particle lifetimes. *Phys. Rev. B*, 47:15476–15481, Jun 1993. 23
- [60] Andrea Damascelli, Zahid Hussain, and Zhi-Xun Shen. Angle-resolved photoemission studies of the cuprate superconductors. *Rev. Mod. Phys.*, 75:473–541, Apr 2003. 23
- [61] Wikipedia: ARPES. https://en.wikipedia.org/wiki/Angle-resolved_photoemission_spectroscopy. Accessed: 2016-08-10. 24

- [62] M. P. Seah and W. A. Dench. Quantitative electron spectroscopy of surfaces: A standard data base for electron inelastic mean free paths in solids. *Surface and Interface Analysis*, 1(1):2–11, 1979. 26, 67
- [63] Andrea Damascelli. Probing the electronic structure of complex systems by arpes. *Physica Scripta*, 2004(T109):61, 2004. 27
- [64] G. Paolucci, K.C. Prince, B.E. Hayden, P.J. Davie, and A.M. Bradshaw. Photoemission band mapping via surface umklapp. *Solid State Communications*, 52(12):937 – 940, 1984. 27
- [65] F. London. Zur Theorie und Systematik der Molekularkräfte. *Zeitschrift für Physik*, 63(3):245–279, 1930. 31
- [66] F. London. The general theory of molecular forces. *Trans. Faraday Soc.*, 33:8b–26, 1937. 31
- [67] R. Eisenshitz and F. London. Über das Verhältnis der van der Waalschen Kräfte zu den momöpolaren Bindungskräften. *Z. Phys.*, 60:490, 1930. 31
- [68] J. E. Lennard-Jones. Processes of adsorption and diffusion on solid surfaces. *Trans. Faraday Soc.*, 28:333–359, 1932. 31
- [69] Kristian Berland, Valentino R Cooper, Kyuho Lee, Elsebeth Schröder, T Thonhauser, Per Hyldgaard, and Bengt I Lundqvist. van der Waals forces in density functional theory: a review of the vdW-DF method. *Reports on Progress in Physics*, 78(6):066501, 2015. 31, 32
- [70] Kristian Berland and Per Hyldgaard. Analysis of van der Waals density functional components: Binding and corrugation of benzene and C₆₀ on boron nitride and graphene. *Phys. Rev. B*, 87:205421, May 2013. 32
- [71] Gabriella Graziano, Jirí Klimeš, Felix Fernandez-Alonso, and Angelos Michaelides. Improved description of soft layered materials with van der Waals density functional theory. *Journal of Physics: Condensed Matter*, 24(42):424216, 2012. 32
- [72] T. Björkman, A. Gulans, A. V. Krasheninnikov, and R. M. Nieminen. van der Waals Bonding in Layered Compounds from Advanced Density-Functional First-Principles Calculations. *Phys. Rev. Lett.*, 108:235502, Jun 2012. 32

- [73] K. S. Novoselov, D. Jiang, F. Schedin, T. J. Booth, V. V. Khotkevich, S. V. Morozov, and A. K. Geim. 102:10451–10453, 2005. 32
- [74] Anthony Ayari, Enrique Cobas, Ololade Ogundadegbe, and Michael S. Fuhrer. Realization and electrical characterization of ultrathin crystals of layered transition-metal dichalcogenides. *Journal of Applied Physics*, 101(1), 2007. 32
- [75] Felix Hanke and Jonas Björk. Structure and local reactivity of the au(111) surface reconstruction. *Phys. Rev. B*, 87:235422, Jun 2013. 32
- [76] M. Z. Hasan and C. L. Kane. Colloquium : Topological insulators. *Rev. Mod. Phys.*, 82:3045–3067, Nov 2010. 32
- [77] Xin Chen and Aidan R. McDonald. Functionalization of two-dimensional transition-metal dichalcogenides. *Advanced Materials*, 28(27):5738–5746, 2016. 32
- [78] Deep Jariwala, Tobin J. Marks, and Mark C. Hersam. Mixed-dimensional van der Waals heterostructures. *Nat Mater*, advanceonlinepublication, 2016. 32
- [79] K. S. Novoselov, A. K. Geim, S. V. Morozov, D. Jiang, M. I. Katsnelson, I. V. Grigorieva, S. V. Dubonos, and A. A. Firsov. Two-dimensional gas of massless Dirac fermions in graphene. *Nature*, 438:197 – 200. 33
- [80] Andres Castellanos-Gomez, Michele Buscema, Rianda Molenaar, Vibhor Singh, Laurens Janssen, Herre S J van der Zant, and Gary A Steele. Deterministic transfer of two-dimensional materials by all-dry viscoelastic stamping. *2D Materials*, 1(1):011002, 2014. 33, 100
- [81] Yongjie Zhan, Zheng Liu, Sina Najmaei, Pulickel M. Ajayan, and Jun Lou. Large-area vapor-phase growth and characterization of MoS₂ atomic layers on a SiO₂ substrate. *Small*, 8(7):966–971, 2012. 33
- [82] Xuesong Li, Weiwei Cai, Jinho An, Seyoung Kim, Junghyo Nah, Dongxing Yang, Richard Piner, Aruna Velamakanni, Inhwa Jung, Emanuel Tutuc, Sanjay K. Banerjee, Luigi Colombo, and Rodney S. Ruoff. Large-area synthesis of high-quality and uniform graphene films on copper foils. *Science*, 324(5932):1312–1314, 2009. 33

-
- [83] Li Song, Lijie Ci, Hao Lu, Pavel B. Sorokin, Chuanhong Jin, Jie Ni, Alexander G. Kvashnin, Dmitry G. Kvashnin, Jun Lou, Boris I. Yakobson, and Pulickel M. Ajayan. Large scale growth and characterization of atomic hexagonal boron nitride layers. *Nano Letters*, 10(8):3209–3215, 2010. PMID: 20698639. 33
- [84] Zheng Liu, Li Song, Shizhen Zhao, Jiaqi Huang, Lulu Ma, Jiangnan Zhang, Jun Lou, and Pulickel M. Ajayan. Direct growth of graphene/hexagonal boron nitride stacked layers. *Nano Letters*, 11(5):2032–2037, 2011. PMID: 21488689. 33
- [85] Jill A. Miwa, Maciej Dendzik, Signe S. Grønberg, Marco Bianchi, Jeppe V. Lauritsen, Philip Hofmann, and Søren Ulstrup. Van der Waals epitaxy of two-dimensional MoS₂ graphene Heterostructures in ultrahigh vacuum. *ACS Nano*, 9(6):6502–6510, 2015. PMID: 26039108. 33
- [86] Horacio Coy Diaz, Redhouane Chaghi, Yujing Ma, and Matthias Batzill. Molecular beam epitaxy of the van der Waals heterostructure MoTe₂ on MoS₂ : phase, thermal, and chemical stability. *2D Materials*, 2(4):044010, 2015. 33
- [87] Yu-Chuan Lin, Ram Krishna Ghosh, Rafik Addou, Ning Lu, Sarah M. Eichfeld, Hui Zhu, Ming-Yang Li, Xin Peng, Moon J. Kim, Lain-Jong Li, Robert M. Wallace, Suman Datta, and Joshua A. Robinson. Atomically thin resonant tunnel diodes built from synthetic van der Waals heterostructures. *Nat. Commun.*, 6, 2015. 33
- [88] K.I. Bolotin, K.J. Sikes, Z. Jiang, M. Klima, G. Fudenberg, J. Honeen, P. Kim, and H.L. Stormer. Ultrahigh electron mobility in suspended graphene. *Solid State Communications*, 146(9):351 – 355, 2008. 33
- [89] Xiaodong Xu, Wang Yao, Di Xiao, and Tony F. Heinz. Spin and pseudospins in layered transition metal dichalcogenides. *Nat Phys*, 10:343 – 350, 2014. 34, 59
- [90] Qing Hua Wang, Kalantar, Andras Kis, Jonathan N. Coleman, and Michael S. Strano. Electronics and optoelectronics of two-dimensional transition metal dichalcogenides. *Nat Nano*, 7(11):699–712, 2012. 34

- [91] Band Structure Engineering Lab homepage. <https://pgi-jcns.fz-juelich.de/wp/electronic-structure/>. Accessed: 2016-09-27. 37
- [92] Markus Eschbach. *Band Structure Engineering in 3D Topological Insulators Investigated by Angle-Resolved Photoemission Spectroscopy*. dissertation, Universität Duisburg-Essen, 2016. 37, 38, 39, 41, 42, 44, 45
- [93] Related pergamon titles of interest. In J.A. Bittencourt, editor, *Fundamentals of Plasma Physics*. Pergamon, Amsterdam, 1986. 39
- [94] G Schönhense and U Heinzmann. A capillary discharge tube for the production of intense VUV resonance radiation. *Journal of Physics E: Scientific Instruments*, 16(1):74, 1983. 40
- [95] S. Suga, A. Sekiyama, G. Funabashi, J. Yamaguchi, M. Kimura, M. Tsujibayashi, T. Uyama, H. Sugiyama, Y. Tomida, G. Kuwahara, S. Kitayama, K. Fukushima, K. Kimura, T. Yokoi, K. Murakami, H. Fujiwara, Y. Saitoh, L. Plucinski, and C. M. Schneider. High resolution, low $h\nu$ photoelectron spectroscopy with the use of a microwave excited rare gas lamp and ionic crystal filters. *Review of Scientific Instruments*, 81(10), 2010. 41
- [96] P Gospodarič. Laser-based angle-resolved photoemission spectroscopy study of spin-orbit coupling effects on solid state surfaces. Master's thesis, University of Cologne, 2015. 41
- [97] L. Plucinski, J. Minár, B. C. Sell, J. Braun, H. Ebert, C. M. Schneider, and C. S. Fadley. Band mapping in higher-energy x-ray photoemission: Phonon effects and comparison to one-step theory. *Phys. Rev. B*, 78:035108, Jul 2008. 41
- [98] R E Imhof, A Adams, and G C King. Energy and time resolution of the 180 degrees hemispherical electrostatic analyser. *Journal of Physics E: Scientific Instruments*, 9(2):138, 1976. 43
- [99] Y.M. Cross and J.E. Castle. The relationship between transmission efficiencies in the FRR and fat modes of an electron spectrometer. *Journal of Electron Spectroscopy and Related Phenomena*, 22(1):53 – 60, 1981. 43

- [100] S. LaShell, B. A. McDougall, and E. Jensen. Spin Splitting of an Au(111) Surface State Band Observed with Angle Resolved Photoelectron Spectroscopy. *Phys. Rev. Lett.*, 77:3419–3422, Oct 1996. 44
- [101] J. Henk. *Beiträge zur Theorie der Elektronenspektroskopie: Anwendungen der relativistischen Vielfachstreutheorie*. habilitation, Martin-Luther-Universität Halle-Wittenberg, 1960. 44
- [102] P. Luchini and H. Motz. *Undulators and free-electron lasers*. International series of monographs on physics. Clarendon Press, 1990. 46
- [103] S. Cramm. IFF Jahresbericht, 1999. 47
- [104] H. Petersen, C. Jung, C. Hellwig, W. B. Peatman, and W. Gudat. Review of plane grating focusing for soft x-ray monochromators. *Rev. Sci. Instrum.*, 66, 1995. 46, 47
- [105] Shaukat Khan, Mohammed Bakr, Markus Höner, Holger Huck, Robert Molo, André Nowaczyk, Andreas Schick, Peter Ungelenk, and Maryam Zeinalzadeh. Coherent harmonic generation at delta: A new facility for ultrashort pulses in the vuv and thz regime. *Synchrotron Radiation News*, 24(5):18–23, 2011. 50
- [106] Surface Concept GmbH. Delayline Detector DLD-3030. <http://www.surface-concept.com>, Accessed: 2016-10-03. 50
- [107] Alexej Herdt. *Exploring the electronic properties of novel spintronic materials by photoelectron spectroscopy*. dissertation, Universität Duisburg-Essen, 2012. 50
- [108] D. Yu, C. Math, M. Meier, M. Escher, G. Rangelov, and M. Donath. Characterisation and application of a SPLEED-based spin polarisation analyser. *Surface Science*, 601:5803–5808, December 2007. 50
- [109] J. Kirschner and R. Feder. Spin polarization in double diffraction of low-energy electrons from w(001): Experiment and theory. *Phys. Rev. Lett.*, 42:1008–1011, Apr 1979. 50
- [110] L. Plucinski, A. Oelsner, F. Matthes, and C.M. Schneider. A hemispherical photoelectron spectrometer with 2-dimensional delay-line detector and

- integrated spin-polarization analysis. *J. Electron. Spectrosc. Relat. Phenom.*, 181(2):215 – 219, 2010. 51
- [111] Marten Patt. *Bulk and surface sensitive energy-filtered photoemission microscopy using synchrotron radiation for the study of resistive switching memories*. dissertation, Universität Duisburg-Essen, 2016. 53, 54, 55, 57
- [112] M Escher, N Weber, M Merkel, C Ziethen, P Bernhard, G Schönhense, S Schmidt, F Forster, F Reinert, B Krömker, and D Funnemann. Nanoesca: a novel energy filter for imaging x-ray photoemission spectroscopy. *Journal of Physics: Condensed Matter*, 17(16):S1329, 2005. 53, 56
- [113] E. Bauer. The resolution of the low energy electron reflection microscope. *Ultramicroscopy*, 17(1):51 – 56, 1985. 53
- [114] Christian Tusche, Alexander Krasnyuk, and Jürgen Kirschner. Spin resolved bandstructure imaging with a high resolution momentum microscope. *Ultramicroscopy*, 159, Part 3:520 – 529, 2015. Special Issue: LEEM-PEEM 9. 53, 56
- [115] F. Hadjarab and J.L. Erskine. Image properties of the hemispherical analyzer applied to multichannel energy detection. *Journal of Electron Spectroscopy and Related Phenomena*, 36(3):227 – 243, 1985. 56
- [116] Kin Fai Mak, Changgu Lee, James Hone, Jie Shan, and Tony F. Heinz. Atomically thin MoS₂: A new direct-gap semiconductor. *Phys. Rev. Lett.*, 105:136805, Sep 2010. 59, 65, 66, 69, 84
- [117] Di Xiao, Gui-Bin Liu, Wanxiang Feng, Xiaodong Xu, and Wang Yao. Coupled spin and valley physics in monolayers of MoS₂ and other group-vi dichalcogenides. *Phys. Rev. Lett.*, 108:196802, May 2012. 59, 61, 69
- [118] Xiuwen Zhang, Qihang Liu, Jun-Wei Luo, Arthur J. Freeman, and Alex Zunger. Hidden spin polarization in inversion-symmetric bulk crystals. *Nat Phys*, 10:381–393, 2014. 59, 75, 76
- [119] A. Kimura, E. E. Krasovskii, R. Nishimura, K. Miyamoto, T. Kadono, K. Kanomaru, E. V. Chulkov, G. Bihlmayer, K. Shimada, H. Namatame, and M. Taniguchi. Strong rashba-type spin polarization of the photocurrent

- from bulk continuum states: Experiment and theory for Bi(111). *Phys. Rev. Lett.*, 105:076804, Aug 2010. 59
- [120] J. M. Riley, F. Mazzola, M. Dendzik, M. Michiardi, T. Takayama, L. Bawden, C. Granerod, M. Leandersson, T. Balasubramanian, M. Hoesch, T. K. Kim, H. Takagi, W. Meevasana, Ph. Hofmann, M. S. Bahramy, J. W. Wells, J. W. Wells, and P. D. C. King. Direct observation of spin-polarized bulk bands in an inversion-symmetric semiconductor. *Nat Phys*, 10:835, Sep 2014. 59, 81, 82, 83, 84, 85
- [121] Kin Fai Mak, Keliang He, Jie Shan, and Tony F. Heinz. Control of valley polarization in monolayer MoS₂ by optical helicity. *Nat Nano*, 7:494–498, 2012. 59
- [122] Qihang Liu, Xiuwen Zhang, and Alex Zunger. Intrinsic circular polarization in centrosymmetric stacks of transition-metal dichalcogenide compounds. *Phys. Rev. Lett.*, 114:087402, Feb 2015. 59
- [123] Roscoe G. Dickinson and Linus Pauling. The crystal structure of molybdenite. *Journal of the American Chemical Society*, 45(6):1466–1471, 1923. 60
- [124] Ravi K. Tiwari, Jianshu Yang, Mark Saeys, and Christian Joachim. Surface reconstruction of MoS₂ to Mo₂S₃. *Surface Science*, 602(15):2628 – 2633, 2008. 62
- [125] J.A. Wilson and A.D. Yoffe. The transition metal dichalcogenides discussion and interpretation of the observed optical, electrical and structural properties. *Advances in Physics*, 18(73):193–335, 1969. 63
- [126] A R Beal, J C Knights, and W Y Liang. Transmission spectra of some transition metal dichalcogenides. ii. group via: trigonal prismatic coordination. *Journal of Physics C: Solid State Physics*, 5(24):3540, 1972. 63
- [127] Wencan Jin, Po-Chun Yeh, Nader Zaki, Datong Zhang, Jerzy T. Sadowski, Abdullah Al-Mahboob, Arend M. van der Zande, Daniel A. Chenet, Jerry I. Dadap, Irving P. Herman, Peter Sutter, James Hone, and Richard M. Osgood. Direct measurement of the thickness-dependent electronic band structure of MoS₂ using angle-resolved photoemission spectroscopy. *Phys. Rev. Lett.*, 111:106801, Sep 2013. 65, 66

- [128] Yi Zhang, Tay-Rong Chang, Bo Zhou, Yong-Tao Cui, Hao Yan, Zhongkai Liu, Felix Schmitt, James Lee, Rob Moore, Yulin Chen, Hsin Lin, Horng-Tay Jeng, Sung-Kwan Mo, Zahid Hussain, Arun Bansil, and Zhi-Xun Shen. Direct observation of the transition from indirect to direct bandgap in atomically thin epitaxial MoSe₂. *Nat Nano*, 9(2):111–115, 2014. 66
- [129] S K Mahatha, K D Patel, and Krishnakumar S R Menon. Electronic structure investigation of MoS₂ and MoSe₂ using angle-resolved photoemission spectroscopy and ab initio band structure studies. *Journal of Physics: Condensed Matter*, 24(47):475504, 2012. 66
- [130] Sang Wook Han, Gi-Beom Cha, Emmanouil Frantzeskakis, Ivy Razado-Colambo, José Avila, Young S. Park, Daehyun Kim, Jihoon Hwang, Jeong Soo Kang, Sunmin Ryu, Won Seok Yun, Soon Cheol Hong, and Maria C. Asensio. Band-gap expansion in the surface-localized electronic structure of MoS₂(0002). *Phys. Rev. B*, 86:115105, Sep 2012. 66, 68, 72, 84
- [131] Drew W. Latzke, Wentao Zhang, Aslihan Suslu, Tay-Rong Chang, Hsin Lin, Horng-Tay Jeng, Sefaattin Tongay, Junqiao Wu, Arun Bansil, and Alessandra Lanzara. Electronic structure, spin-orbit coupling, and interlayer interaction in bulk MoS₂ and WS₂. *Phys. Rev. B*, 91:235202, Jun 2015. 66, 68, 84
- [132] Hannu-Pekka Komsa and Arkady V. Krasheninnikov. Electronic structures and optical properties of realistic transition metal dichalcogenide heterostructures from first principles. *Phys. Rev. B*, 88:085318, Aug 2013. 84
- [133] E. Cappelluti, R. Roldán, J. A. Silva-Guillén, P. Ordejón, and F. Guinea. Tight-binding model and direct-gap/indirect-gap transition in single-layer and multilayer MoS₂. *Phys. Rev. B*, 88:075409, Aug 2013. 84
- [134] S. W. Han, Hyuksang Kwon, Seong Keun Kim, Sunmin Ryu, Won Seok Yun, D. H. Kim, J. H. Hwang, J.-S. Kang, J. Baik, H. J. Shin, and S. C. Hong. Band-gap transition induced by interlayer van der Waals interaction in MoS₂. *Phys. Rev. B*, 84:045409, Jul 2011. 84
- [135] Tawinan Cheiwchanchamnangij and Walter R. L. Lambrecht. Quasiparticle band structure calculation of monolayer, bilayer, and bulk MoS₂. *Phys. Rev. B*, 85:205302, May 2012. 84

-
- [136] K.K. Tiong, C.H. Ho, and Y.S. Huang. The electrical transport properties of ReS_2 and ReSe_2 layered crystals. *Solid State Communications*, 111(11):635–640, 1999. 87
- [137] C. H. Ho, Y. S. Huang, K. K. Tiong, and P. C. Liao. Absorption-edge anisotropy in reS_2 and rese_2 layered semiconductors. *Phys. Rev. B*, 58:16130–16135, Dec 1998. 87
- [138] Ozgur Burak Aslan, Daniel A. Chenet, Arend M. van der Zande, James C. Hone, and Tony F. Heinz. Linearly Polarized Excitons in Single- and Few-Layer ReS_2 Crystals. *ACS Photonics*, 3(1):96–101, 2016. 87, 105
- [139] Huan Zhao, Jiangbin Wu, Hongxia Zhong, Qiushi Guo, Xiaomu Wang, Fengnian Xia, Li Yang, Pingheng Tan, and Han Wang. Interlayer interactions in anisotropic atomically thin rhenium diselenide. *Nano Research*, 8(11):3651–3661, 2015. 87
- [140] Philipp Nagler, Gerd Plechinger, Christian Schüller, and Tobias Korn. Observation of anisotropic interlayer Raman modes in few-layer ReS_2 . *Rapid Research Letters*, 10(2):185–189, 2016. 87
- [141] H.-J. Lamfers, A. Meetsma, G.A. Wiegers, and J.L. de Boer. The crystal structure of some rhenium and technetium dichalcogenides. *Journal of Alloys and Compounds*, 241(1):34–39, 1996. 87
- [142] Sefaattin Tongay, Hasan Sahin, Changhyun Ko, Alex Luce, Wen Fan, Kai Liu, Jian Zhou, Ying-Sheng Huang, Ching-Hwa Ho, Jinyuan Yan, D. Frank Ogletree, Shaul Aloni, Jie Ji, Shushen Li, Jingbo Li, F. M. Peeters, and Junqiao Wu. Monolayer behaviour in bulk ReS_2 due to electronic and vibrational decoupling. *Nat. Commun.*, 5, Feb 2014. 89, 91, 92, 104, 105, 106
- [143] Xiao-Fen Qiao, Jiang-Bin Wu, Linwei Zhou, Jingsi Qiao, Wei Shi, Tao Chen, Xin Zhang, Jun Zhang, Wei Ji, and Ping-Heng Tan. Polytypism and unexpected strong interlayer coupling in two-dimensional layered ReS_2 . *Nanoscale*, 8:8324–8332, 2016. 92, 105
- [144] Matlab homepage. <https://de.mathworks.com/products/matlab/>. Accessed: 2016-10-10. 95

- [145] N. R. Wilson, P. V. Nguyen, K. L. Seyler, P. Rivera, A. J. Marsden, Z. P. L. Laker, G. C. Constantinescu, V. Kandyba, A. Barinov, N. D. M. Hine, X. Xu, and D. H. Cobden. Band parameters and hybridization in 2D semiconductor heterostructures from photoemission spectroscopy. *ArXiv e-prints*, January 2016. 104

Band / Volume 157

Interface phenomena in $\text{La}_{1/3}\text{Sr}_{2/3}\text{FeO}_3$ / $\text{La}_{2/3}\text{Sr}_{1/3}\text{MnO}_3$ heterostructures and a quest for p-electron magnetism

M. Waschk (2017), ix, 205 pp
ISBN: 978-3-95806-281-8

Band / Volume 158

Physics of Life

Lecture Notes of the 49th IFF Spring School 2018
26 February – 09 March 2018, Jülich, Germany
ed. by G. Gompper, J. Dhont, J. Elgeti, C. Fahlke, D. Fedosov,
S. Förster, P. Lettinga, A. Offenhäusser (2018), ca 1000 pp
ISBN: 978-3-95806-286-3

Band / Volume 159

Identifizierung von Bindungsdeterminanten von Tat-Vorläuferproteinen an den TatBCRezeptorkomplex während der Tat-abhängigen Proteintranslokation in *Escherichia coli*

A. Ulfing (2018), 186 pp
ISBN: 978-3-95806-290-0

Band / Volume 160

***Corynebacterium glutamicum* – a novel platform for the production of plant polyphenols**

N. Kallscheuer (2018), X, 98 pp
ISBN: 978-3-95806-291-7

Band / Volume 161

Neurons on 3D polymer nanostructures

A. Belu (2018), vii, 135 pp
ISBN: 978-3-95806-296-2

Band / Volume 162

Tailoring and Characterisation of Bioelectronic Interfaces

A. Markov (2018), 75 pp
ISBN: 978-3-95806-298-6

Band / Volume 163

Epitaxy of group IV Si-Ge-Sn alloys for advanced heterostructure light emitters

N. von den Driesch (2018), viii, 149 pp
ISBN: 978-3-95806-300-6

Band / Volume 164

**Impact and Regulatory Control of the CGP3 Prophage in
*Corynebacterium glutamicum***

E. Pfeifer (2018), IV, 206 pp
ISBN: 978-3-95806-301-3

Band / Volume 165

**Establishment of Bacterial Microcompartments in the
Industrial Production Strain *Corynebacterium glutamicum***

I. Huber (2018), X, 114, XI-XXXIV pp
ISBN: 978-3-95806-302-0

Band / Volume 166

Current-Induced Magnetization Dynamics in Ferromagnetic Nanowires

M. I. Khan (2018), vi, 138 pp
ISBN: 978-3-95806-308-2

Band / Volume 167

Management of Electrophysiological Data & Metadata

Making complex experiments accessible to yourself and others

L. Zehl (2018), 182 pp
ISBN: 978-3-95806-311-2

Band / Volume 168

**Investigation of GeSn as Novel Group IV
Semiconductor for Electronic Applications**

C. Schulte-Braucks, Christian (2018), xx, 165, XII pp
ISBN: 978-3-95806-312-9

Band / Volume 169

**Tailoring the Electronic Properties of Epitaxial Oxide Films
via Strain for SAW and Neuromorphic Applications**

Y. Dai (2018), VI, 133 pp
ISBN: 978-3-95806-319-8

Band / Volume 170

**The electronic structure of transition metal dichalcogenides investigated
by angle-resolved photoemission spectroscopy**

M. Gehlmann (2018), ii, 108, XVIII pp
ISBN: 978-3-95806-324-2

Weitere **Schriften des Verlags im Forschungszentrum Jülich** unter
<http://www.zb1.fz-juelich.de/verlagextern1/index.asp>

Schlüsseltechnologien / Key Technologies

Band / Volume 170

ISBN 978-3-95806-324-2

Mitglied der Helmholtz-Gemeinschaft

